UC Irvine
UC Irvine Electronic Theses and Dissertations

Title
Understanding the Role of Global Meridional Overturning Circulation in the Ocean Carbon Sink

Permalink
https://escholarship.org/uc/item/37d9b192

Author
Liu, Yi

Publication Date
2023

Copyright Information
This work is made available under the terms of a Creative Commons Attribution License, availalbe at https://creativecommons.org/licenses/by/4.0/

Peer reviewed|Thesis/dissertation

eScholarship.org Powered by the California Digital Library
University of California

UNIVERSITY OF CALIFORNIA,
IRVINE

Understanding the Role of Global Meridional Overturning Circulation in the Ocean Carbon Sink

DISSERTATION

submitted in partial satisfaction of the requirements
for the degree of

DOCTOR OF PHILOSOPHY

in Earth System Science

by

Yi Liu

Dissertation Committee:
Professor J. Keith Moore, Chair
Professor François Primeau
Professor James Randerson
Professor Adam Martiny

2023

Chapter 2 © 2023 Nature Publishing Group
All other materials © 2023 Yi Liu

TABLE OF CONTENTS

Page

LIST OF FIGURES iii

LIST OF TABLES v

ACKNOWLEDGEMENTS vi

VITA viii

ABSTRACT OF THE DISSERTATION ix

CHAPTER 1: Introduction 1

CHAPTER 2: Reduced CO_2 uptake and growing nutrient sequestration from slowing overturning circulation 10

CHAPTER 3: Surface-to-Interior Transport Timescales and Ventilation Patterns in a Time-Dependent Circulation Driven by Sustained Climate Warming 54

CHAPTER 4: Surface-to-Interior Transport Timescales and Ventilation Patterns in a Time-Dependent Circulation Driven by Sustained Climate Warming 87

CHAPTER 5: Summary and Conclusions 116

REFERENCES 120

LIST OF FIGURES

Page

Figure 2.1 Slowing Meridional Overturning Circulation (MOC) with strong climate warming. 23

Figure 2.2 Changes in meridional overturning, carbon export, and carbon storage by 2100. 24

Figure 2.3 Slowing SMOC rates reduce ocean carbon uptake. 25

Figure 2.4 Shifting carbon and nutrient distributions over time with climate warming. 26

Figure 2.5 Biological export and changing circulation contributions to regenerated carbon storage. 27

Figure 2.6 Slowdown of Meridional Overturning Circulation (MOC) in CMIP5 (RCP8.5-ECP8.5) and CMIP6 (SSP1-2.6 and SSP2-4.5). 28

Figure 2.7 Declining Southern Ocean AABW Formation and SMOC. 29

Figure 2.8 Deep ocean carbon accumulation (> 2000m) in CESMv1 RCP8.5 and 13 CMIP6 models under the SSP5-8.5 warming scenario. 30

Figure 2.9 Deep ocean carbon accumulation and meridional overturning rates in twelve CMIP6 models under SSP2-4.5 scenario. 32

Figure 2.10 Deep ocean carbon accumulation and meridional overturning rates in eight CMIP6 models under the SSP1-2.6 warming scenario. 33

Figure 2.11 Slowing SMOC rates on intermediate ocean carbon uptake. 34

Figure 2.12 Slowing SMOC rates on deep ocean carbon uptake. 35

Figure 2.13 Separating biology and circulation impacts on regenerated DIC accumulation in the deep ocean. 36

Figure 2.14 Partitioning of deep-ocean DIC storage in the offline model. 48

Figure 2.15 Comparison of the regenerated DIC accumulation calculated by the AOU method, TOU method and the offline model. 48

Figure 3.1 Ocean circulation and buoyancy frequency. 71

Figure 3.2 The separation of 17 surface patches. 72

Figure 3.3 The surface sources of global ocean waters. 74

Figure 3.4 The fraction of whole water column where it made its next contact with the surface at each ocean grid in the experiment of scenario1 (left panels) and scenario2 (right panels). 77

Figure 3.5 The global mean age. 79

Figure 3.6 The global mean first passage time. 82

Figure 4.1 Global map and time series of air-sea CO2 flux. 102

Figure 4.2 Global annual mean diagnostics from CESMv1. 104

Figure 4.3 The effects of climate-driven varying circulation, biology, sea surface temperature and piston velocity on air-sea CO2 flux and total carbon uptake. 107

Figure 4.4 The effects of climate-driven varying circulation, biology, sea surface temperature and piston velocity on air-sea CO2 flux and natural carbon storage. 109

Figure 4.5 The impacts of time-evolving circulation and biological processes on DIC vertical profiles. 112

LIST OF TABLES

Page

Table 2.1 CMIP6 model mean changes in physical and biogeochemical fluxes by 2100 under three climate scenarios. 22

Table 2.2 The CMIP6 models included in the MOC analysis. 37

Table 2.3 The CMIP5 models included in the MOC analysis. 38

Table 2.4 Model mean 1990s overturning rates from CMIP6 (36 models) and CMIP5 (24 models) for the Atlantic Meridional Overturning Circulation (AMOC) and the Southern Meridional Overturning Circulation (SMOC) cells are compared with observation-based estimates (reproduced from ref 28). 39

Table 4.1 The optimal model parameters. 97

Table 4.2 The configuration of sensitivity tests. 99

ACKNOWLEDGEMENTS

During the five years of pursuing my Ph.D. degree, I am profoundly grateful to my advisors, Prof. Keith Moore and Prof. François Primeau, for their invaluable guidance, support, and mentorship. Prof. Moore introduced me to the fascinating world of ocean carbon cycle. His patience, willingness to help, and understanding of the ups and downs have meant a lot to me, making my academic experience far more enjoyable and fulfilling than I could have imagined. Equally, I am indebted to Prof. Primeau, who embodies the ideal scientist I have always aspired to become. He not only provided invaluable insights into scientific problem-solving but also, transformed me from someone who once rushed through life with a utilitarian mindset to someone who learned to slow down and savor the beauty of life and the pursuit of science. His witty humor and engaging conversations have been therapeutic, especially during challenging times.

I would also like to extend my gratitude to Prof. James Randerson and Prof. Adam Martiny, my committee members, for their insightful suggestions during my annual committee meetings. Furthermore, I owe heartfelt thanks to former and present members in Moore and Primeau labs, Wei-Lei Wang, Weiwei Fu, JJ Becker, Ann Bardin, Tien-Yiao Hsu, Jun Yu, Nicola Wiseman, Megan Sullivan, Marina Fennell, Hanchao Chen and Kayla Mitchell, whose stimulating discussions have spurred me to delve into profound scientific questions. The Ocean Biogeochemistry Reading Group has also been a source of inspiration, providing an open and welcoming atmosphere for discussing science.

I extend my appreciation to friends within and outside the department. Your friendships have made me feel less lonely and isolated, especially during the pandemic. Last but certainly not least, I want to express my deepest gratitude to my beloved parents for their unconditional love and support over the years. Your unwavering belief in me has allowed me to focus fully on my research, ultimately making the completion of this dissertation a reality.

Chapter 2 of this dissertation is a reprint of the material as it appears in Nature Climate Change, used with permission from Nature Publishing Group. The co-authors in the publication are Dr. Keith Moore, Dr. François Primeau, Dr. James Randerson and Dr. Adam Martiny. Financial support was provided by University of California Irvine, and research grants from the U.S. Department of Energy (DE-SC0021267), Earth System Model Development and Regional and Global Climate Modeling programs.

To all of you who have touched my life during this journey, thank you.

VITA

Yi Liu

2015	B.S. in Environmental Science, Ocean University of China
2018	M.S. in Physical Oceanography, South China Sea Institute of Oceanology, Chinese Academy of Sciences
2020	M.S. in Earth System Science, University of California, Irvine
2023	Ph.D. in Earth System Science, University of California, Irvine

FIELD OF STUDY

Ocean Carbon Cycle; Ocean Biogeochemistry

PUBLICATIONS

[1] **Liu, Y.**, Moore, J. K., Primeau, F., & Wang, W. L. (2023). Reduced CO_2 uptake and growing nutrient sequestration from slowing overturning circulation. *Nature Climate Change*, 13(1), 83-90.

[2] **Liu, Y.**, Primeau, F. (2023). Surface-to-Interior Transport Timescales and Ventilation Patterns in a Time-Dependent Circulation Driven by Sustained Climate Warming. In review at *Journal of Physical Oceanography*.

ABSTRACT OF THE DISSERTATION

Understand the Role of Global Meridional Overturning Circulation

on the Ocean Carbon Sink

by

Yi Liu

Doctor of Philosophy in Earth System Science

University of California, Irvine, 2023

Professor J. Keith Moore, Irvine, Chair

The oceans play an important role in regulating atmospheric CO_2 levels and the climate system. Since the beginning of the Industrial Revolution, the ocean has absorbed more than 25% of anthropogenic CO_2 emissions, and the carbon sink is expected to grow over the next several centuries as atmospheric CO_2 concentrations rise. Multiple ocean processes, however, affect the amount of anthropogenic carbon that the ocean absorbs from the atmosphere. This thesis combines Earth System Models (ESM) from the sixth phase Coupled Model Intercomparison Project (CMIP6) with an offline inverse biogeochemical model to answer a fundamental question: What mechanisms control the size of the ocean carbon sink in a warming climate?

First, I use the CMIP6 models to investigate the role of meridional overturning circulation in ocean carbon uptake (Chapter 2). Slowing MOC reduces anthropogenic carbon uptake by the solubility pump while increasing deep ocean carbon and nutrient storage by the biological pump. The net effect is a reduction in the ocean carbon sink.

I then used an offline inverse biogeochemical model to conduct a series of sensitivity experiments to better understand how changes in circulation affect the ocean carbon sink (Chapter 3). The results show that slowing MOC reduces anthropogenic carbon uptake by decreasing biological productivity. The slowing MOC sequesters more nutrients in the deep ocean, reducing nutrient replenishment to the upper ocean and thus lowering biological productivity. This increases ocean surface CO_2 saturation and reduces the ocean's ability to absorb anthropogenic CO_2 from the atmosphere. However, without taking into account changes in biological productivity, the slowing MOC contributes little to the ocean carbon sink.

In Chapter 4, I examine the ocean ventilation timescales and patterns in a time-evolving circulation in the context of climate change. I found that slowing meridional overturning circulation causes a 110-year increase in global-averaged mean age from the year 1850 to 2300. However, where and when the water will be re-exposed to the atmosphere is highly dependent on the post-2300 circulation. The dependence of interior-to-surface transit time on future ocean circulation produces great uncertainties in the long-term durability of the ocean CDR strategies.

Chapter 1: Introduction

1.1 The ocean carbon sink

A global agreement on climate change The Paris Agreement aims to limit global average temperature increase to less than 2°C or 1.5°C above preindustrial levels. To meet the climate targets, strict carbon emission reductions and "negative emission" strategies (Carbon Dioxide Removal, hereafter CDR) are required. The foundation of meeting these climate targets is accurately calculating the allowable amounts of additional emissions as well as the efficacy of CDR strategies for enhancing natural carbon sinks. However, the calculations, which are heavily reliant on future global carbon sinks, have large uncertainties (Jones and Friedlingstein, 2020; Keller et al., 2018).

Since the Industrial Revolution, the ocean has absorbed more than 25% of anthropogenic CO_2 emissions (Friedlingstein et al., 2022), and this carbon sink is projected to continue growing over the next several centuries (Randerson et al., 2015; Jones et al., 2016). However, accurately estimating the contemporary and future ocean carbon sink using Earth System Models (ESMs) is challenging, and there are significant uncertainties with large regional biases in the current era compared to observation-based products (McKinley et al., 2017; Kessler and Tjiputra, 2016; Fay and McKinley, 2021). The uncertainty of the future ocean carbon sink (Terhaar et al., 2022: 150±11 PgC to 399±29 PgC depending on the climate scenarios) contributes significantly to the uncertainties of allowable additional emissions (i.e., 416±90 PgC (Schurer et al., 2018)). Furthermore, the large uncertainty in the CMIP6 ESMs implies a lack of comprehensive understanding of the carbon cycle, which adds uncertainty to the calculation of the durability of some marine carbon dioxide removal (mCDR) strategies that aim to sequester CO_2 in the deep ocean.

In estimating the contemporary and future ocean carbon sink, ESMs include uncertainties arising from various sources such as model structure, initialization, and emission scenarios. Among these, emission scenarios contribute most significantly to the considerable spread of ESMs concerning the future ocean carbon sink, posing a challenge that is difficult to minimize. Differences in the parameterization of ocean processes and initial conditions across models primarily account for the remaining spread. These uncertainties underscore the existing gaps in our understanding of ocean processes, including physical and biogeochemical aspects, such as the unclear roles of large-scale ocean circulation and ocean biology in modulating the ocean carbon sink. A recent study by McKinley et al. (2023) suggests that constraining the contemporary ocean carbon sink estimation could reduce the model spread of the future global ocean carbon sink by approximately 50%. However, the influence of individual ocean processes on the spread of the ocean carbon sink estimated by ESMs remains unclear.

1.2 Natural and anthropogenic ocean carbon

The ocean serves as a vast reservoir of inorganic carbon, with continuous exchange occurring between the ocean and the atmosphere. It includes both natural and anthropogenic components of carbon. The natural CO_2 pool is part of the ocean's dissolved inorganic carbon (DIC) pool that existed in the preindustrial era, whereas the anthropogenic component represents the carbon that the ocean takes up from rising atmospheric CO_2 due to anthropogenic perturbation.

1.2.1 The natural carbon cycle

The preindustrial level of atmospheric CO_2 was approximately 280 ppm, and the role of ocean carbon pumps in maintaining this level of atmospheric CO_2 is crucial (Henson et al., 2017). In the absence of the ocean carbon pump, the preindustrial atmospheric CO_2 levels would have been as high as 583 ppm (DeVries, 2022).

The carbon pumps also modulate the DIC distribution in the ocean. The most striking feature of DIC in the ocean is its robust vertical gradient, characterized by lower concentrations near the surface and higher concentrations in deeper waters. This gradient enables the ocean to absorb additional carbon from the atmosphere, thus mitigating climate change. Ocean carbon pumps, primarily the biological and solubility pumps, are responsible for maintaining these gradients (Volk and Hoffert, 1985). Approximately two-thirds of the ocean's vertical DIC gradients can be attributed to the biological pump, while the remaining third is a result of the solubility pump (DeVries, 2022). A comprehensive understanding of ocean carbon pumps is essential for deciphering both the natural carbon cycle and anthropogenic carbon uptake resulting from human-induced increased atmospheric CO_2.

The biological pump transfers carbon dioxide (CO_2) from the atmosphere into the deep ocean. This process involves photosynthetic organisms, such as phytoplankton, absorbing carbon and then sinking organic matter and calcium carbonate shells to the deep ocean. The strength of the biological pump is primarily determined by surface water productivity and the export of some of this production. Factors such as nutrients, temperature, and light regulate phytoplankton growth, thereby influencing the strength and efficiency of biological pump. Globally, the biological pump has a strength of 5-13 PgC/yr, with significant spatial variations (e.g., Henson et al., 2011; Henson et al., 2022; Nowicki et al., 2022). As phytoplankton consume nutrients and generate organic matter, some of which sink into the ocean's depths, upper ocean nutrients become depleted. To maintain marine biological productivity, ocean circulation must ultimately return these sinking nutrients to the upper ocean (Palter et al., 2010; Moore et al., 2018). Ultimately, the strength and efficiency of the biological pump are controlled by both biological processes and physical processes such as ocean circulation. The solubility pump is another critical contributor to the ocean carbon sink, accounting for approximately 1/3 of the DIC vertical gradients (DeVries, 2022). It operates based on the principle that carbon dioxide is more soluble in cold water. As cold water is denser, it is more likely to sink into the deep ocean, taking dissolved CO_2 along with it (Volk and Hoffert, 1985). As a result, the solubility pump is driven by a combination of ocean chemistry and ocean circulation. This process helps maintain the ocean's ability to absorb additional carbon from the atmosphere and contributes significantly to the overall ocean carbon sink, collaborating closely with the biological pump to regulate Earth's carbon cycle and climate system.

Recent and projected climate warming alters natural carbon cycling via multiple pathways, including CO_2 solubility, ocean circulation, and ocean carbon pumps. As ocean temperatures rise, CO_2 solubility in water decreases, leading to natural carbon outgassing from the surface. The stronger upwelling in the Southern Ocean driven by stronger westerlies is also a potential reason for natural carbon outgassing. The reduced carbonate buffer factor also emitted some natural carbon into the atmosphere (Holzer and DeVries, 2022). Changes in the biological pump are also an important factor in modulating natural carbon cycling. The strength of the biological pump is projected to decline in most Earth

System Models due to increased nutrient stress in the upper ocean (Henson et al., 2022; Fu et al., 2016). However, physiological responses and phytoplankton community shifts may partially mitigate this stress by requiring fewer nutrients with higher stoichiometric ratios (Kwon et al., 2022). Although the weakened biological pump reduces carbon injection into the deep ocean, the slower overturning circulation allows more time for carbon buildup before eventual release back to the atmosphere (Matear et al., 1999; Bernardello et al., 2014).

1.2.2 The anthropogenic carbon uptake

The ocean accounts for approximately 40% of the total anthropogenic carbon absorption from the atmosphere since the preindustrial era. The concept of the oceanic anthropogenic carbon sink is a combination of the absorption of newly emitted carbon and alterations in the ocean's natural inventory caused by climate-induced shifts in temperatures, winds, and freshwater cycles (Frolicher and Joos, 2010; McNeil and Matear, 2013). Notably, the Southern Ocean contributes to a larger proportion of anthropogenic carbon uptake compared to other ocean basins (Gruber et al., 2019; Prend et al., 2022).

Historically, data-constrained estimates indicate that the ocean has absorbed approximately 33.0±4.0 PgC from 1994 to 2007 (Gruber et al., 2019). Conversely, Earth System Models, including both CMIP5 and CMIP6 models, present lower estimates of carbon uptake at around 27.8±0.5 PgC (Fu et al., 2022). This discrepancy might be attributable to a weakened exchange from the surface to the ocean's interior.

In a changing climate, estimating the future ocean carbon sink presents significant challenges. However, current oceanic conditions, such as overturning circulation, ocean stratification and the Revelle factor can help constrain some uncertainties. Employing these emergent constraints could decrease uncertainties around future anthropogenic carbon uptake by 32%-62%, depending on the warming scenarios (Terhaar et al., 2022). Furthermore, constraining present-day carbon sinks can reduce approximately 50% of the uncertainty in the future ocean carbon sink (McKinley et al., 2023). The trajectory of future ocean carbon sinks also heavily relies on prescribed climate scenarios. For instance, under a "business-as-usual" scenario, the ocean would absorb approximately 750 PgC of anthropogenic carbon from the preindustrial era until 2100. Under the scenario with emission mitigation, this value reduces to 380 PgC (Ridge and McKinley, 2021). While the ocean carbon sink mirrors atmospheric CO_2 emissions to some extent, the time-evolving ocean physical and biological processes also influence the magnitude of the sink.

Previous studies argue that the reduced buffer factor primarily influences the ocean carbon sink under both moderate and business-as-usual warming scenarios (Ridge and McKinley, 2021; Chikamoto and DiNezio, 2021). The temperature-driven decreased CO_2 solubility, along with other mechanisms, such as variable overturning circulation and the biological pump, also affect carbon uptake by modulating the surface ocean's DIC, alkalinity (ALK), and air-sea CO_2 disequilibrium.

1.3 The global overturning circulation

The Meridional Overturning Circulation (MOC) is a key component of global ocean circulation, playing a vital role in heat and nutrient distribution as well as the ocean carbon sink. The MOC consists of two primary cells: the abyssal cell Southern Ocean Meridional Overturning Circulation (SMOC), driven by Antarctic Bottom Water (AABW) formation and the upwelling of Circumpolar Deep Water (CDW), and the upper cell Atlantic Meridional Overturning Circulation (AMOC), driven by North Atlantic Deep Water (NADW) formation.

The MOC interacts with the upper ocean circulation, thereby affecting both natural carbon cycling and anthropogenic carbon uptake. In the Antarctic Divergence, deep ocean nutrients upwell to the surface and travel northward, further spreading into the Subantarctic Mode Water (SAMW) and Antarctic Intermediate Water (AAIW) formation regions via Ekman transport. SAMW, enriched with nutrients from thick wintertime mixed layers, move northward into the thermocline, fueling low-latitude biological productivity through upward transport in equatorial regions.

A slowing global meridional overturning circulation combined with intensifying upper ocean stratification affects the ocean carbon sink. This slowdown is hypothesized to sequester more nutrients in the deep ocean, leading to a potential decrease in surface nutrient levels and biological productivity (Moore et al., 2018). Yet, it also allows carbon to remain in the deep water longer before resurfacing. The weakening exchange between surface and deep water could hinder the transfer of anthropogenic carbon from the surface to the ocean interior, thereby accumulating carbon at the surface and reducing the ocean's uptake of additional anthropogenic carbon from the atmosphere. Untangling the complex influence of varying overturning circulation on the oceanic carbon sink poses a considerable challenge.

1.4 Research questions

This thesis mainly focuses on how ocean circulation and biological processes affect the ocean carbon sink. Also, how the time-evolving circulation will affect the ventilation timescales and further the efficacy of some ocean CDR strategies. This thesis is divided into three main chapters.

In Chapter 2, I will focus on the role of time-evolving global overturning circulation on the ocean carbon sink. Previous studies have primarily focused on the variability and trends of AMOC, while the control of the SMOC on the ocean carbon sink has been largely ignored. This chapter aims to address this gap in knowledge by analyzing all CMIP6 models, in conjunction with an offline biogeochemical model, to investigate the effects of a slowdown in SMOC on nutrient availability, biological productivity, and the ocean carbon sink. Our findings indicate that a slowdown of the SMOC will deplete surface nutrients and decrease export production, but it will increase the efficiency of the biological pump, resulting in the sequestration of more regenerated carbon. This slowdown, however, will weaken the solubility pump by transporting less anthropogenic carbon into the deep ocean and ultimately lead to a reduction in the ocean carbon sink.

In Chapter 2, I investigate how the ocean carbon sink is affected by a slowdown in overturning circulation under different warming scenarios using CMIP6 models. However, we still don't fully understand the specific mechanisms by which this slowdown affects both natural and anthropogenic carbon, nor do we have a clear picture of how other oceanic processes, like sea surface temperature, biology, and air-sea CO_2 exchange, impact the ocean carbon sink. To address these gaps in knowledge, we integrated time-evolving circulation into an inverse biogeochemical model to analyze the contributions of each oceanic process to the ocean carbon sink in chapter 3. Our results indicate that while increased temperature leads to natural carbon outgassing, the slowing overturning circulation and the associated decrease in export production, has the greatest impact on the total ocean carbon sink.

Chapters 2 and 3 help us understand the crucial role that oceanic processes play in regulating the ocean carbon sink. However, the impact of time-evolving circulation on ventilation timescales and patterns is equally important, as it directly influences the sequestration timescales and durability of ocean carbon dioxide removal (CDR) strategies that aim to sequester carbon in the deep ocean. In chapter 4, we expand on the theory of water mean age and mean first-passage time by incorporating time-evolving circulation. Our findings indicate that a slowdown in overturning circulation results in older deep water, but younger upper ocean. However, the estimation of mean first-passage time, i.e., the length of time a tracer can remain in the water before reaching the surface, is highly dependent on future circulation patterns beyond the year 2300, when our simulation ends. As a result, there are significant uncertainties in our estimation of mean first-passage time.

In chapter 5, I provide a summary of this dissertation and give an overview of the impacts of slowing overturning circulation on the ocean carbon sink and its potential impacts on the durability of mCDR strategies. Furthermore, I contemplate prospective future research directions.

Chapter 2: Reduced CO_2 Uptake and Growing Nutrient Sequestration from Slowing Overturning Circulation

Abstract

Current Earth System Models (ESMs) project dramatic slowing (28%-42% by 2100) of Atlantic Meridional Overturning Circulation (AMOC) and Southern Meridional Overturning Circulation (SMOC) across a range of climate scenarios, with a complete shutdown of SMOC possible by year 2300. Slowing meridional overturning circulation (MOC) differentially impacts the ocean biological and solubility carbon pumps, leaving the net impact on ocean carbon uptake uncertain. Here using a suite of ESMs, we show that slowing MOC reduces anthropogenic carbon uptake by the solubility pump, but increases deep ocean storage of carbon and nutrients by the biological pump. The net effect reduces ocean uptake of anthropogenic CO_2. The deep-ocean nutrient sequestration will increasingly depress global-scale, marine net primary production (NPP) over time. MOC slowdown represents a positive feedback that could extend or intensify peak-warmth climate conditions on multicentury timescales.

This chapter appeared as a publication in Nature Climate Change.

Liu, Y., Moore, J.K., Primeau, F., Wang, W.L., (2023), Reduced CO_2 uptake and growing nutrient sequestration from slowing overturning circulation. *Nat. Clim. Chang.* **13**, 83–90. https://doi.org/10.1038/s41558-022-01555-7.

Main text

The global Meridional Overturning Circulation (MOC), comprised of the Atlantic-based upper MOC cell (AMOC) and the deeper Southern MOC cell (SMOC), strongly impacts climate and marine biogeochemistry (Jahn et al., 2013; Matear et al., 1999; Plattner et al., 2001; Schmittner, 2005; Whitt et al., 2020; Katavouta and Williams, 2021). Earth System Models (ESM) from the Coupled Model Intercomparison Project (CMIP6) project rapidly declining AMOC rates over the 21st century (Katavouta and Williams, 2021; Weijer et al., 2020; O'Neill et al., 2016). Recent observations suggest declining North Atlantic Deep Water (NADW) formation and slowing of AMOC are underway and already impacting biological productivity (Thornalley et al., 2018; Caesar et al., 2018; Osman et al., 2019). A recent study of eleven CMIP6 models found a strong link between Atlantic basin carbon storage and slowing AMOC (Katavouta and Williams, 2021). There have been fewer studies of SMOC response to climate warming, particularly with ESM projections that extend beyond year 2100 (Moore et al., 2018; Frölicher et al.,2020; Beadling et al., 2020; Heuzé, 2021).

The oceans play a critical role in removing anthropogenic CO_2 from the atmosphere (Sabine et al., 2004; Gruber et al., 2019). Global ocean dissolved inorganic carbon (DIC) concentrations have increased over time as the oceans take up anthropogenic CO_2, driven by rising atmospheric CO_2 concentrations (Sabine et al., 2004; Gruber et al., 2019). Both the biological and solubility carbon pumps contribute to ocean CO_2 sequestration. The solubility pump refers to the combined influences of ocean circulation and inorganic carbon chemistry that contribute to uptake and storage of carbon dioxide, helping maintain observed vertical gradients of DIC (higher concentrations at depth). The biological pump refers to the biogenic export of carbon to the interior ocean (as sinking particulate organic carbon (POC), sinking calcium carbonate ($CaCO_3$), and transported dissolved organic matter), which modifies surface carbon chemistry and air-sea CO_2 exchange. CMIP5 ESMs project weakening biological carbon export from surface waters over the 21st century, generally with larger decreases under stronger warming scenarios (Bopp et al., 2013; Fu et al., 2016; Laufkötter et al., 2016).

Slowing meridional overturning circulation weakens carbon uptake by the solubility pump, but allows more time for exported biogenic carbon to accumulate at depth, increasing deep ocean carbon and nutrient storage by the biological pump (Matear et al., 1999; Plattner et al., 2001; Schmittner, 2005; Whitt et al., 2020; Katavouta and Williams, 2021; Frölicher and Joos., 2010; Bernardello et al., 2014; Ito, 2015; DrVries et al., 2017; Ödalen et al., 2018). Previous studies often focused on a single model, assumed steady state circulation, or focused on the paleoclimate context. MOC impacts on global ocean carbon uptake and the underlying mechanisms across multiple warming scenarios remain unclear, as all these multiple processes are integrated in ESMs and the relative roles of these processes may be changing over time, making it difficult to disentangle. Here, we diagnose the effects of slowing overturning circulation on the ocean carbon sink in the context of a warming climate with a suite of CMIP6 ESM projections along three potential future climate scenarios. We also incorporate a new offline model based on output from the CESMv1(BGC) CMIP5 RCP8.5-ECP8.5 simulation (Moore et al., 2018) (hereafter CESMv1-RCP8.5). Simulations with the offline model allow us to more accurately diagnose the changing contributions of different processes to carbon sequestration over time in the CESMv1-RCP8.5 simulation (Methods for details).

Climate Warming Slows Meridional Overturning Circulation

We calculate the changing rates of overturning in the Atlantic-based upper MOC cell (AMOC) and for the global Southern MOC cell (SMOC) for a suite of thirty-six CMIP6 models and twenty-four CMIP5 models to year 2100 across multiple climate scenarios (CMIP5 Representative Concentration Pathway (RCP) 8.5, and CMIP6 Shared Socioeconomic Pathways (SSP) 1-2.6, SSP2-4.5 and SSP5-8.5). Radiative forcing at 2100 is the same for the two high-end scenarios, but with a modestly different relative contribution from different greenhouse gases. We extend this analysis to year 2300 for the six CMIP6 models with output available on the Earth System Grid Federation (ESGF) (tables S1-S2 in Supplementary Information, hereafter SI). The RCP8.5 and SSP5-8.5 are high-end warming, emissions-as-usual scenarios, SSP2-4.5 has more moderate warming, and SSP1-2.6 is a stabilization scenario aimed at keeping mean surface warming below 2^{o}C (O'Neill et al., 2016). The CMIP6 mean AMOC rate (maximum overturning at 30^{o}N) for the present climate (1990s) is 19.2±4.5 Sv, which matches well with the estimate of 17.0±4.4 Sv from the RAPID project (27) and other observation-based estimates (Cessi, 2019) (Fig. 2.1, table 4). However, all CMIP6 models underestimate SMOC rate (maximum overturning at 30^{o}S) compared to the observational estimates (Fig. 2.1, Fig. 2.6, table 4). Despite these model discrepancies there is a robust trend across the models of declining overturning rates in both AMOC and SMOC as the climate warms.

There is a dramatic future slowing of both MOC cells on the high-end warming scenarios (RCP8.5, SSP5-8.5) that extends well beyond year 2100 (Fig. 2.1, Fig. 2.6). The

CMIP6 model-mean AMOC rate steadily declines over the 21st century (Katavouta and Williams, 2021) before stabilizing at a much-reduced rate (Fig. 2.1A), similar to the CMIP5 models (Fig. 2.6). Overturning rates for both MOC cells also decline to year 2100 under the more moderate warming scenarios (Fig. 2.2, Fig. 2.6). SMOC slows as polar salinity-driven stratification intensifies (Fig. 2.7, SI) and appears to be shutting down completely by year 2300 in available CMIP6 SSP5-8.5 models, similar to the pattern in the CESMv1-RCP8.5 simulation (Fig. 2.1, Fig. 2.6, SI). Both AMOC and SMOC slow with climate warming, but there is a range of responses across models and climate scenarios (Figs. 2.1-2.2, table 2.1). There is considerable variability in the degree of MOC slowdown, with the inter-model differences often larger than the variability across different climate scenarios with the same model. Thus, there is broad agreement in projecting rapidly declining MOC rates this century, but substantial uncertainty remains in the magnitude of MOC slowing and in the tipping points related to potential MOC shutdown in the centuries beyond.

Reduced Ocean Carbon Uptake from Slowing SMOC

To understand the time-dependent contributions of the biological and solubility pumps to global ocean carbon uptake, we partition DIC into the regenerated and preformed components using the apparent oxygen utilization (AOU), and define the strength of the biological and solubility carbon pumps in a changing climate as the accumulation rate of the regenerated DIC and preformed DIC, respectively, relative to the preindustrial for thirteen CMIP6 models and the CESMv1-RCP8.5 simulation.

We find increasing ocean carbon storage (full depth) in every model with most of the accumulation as preformed DIC at intermediate depths (100-2000 m, Fig. 2.2, table 2.1). The whole ocean regenerated DIC storage ranges widely across these models from +5 to +142 PgC, accounting for 1% to 30% (mean 15%) of the total ocean carbon storage by 2100 (Fig. 2.2). Yet in the deep ocean (> 2000m) regenerated DIC accounted for ~50-100% of the carbon accumulation and increases over the 21st century across the CMIP6 models and different warming scenarios (Fig. 2.2, Figs. 2.8-2.10, table 2.1). Differences in deep ocean regenerated carbon accumulation are limited across the warming scenarios, even though both AMOC and SMOC tend to slow more with stronger climate warming (table 2.1). Storage of preformed carbon in the deep ocean increases at a slower rate or in some models declines over the 21st century (Fig. 2.2, Figs. 2.8-2.10). Thus, the biological pump is coming to dominate deep ocean (> 2000 m) carbon storage by 2100 in most of the CMIP6 models, particularly under stronger climate warming scenarios (SSP2-4.5 and SSP5-8.5 scenarios).

Regenerated DIC is also accumulating at intermediate depths, but this accumulation scales more strongly with degree of climate warming across the CMIP6 scenarios (Fig. 2.2, table 2.1). The accumulation of regenerated DIC by the end of this century is correlated with the changes in export production normalized by the slowdown of SMOC, because the accumulation of regenerated DIC is controlled by the changes in surface export production, which injects carbon into ocean interior, and by the changes of SMOC, which is an indicator of ocean interior residence time and the potential to accumulate regenerated DIC. This correlation is valid across CMIP6 SSP1-2.6, SSP2-4.5 and SSP5-8.5 warming scenarios (Fig. 2.3). Furthermore, it is also valid in the intermediate and deep ocean (Figs. 2.11-2.12).

We hypothesize that slowing of the MOC will reduce the capacity of the oceans to take up anthropogenic CO_2 on multicentury timescales in the context of increasing atmospheric CO_2. Slowing SMOC should weaken the solubility pump, as it controls ventilation of the ocean interior on multicentury timescales. Great amounts of preformed DIC are accumulating at intermediate depths (100 - 2000m) in CMIP6, but little of this is making it into the deep ocean, in part due to slowing MOC (Fig. 2.2, table 2.1). We find significant correlations between the slowing of SMOC and both preformed and total ocean DIC storage by 2100 across CMIP6 SSP1-2.6, SSP2-4.5 and SSP5-8.5 projections for models with necessary output available on the ESGF (Fig. 2.3). The models with the greatest slowing of SMOC take up the least preformed and total DIC. The declines in SMOC can explain 39%-51% of the variance in ocean carbon storage by the solubility pump by 2100 depending on the warming scenarios (Fig. 2.3). The storage of regenerated DIC only partially makes up the difference between preformed and total DIC storage (Fig. 2.3). If we consider intermediate and deep ocean separately, the same correlation holds true in the intermediate ocean (Fig. 2.11), but in the deep ocean, the correlation becomes much weaker as the deep ocean has longer ventilation time which does not allow as much preformed DIC accumulation in the deep ocean by 2100 and the impacts of slowing SMOC on regenerated DIC and preformed DIC partially cancel out, resulting in no obvious correlation to total DIC (Fig. 2.12).

We examine centennial timescale changes in carbon and nutrient accumulation rates (relative to preindustrial) in the CESMv1-RCP8.5 to better illustrate processes happening across the CMIP6 models. DIC storage rate peaks in the 21st century and declines in ocean uptake out to year 2300 (Fig. 2.4). The accumulation of DIC is initially much larger in surface waters than at depth, due to direct uptake of anthropogenic CO_2 from the atmosphere.

However, the movement of carbon from the surface to the interior by circulation eventually dominates over the transfer of carbon from the atmosphere to the oceans, causing the relative contribution of surface ocean DIC storage to decrease. The strongest accumulation rate progressively shifts to intermediate depth waters (Fig. 2.4). Preformed DIC dominates accumulation at intermediate depths (100 - 2000m), but little has reached the deep ocean, even by 2300, largely due to slowing MOC (Fig. 2.4, table 2.1). Preformed DIC accumulation rates decline at all depth levels after 2100, with very little accumulation in the deep ocean and no surface accumulation (< 100m) of preformed DIC in the 2200s. The accumulation rate of preformed DIC at intermediate depths slows substantially in the 2200s compared to the previous two centuries, but still accounts for most of the total carbon storage over the 23rd century (Fig. 2.4).

During 20th century, CESMv1-RCP8.5 accumulation of carbon in the deep ocean (> 2000m) is dominated by the solubility pump (~67%), but the biological pump comes to dominate deep-ocean carbon storage (Fig. 2.4). By 2100, the biological pump accounts for 65% of the deep-ocean DIC accumulation, increasing to 85% by 2300 (Fig. 2.4). Thus, the biological pump comes to dominate deep-ocean carbon storage with strong climate warming in the CESMv1-RCP8.5, as seen in the CMIP6 models (Fig. 2.2, Figs. 2.8-2.10). The biological pump is also sequestering nitrate and phosphate in the deep ocean, with large upper-ocean declines balanced by increasing deep ocean concentrations (Fig. 2.4). In 2200s, both the preformed and regenerated DIC keep accumulating in the ocean, but the declines of accumulation rates of preformed DIC are far larger than the declines in regenerated DIC accumulation rates compared to 2100s (Fig. 2.4). Thus, the total rate of CO_2 uptake from the atmosphere is declining just as atmospheric CO_2 concentrations and surface temperatures are approaching peak values (O'Neill et al., 2016; Moore et al., 2018).

To better understand the changing regenerated DIC distributions, we separate the effects of decreasing surface export flux from the effects of slowing MOC on regenerated carbon distributions with the offline model. We perform a decomposition of the carbon accumulation using offline simulations in which the biological source terms and the circulation are prescribed factorially to be either time-varying or fixed to their preindustrial values (1850s) as simulated with the online ESM (SI). These offline simulations provide a clean separation of the influences of time-varying physical and biological processes. We diagnose the carbon fluxes for CESMv1-RCP8.5 with the offline model, separating the contributions of sinking biological fluxes and the time-varying ocean circulation fluxes across the 100m and 2000m depth horizons, comparing the steady-state preindustrial fluxes with the changing accumulation rates averaged over the 21st and 23rd centuries (Fig. 2.5). The sinking biogenic carbon fluxes at both depths decline over time by ~30%. However, the return of deep-ocean, regenerated DIC back to the surface by the circulation declines even more, from 0.76 PgC/yr preindustrial to 0.38 PgC/yr in the 21st century, and even brings (-0.04 PgC/yr) upper ocean regenerated DIC back to the deep ocean in the 23rd century (Fig. 2.5). The imbalance leads to net storage of regenerated carbon, nitrogen and phosphorus in the deep ocean, depressing upper-ocean nutrient concentrations (Figs. 2.4-2.5). With available model output, we could separate the impacts of changing surface export and circulation on regenerated DIC accumulation for CESMv1-RCP8.5 and for three CMIP6 projections. In each of these projections the biological export from surface waters declines over the 21st century. Thus, all of the increasing deep-ocean regenerated DIC accumulation is due to slowing MOC (Fig. 2.13, table 2.1).

Discussion and Conclusions

The CMIP6 ESMs consistently project dramatic slowing of AMOC and SMOC across a wide range of future climate scenarios. There are substantial differences across the models in both the magnitude of MOC slowing and in how strongly it scales with the degree of climate warming (Figs. 2.1-2.2, Figs. 2.6-2.7). On the low-end warming scenario (SSP1-2.6) both MOC cells stabilize after year 2100, but at rates greatly reduced from the preindustrial (-37% for AMOC, -67% for SMOC). There are no signs of MOC recovery by year 2300. On the high-end warming scenario (SSP5-8.5), SMOC appears to collapse completely by 2300 (Fig. 2.1, SI).

Slowing MOC increases the efficiency of the biological pump. Global-scale primary production and surface biogenic carbon export will decline as critical nutrients are increasingly sequestered in the deep ocean, along with community shifts from larger phytoplankton to smaller phytoplankton under increasing nutrient stress (Moore et al., 2018, Fu et al., 2016) until at some point MOC becomes more vigorous again (13). Despite the declining or flat surface export production, nearly all of the models show increasing storage of regenerated DIC over this century, due to the MOC slowing (Fig. 2.2, Fig. 2.13, table 2.1). In the near term, the increasing sequestration efficiency of the biological pump, driven by the MOC slowdown, leads to net removal of CO_2 from the atmosphere, partially compensating for the weakening solubility pump. However, a substantial pulse of CO_2 could be released back to the atmosphere when a more vigorous MOC eventually returns. Some studies have suggested a returning MOC strength after several hundred years (Frölicher et al., 2020, Frölicher and Joos, 2010; Ito et al., 2014, Schmittner et al., 2008; Yamamoto et al., 2015; Battaglia and Joos, 2018). These coarse resolution and intermediate complexity models did not include active ice sheets and may not accurately capture the long term climate impacts on MOC. The longer residence time in the deep ocean allows more accumulation of regenerated carbon and nutrients at depth, but it also allows more oxygen to be consumed before water masses are again ventilated at the surface. Slowing MOC will exacerbate the expected declines in ocean oxygen content, driven primarily by warming effects on solubility and increasing upper ocean stratification (Koeve et al., 2020, Levin et al., 2018). MOC shutdown could eventually lead to an anoxic deep ocean, which has contributed to past mass extinction events (Brennecka et al., 2011).

Slowing MOC weakens the solubility pump's capacity to take up and store anthropogenic CO_2 on multicentury timescales. The increasing efficiency of the biological pump only partially compensates for much larger decreases in solubility pump efficiency (i.e., preformed DIC accumulation) as circulation changes and surface waters saturate with CO_2 (Figs. 2.2-2.5). Thus, slowing of MOC with climate warming will weaken ocean uptake of CO_2, potentially extending hot climate conditions by hundreds to even thousands of years (Steffen et al., 2018; Holzer et al., 2020; Plattner et al., 2008; Clark et al., 2016; Frölicher and Paynter, 2015; Hajima et al., 2020). Elevated air temperatures and high CO_2 concentrations could last for millennia with a persistent collapse of MOC, which would prevent the deep ocean from contributing to CO_2 drawdown. The timescale for AABW to return to the surface had already increased by 2000 years as of the 2090s due to the rapid slowing of SMOC in one ESM (Holzer et al., 2020). The intermediate complexity models used to generate the CMIP6 climate scenarios lack realistic ocean circulation (O'Neill et al., 2016) and so likely overestimate ocean CO_2 uptake by not properly accounting for the impacts of MOC slowdown as climate warms. This means larger reductions in greenhouse gas emissions than previously estimated may be necessary to achieve the targeted radiative forcing trends, and for the more moderate scenarios, the climate stabilization goals.

Millennial timescale ESM projections are necessary to understand the impacts of global warming on ocean circulation, biogeochemistry, and marine ecosystems, and to evaluate associated potential climate feedbacks and tipping points (Steffen et al., 2018; Holzer et al., 2020; Plattner et al., 2008; Clark et al., 2016; Frölicher and Paynter, 2015; Hajima et al., 2020). However, few previous studies have included active ice sheet dynamics, and so are missing the massive freshwater inputs from the Greenland and Antarctica that will come with climate warming, and the corresponding impacts on ocean circulation and biogeochemistry (Hu et al., 2009; Lago et al., 2019; Kwiatkowski et al., 2019; Mackie et al., 2020). These freshwater inputs will further stratify polar regions, inhibiting deep water formation. Thus, inclusion of active ice-sheet dynamics in the ESMs will likely further weaken MOC (Levin et al., 2018) relative to the CMIP6 results presented here, potentially contributing to a shutdown of the deep-water formation that drives both MOC cells. Some CMIP6 models form Antarctic Bottom Water (AABW) through an unrealistic, open ocean convection, missing important shelf and coastal processes that influence AABW in the observations, including dynamic ocean-ice sheet interactions (Heuzé, 2021). Deep water formation results from complex interactions between the oceans, the atmosphere, sea ice, and ice sheets, often at spatial scales smaller than current ESM grid cells can represent. Improved representation of the deep-water formation processes that drive the MOC cells should be a top priority for ESM development (Katavouta and Williams, 2021; Beadling et al., 2020; Heuzé, 2021) as these processes will largely determine the long-term trajectory of ongoing climate perturbation. As humanity moves to reduce greenhouse emissions, there is a great need to explore millennial timescale climate change with state-of-the-art ESMs to better understand the full consequences of greenhouse gas emissions for planet Earth (Moore et al., 2018; Frölicher et al., 2020; Steffen et al., 2018; Holzer et al., 2020; Plattner et al., 2008; Clark et al., 2016; Frölicher and Paynter, 2015; Hajima et al., 2020).

Table 2.1. CMIP6 model mean changes in physical and biogeochemical fluxes by 2100 under three climate scenarios. Shown are the mean changes in meridional overturning circulation rates and in the sinking flux of particulate organic carbon at 100m depth from CMIP6 models (2080-2099 mean relative to 1850-1869 mean for each model) across a range of warming scenarios. For each calculation we include all CMIP6 models with all necessary output available on the Earth System Grid Federation (ESGF). "n" is the number of models with necessary variables.

	SSP1-2.6	SSP2-4.5	SSP5-8.5
ΔAMOC (Sv)	-5.1±3.0 (-28.8%±16.4%) (n=24)	-6.0±2.6 (-33.6%±14.2%) (n=26)	-7.3±2.7 (-41.7%±13.8%) (n=28)
ΔSMOC (Sv)	-3.6±1.9 (-33.2%±14.1%) (n=24)	-4.0±2.0 (-37.9%±13.7%) (n=26)	-4.6±2.3 (-41.9%±14.8%) (n=28)
ΔEP (PgC/yr)	-0.4±0.2 (-4.5%±4.0%) (n=11)	-0.6±0.3 (-6.9%±5.7%) (n=12)	-1.1±0.5 (-12.3%±8.2%) (n=13)
ΔpreDIC (100-2000m, PgC)	220.5±32.1 (n=11)	273.6±37.1 (n=12)	364.2±46.6 (n=13)
ΔpreDIC (>2000m, PgC)	24.4±24.0 (n=11)	22.1±25.1 (n=12)	21.8±24.4 (n=13)
ΔregDIC (100-2000m, PgC)	15.9±16.7 (n=11)	21.7±18.1 (n=12)	31.7±20.1 (n=13)
ΔregDIC (>2000m, PgC)	34.0±30.1 (n=11)	36.3±29.3 (n=12)	37.3±28.7 (n=13)

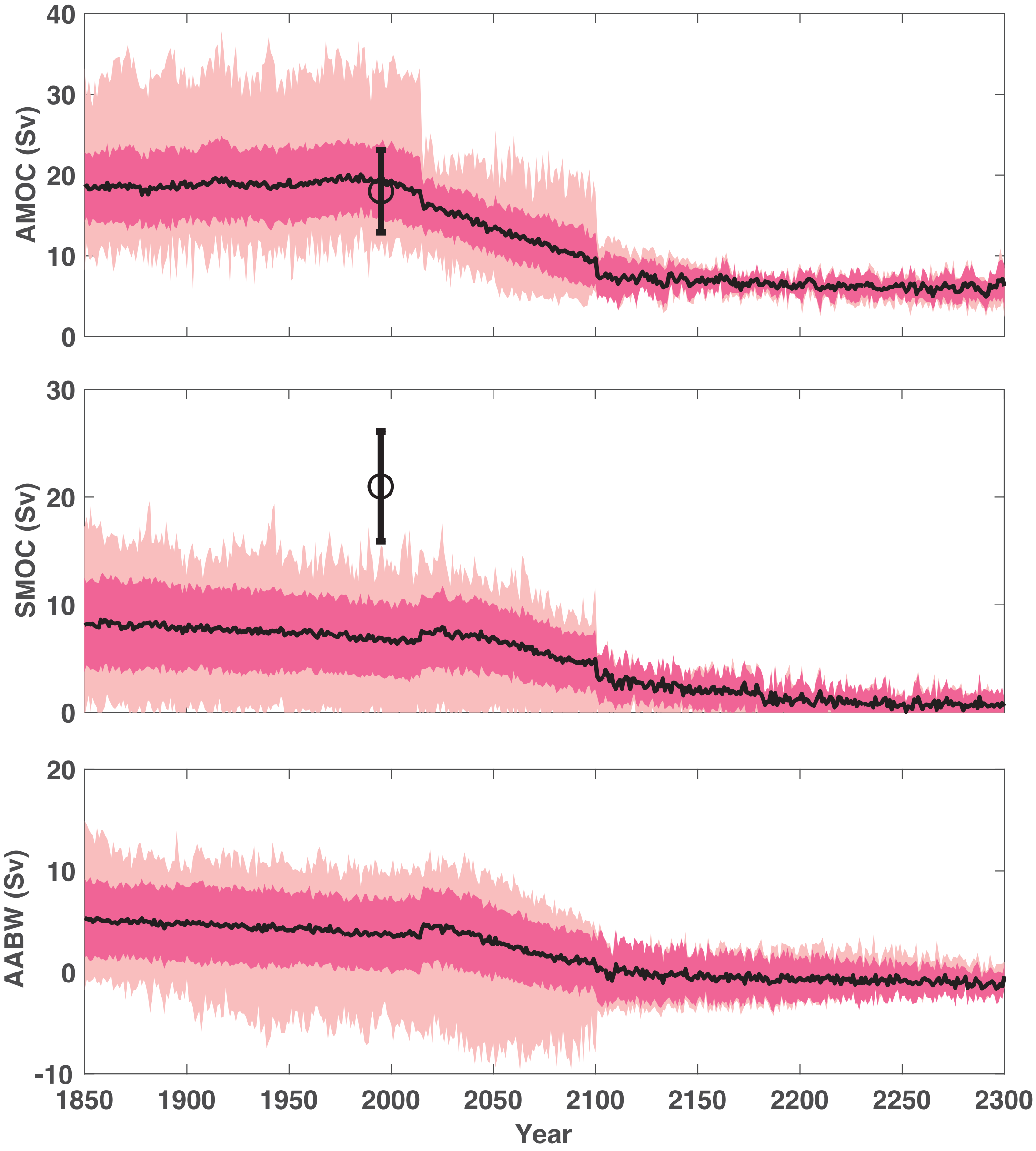

Figure 2.1. Slowing Meridional Overturning Circulation (MOC) with strong climate warming. Mean MOC rates (Sv) under the SSP5-8.5 scenario from CMIP6 models to year 2100 (36 models for historical period, 28 extend to 2100, 6 models extend to 2300, table S1) are shown for the Atlantic Meridional Overturning Circulation (AMOC, A) and the Southern Meridional Overturning Circulation (SMOC, B). Black line indicates the CMIP6 multi-model mean, and light and dark pink shadings indicate the range and one standard deviation. Black circles and lines indicate mean and one standard deviation of the observation-based MOC

estimates in table 2.4. Also shown is the mean northward bottom flow across 50°S (> 4000m), representing export of Antarctic Bottom Water (AABW) from the Southern Ocean (see SI for details).

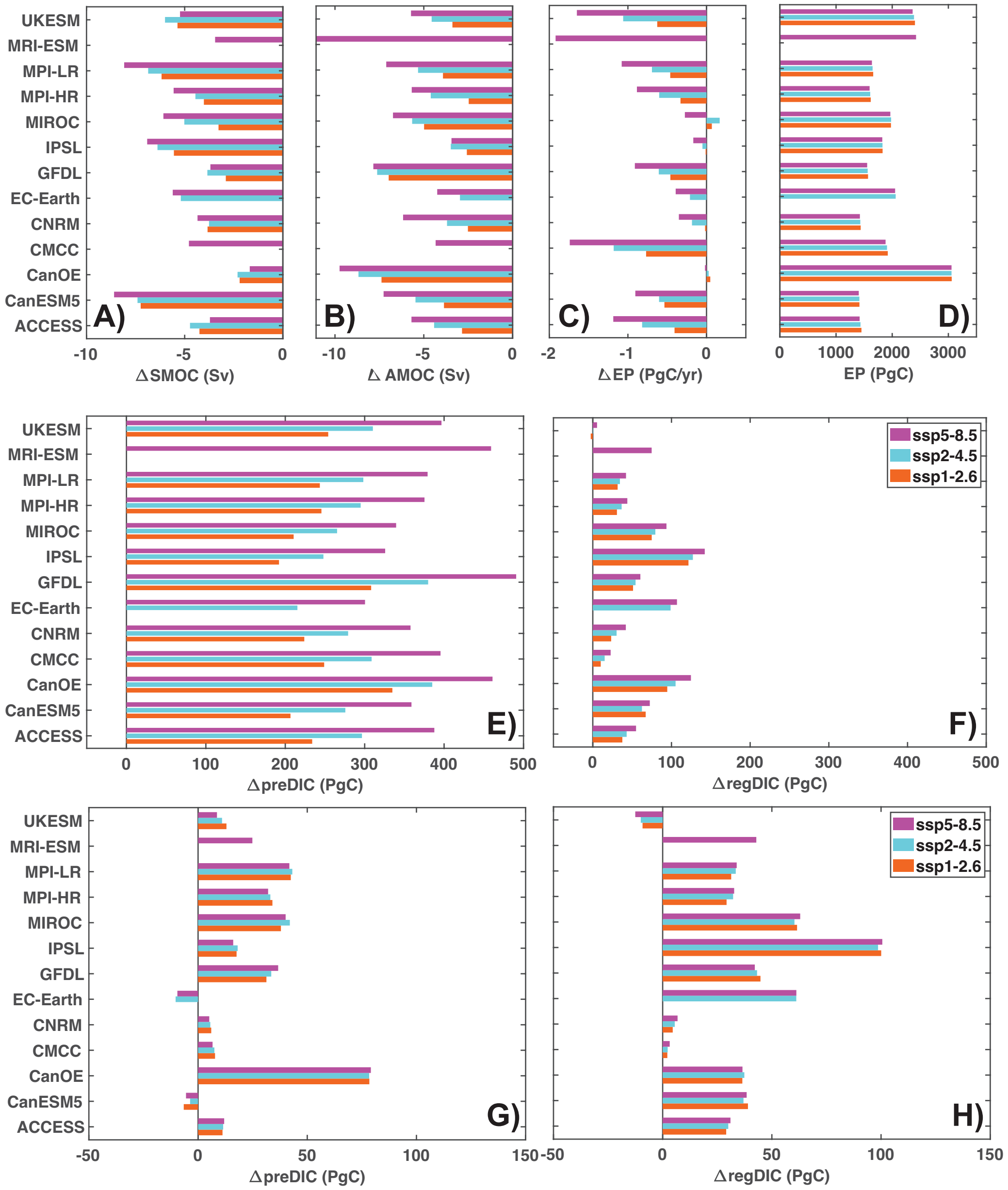

Figure 2.2. Changes in meridional overturning, carbon export, and carbon storage by 2100. Panels A and B show the changes in SMOC and AMOC (Sv) comparing preindustrial mean (1850-1869) to mean of years 2090-2099. Panel C shows changes in export production (sinking organic carbon at 100m (PgC/yr). Panel D shows the integrated export production from 1850 to 2100 (PgC). Panels E and F show preformed and regenerated carbon accumulation (PgC/yr) at intermediate depths (100-2000m) under three warming

scenarios. Panels G and H show deep ocean carbon accumulation (> 2000m) as in E and F. For reference 1 ppm atmospheric CO_2 = 0.47 PgC. Only 13 models with necessary variables are included.

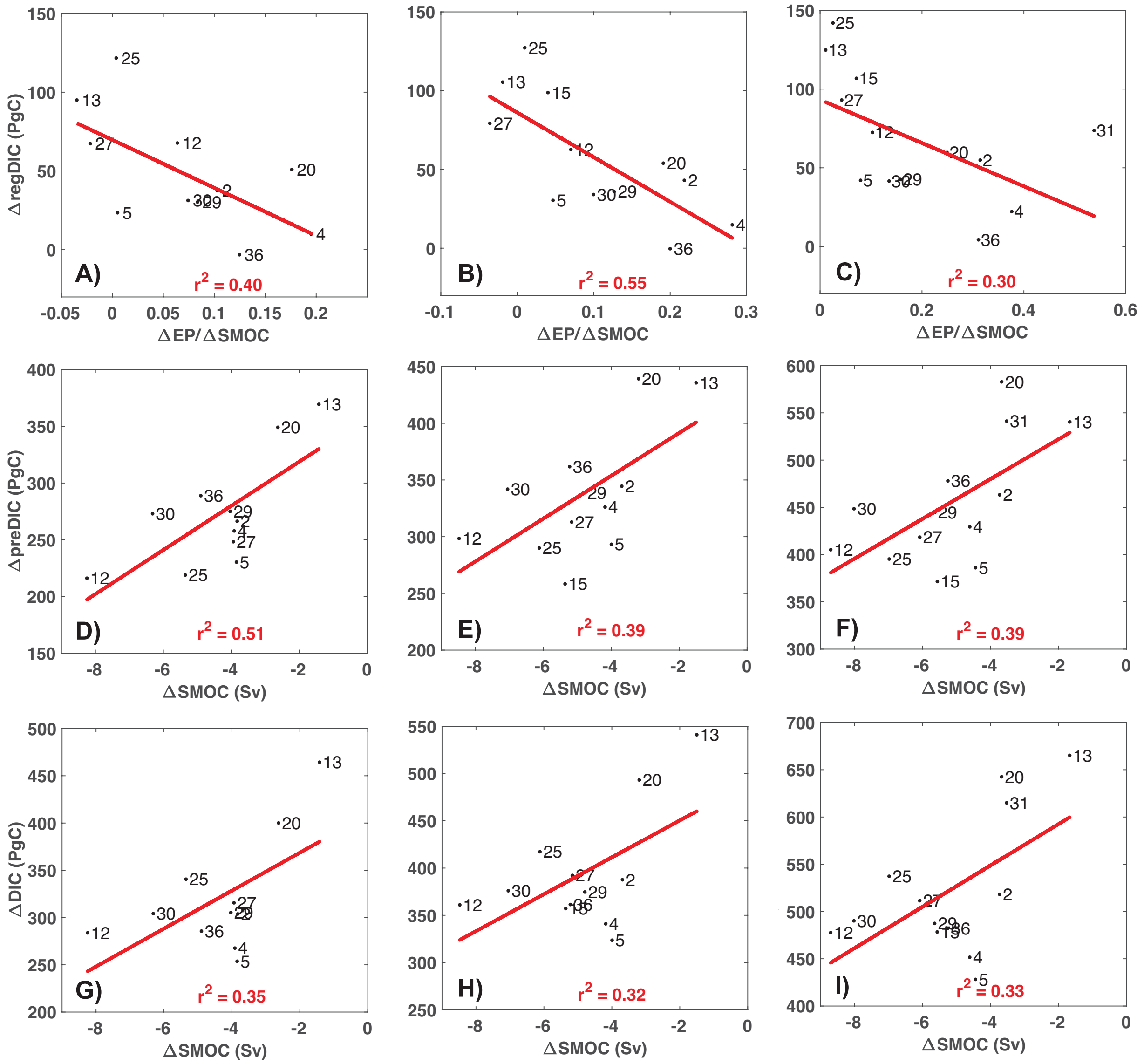

Figure 2.3. Slowing SMOC rates reduce ocean carbon uptake. The full water column storage of regenerated dissolved inorganic carbon (top row, A-C), preformed DIC (middle row, D-F), and total DIC (bottom row, G-I) by year 2100 (2080-2099 compared to 1850-1869) from eleven CMIP6 SSP1-2.6 projections (left column), twelve CMIP6 SSP2-4.5 projections (middle column), and thirteen CMIP6 SSP5-8.5 projections (right column) are compared with the relative declines of export production and SMOC rates (regenerated DIC) and declines in SMOC rate (preformed DIC and total DIC) by year 2100 (2080-2099 compared to 1850-1869). Plotted numbers indicate the model number in table S1.

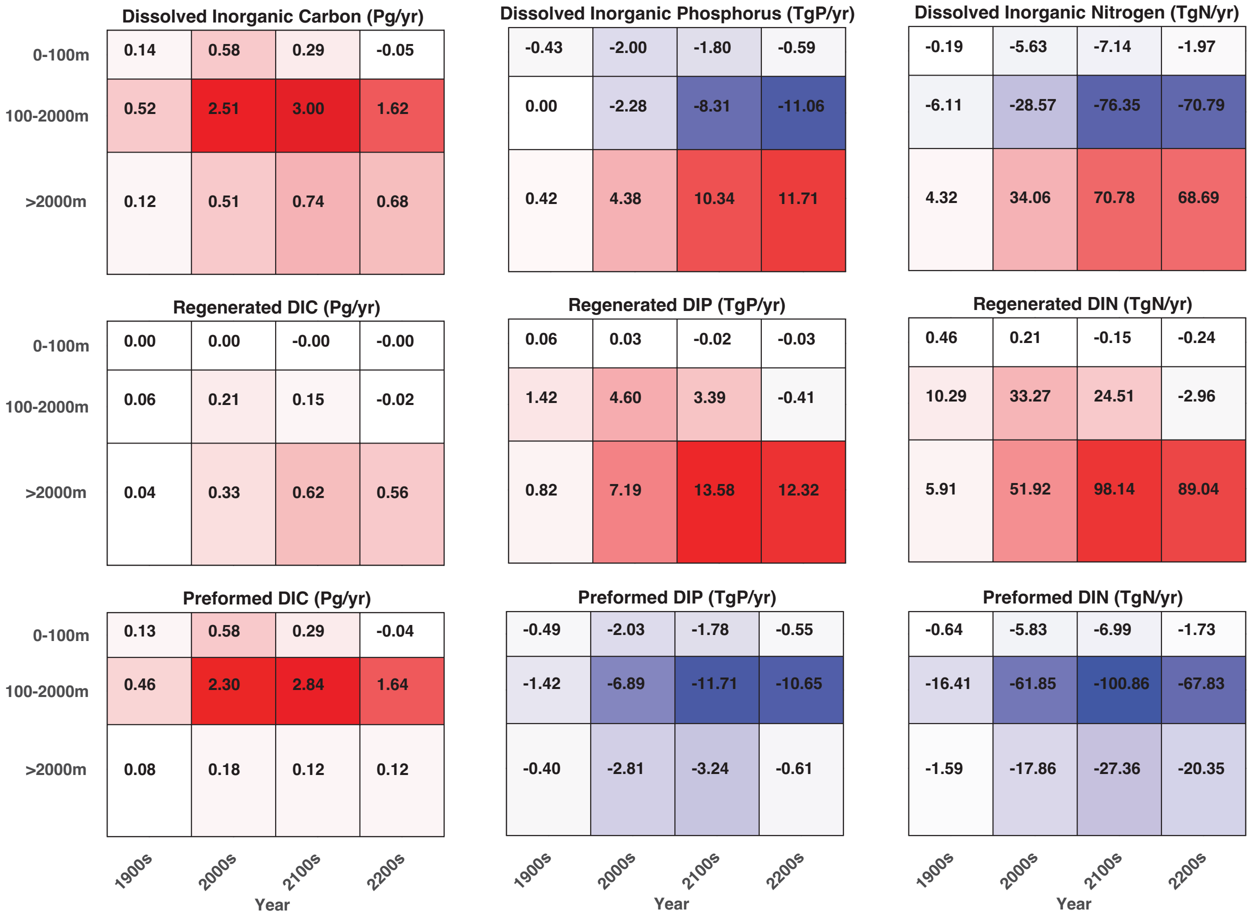

Dissolved Inorganic Carbon (Pg/yr)

	1900s	2000s	2100s	2200s
0-100m	0.14	0.58	0.29	-0.05
100-2000m	0.52	2.51	3.00	1.62
>2000m	0.12	0.51	0.74	0.68

Dissolved Inorganic Phosphorus (TgP/yr)

	1900s	2000s	2100s	2200s
0-100m	-0.43	-2.00	-1.80	-0.59
100-2000m	0.00	-2.28	-8.31	-11.06
>2000m	0.42	4.38	10.34	11.71

Dissolved Inorganic Nitrogen (TgN/yr)

	1900s	2000s	2100s	2200s
0-100m	-0.19	-5.63	-7.14	-1.97
100-2000m	-6.11	-28.57	-76.35	-70.79
>2000m	4.32	34.06	70.78	68.69

Regenerated DIC (Pg/yr)

	1900s	2000s	2100s	2200s
0-100m	0.00	0.00	-0.00	-0.00
100-2000m	0.06	0.21	0.15	-0.02
>2000m	0.04	0.33	0.62	0.56

Regenerated DIP (TgP/yr)

	1900s	2000s	2100s	2200s
0-100m	0.06	0.03	-0.02	-0.03
100-2000m	1.42	4.60	3.39	-0.41
>2000m	0.82	7.19	13.58	12.32

Regenerated DIN (TgN/yr)

	1900s	2000s	2100s	2200s
0-100m	0.46	0.21	-0.15	-0.24
100-2000m	10.29	33.27	24.51	-2.96
>2000m	5.91	51.92	98.14	89.04

Preformed DIC (Pg/yr)

	1900s	2000s	2100s	2200s
0-100m	0.13	0.58	0.29	-0.04
100-2000m	0.46	2.30	2.84	1.64
>2000m	0.08	0.18	0.12	0.12

Preformed DIP (TgP/yr)

	1900s	2000s	2100s	2200s
0-100m	-0.49	-2.03	-1.78	-0.55
100-2000m	-1.42	-6.89	-11.71	-10.65
>2000m	-0.40	-2.81	-3.24	-0.61

Preformed DIN (TgN/yr)

	1900s	2000s	2100s	2200s
0-100m	-0.64	-5.83	-6.99	-1.73
100-2000m	-16.41	-61.85	-100.86	-67.83
>2000m	-1.59	-17.86	-27.36	-20.35

Figure 2.4. Shifting carbon and nutrient distributions over time with climate warming. CESMv1-RCP8.5 centennial mean accumulation rates of dissolved inorganic carbon (left column, DIC (PgC/yr)), dissolved inorganic phosphorus (middle column, DIP (TgP/yr)) and dissolved inorganic nitrogen (right column DIN (TgN/yr)) in the surface ocean (0-100m), intermediate depths (100-2000m), and deep ocean (>2000m) averaged over the periods 1901-2000, 2001-2100, 2101-2200 and 2201-2300 under the RCP8.5-ECP8.5 scenario. The regenerated and preformed components sum to totals shown in top row. Red shading indicates positive accumulation rates and blue shading negative accumulation.

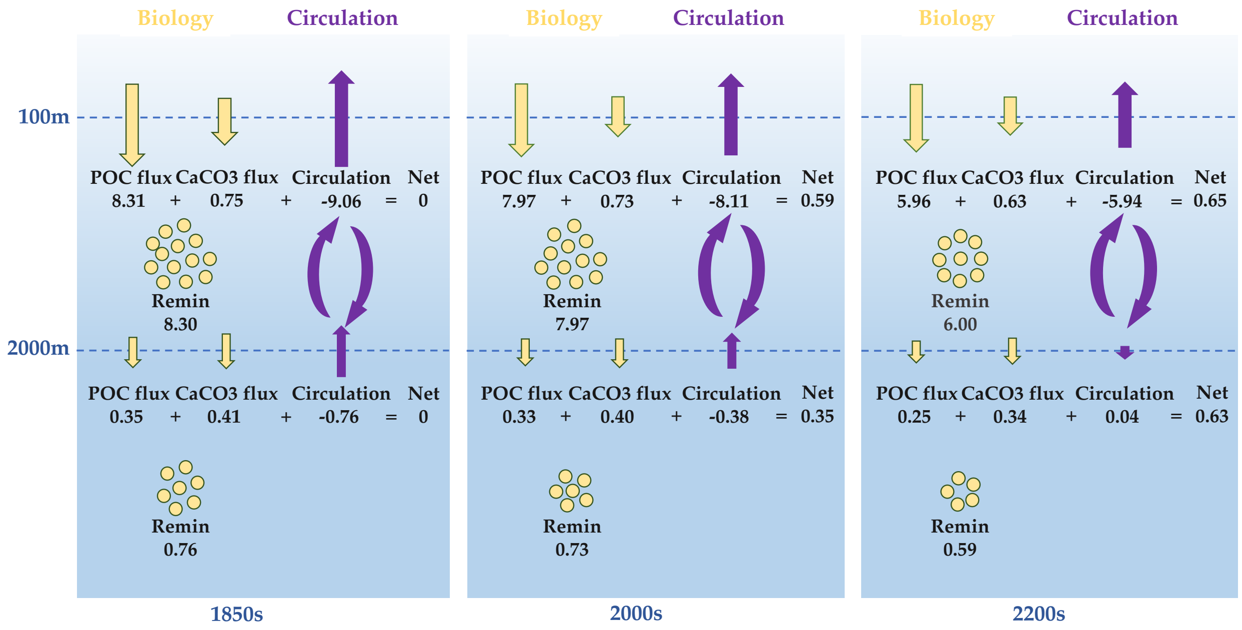

Figure 2.5. Biological export and changing circulation contributions to regenerated carbon storage. CESMv1-RCP8.5 carbon fluxes across the 100m and 2000m depth horizons due to biology as sinking particulate organic carbon (POC) and calcium carbonate ($CaCO_3$) (green arrows), and physical transport across these depths due to circulation and mixing (red arrows) under the RCP8.5-ECP8.5 scenario (PgC/yr). Left, middle, and right panels show mean carbon fluxes for the preindustrial (1850s) and the periods 2001-2100 and 2201-2300, respectively.

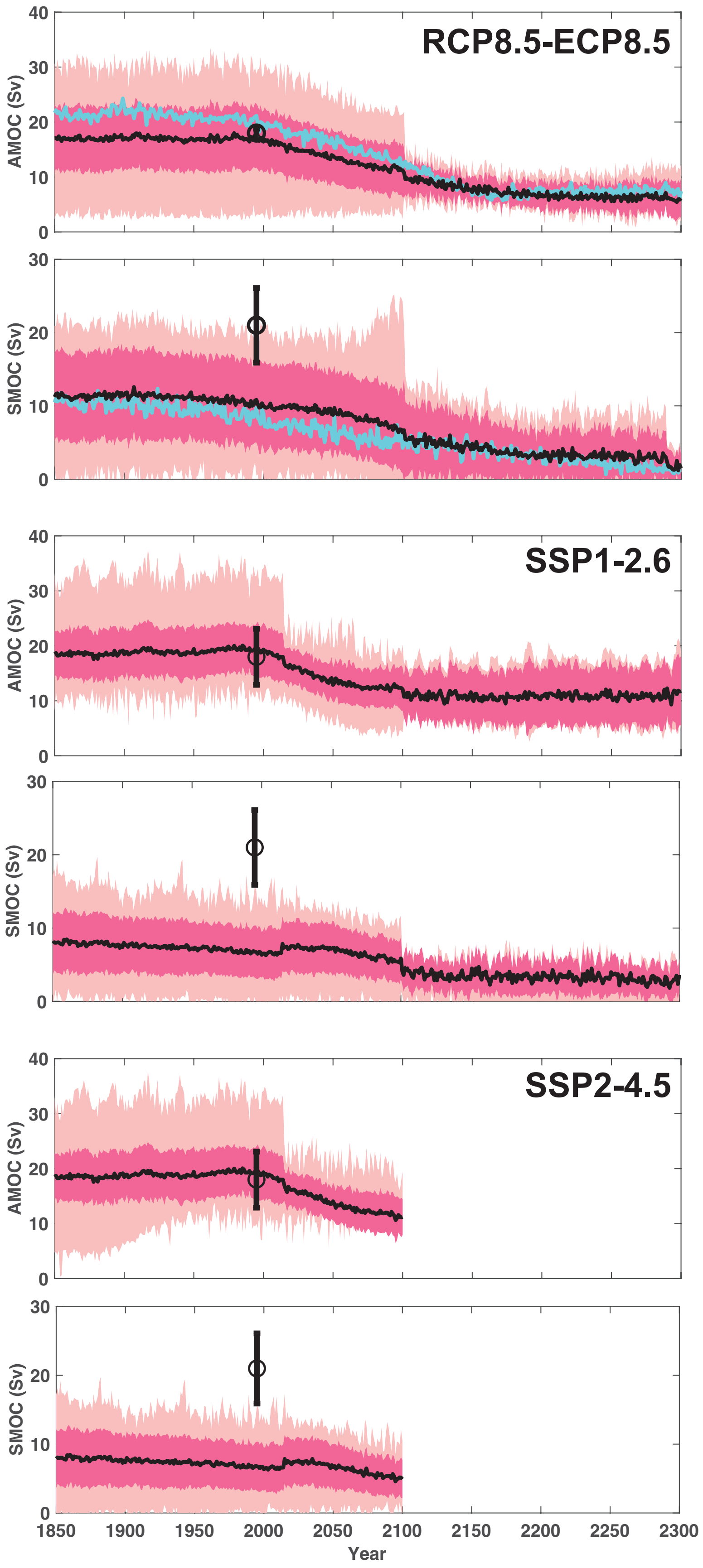
RCP8.5-ECP8.5
SSP1-2.6
SSP2-4.5
AMOC (Sv)
SMOC (Sv)
0
10
20
30
40
1850
1900
1950
2000
2050
2100
2150
2200
2250
2300
Year

Figure 2.6. Slowdown of Meridional Overturning Circulation (MOC) in CMIP5 (RCP8.5-ECP8.5) and CMIP6 (SSP1-2.6 and SSP2-4.5). The Atlantic Meridional Overturning Circulation (AMOC) and the Southern Meridional Overturning Circulation (SMOC) calculated from available CMIP5 models and CMIP6 models (Sv) are shown. The CESMv1 simulation is included and shown here as light blue line. Black lines show the multi-model mean, and light and dark pink shading indicate the range and one standard deviation of the overturning circulation. Black circles and error bars show mean and standard deviation of the observational estimates of MOC rates in table S1.

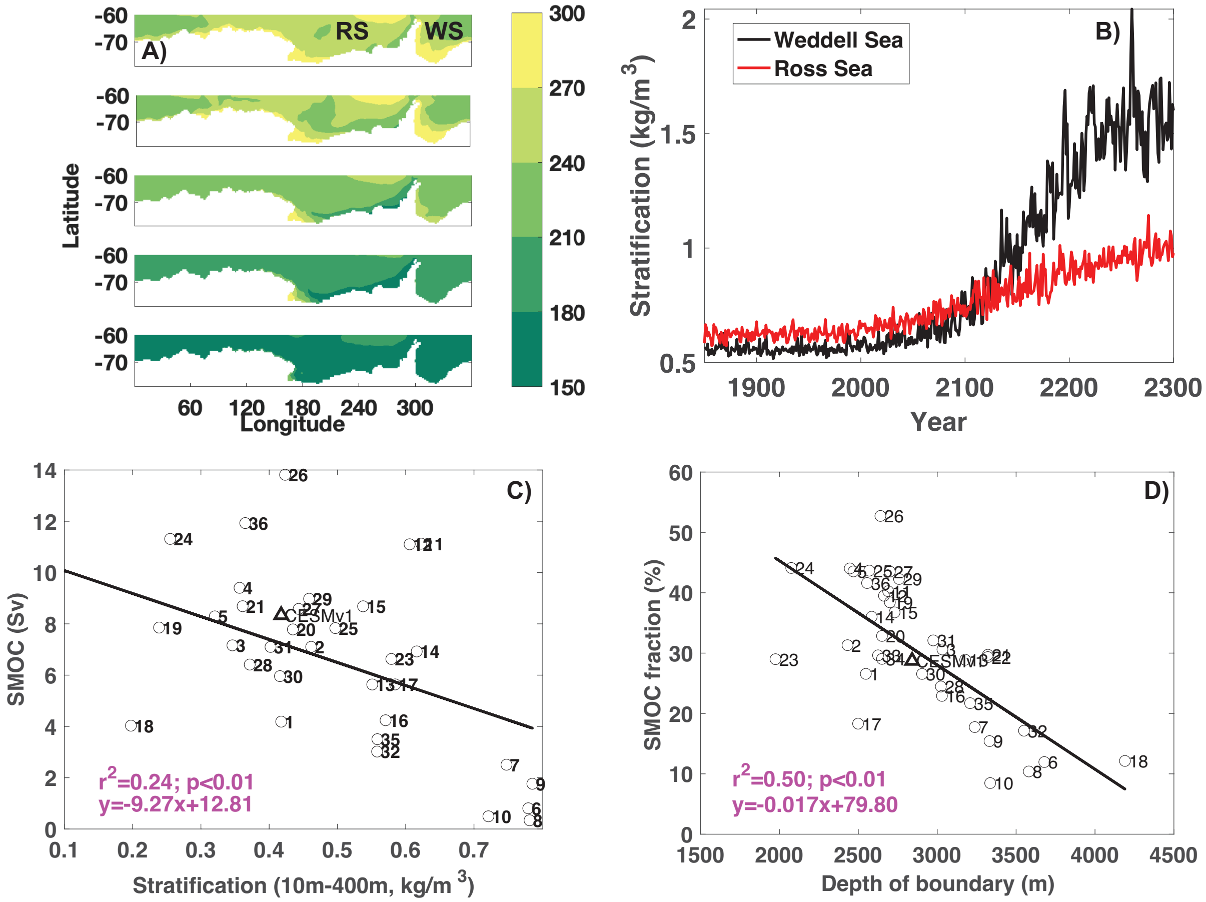

Figure 2.7. Declining Southern Ocean AABW Formation and SMOC. Dissolved oxygen distributions (mmol/m^3) at shelf depths (200-400m) are shown in panel A for decades (1850s, 1990s, 2090s, 2190s, and 2290s) with time series of mean stratification (kg/m^3, calculated by $\rho_{400m} - \rho_{0m}$) in the Weddell Sea (black line) and Ross Sea (red line, B). Panel C and D compare mean stratification (south of 60 °S) versus the SMOC rates (Sv), and mean depth boundary between the AMOC and the SMOC compared with the SMOC fraction of total global overturning circulation in the 1990s for the CMIP6 models. The number in C) and D) indicate the number of models in table S1. The “RS” and “WS” represent Ross Sea and Weddell Sea.

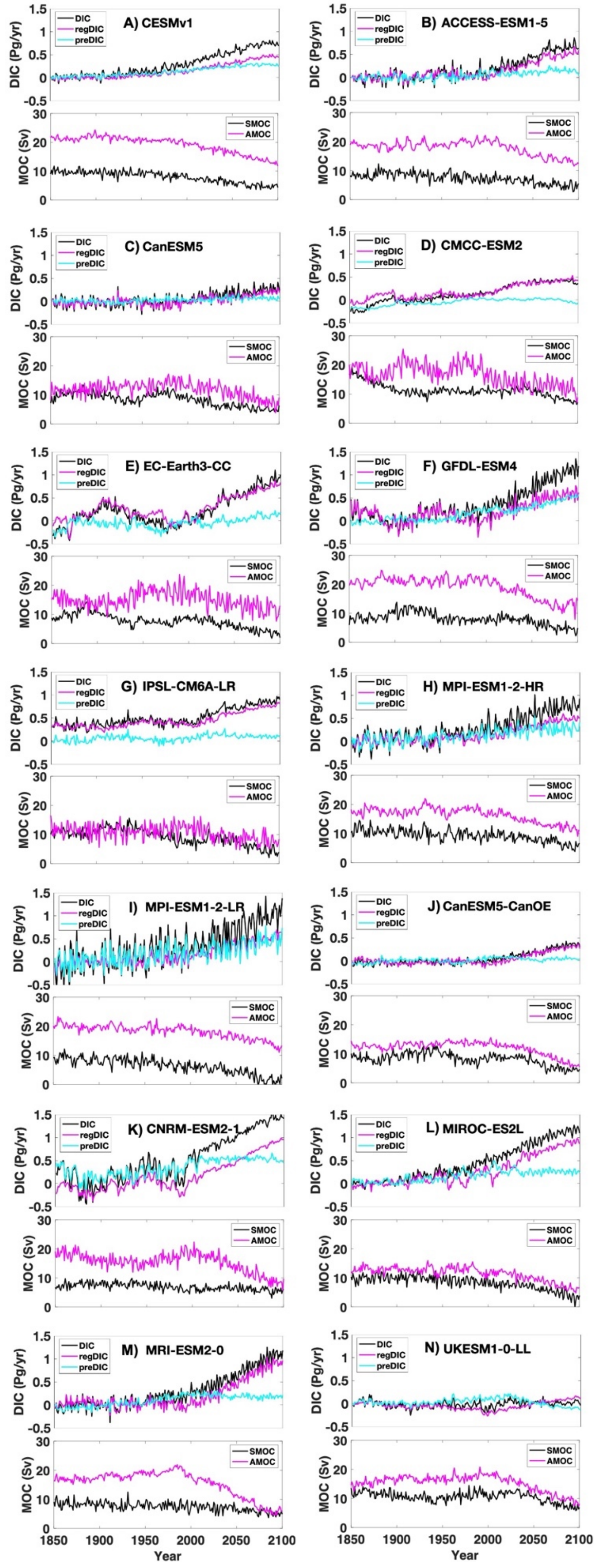
A) CESMv1
B) ACCESS-ESM1-5
C) CanESM5
D) CMCC-ESM2
E) EC-Earth3-CC
F) GFDL-ESM4
G) IPSL-CM6A-LR
H) MPI-ESM1-2-HR
I) MPI-ESM1-2-LR
J) CanESM5-CanOE
K) CNRM-ESM2-1
L) MIROC-ES2L
M) MRI-ESM2-0
N) UKESM1-0-LL
DIC
regDIC
preDIC
SMOC
AMOC
DIC (Pg/yr)
MOC (Sv)
1.5
1
0.5
0
-0.5
30
20
10
0
1850
1900
1950
2000
2050
2100
Year

Figure 2.8. Deep ocean carbon accumulation (> 2000m) in CESMv1 RCP8.5 and 13 CMIP6 models under the SSP5-8.5 warming scenario. The time series of DIC partitioning in CESMv1 (A), ACCESS-ESM1-5 (B), CanESM5 (C), CMCC-ESM2 (D), EC-Earth3-CC (E), GFDL-ESM4 (F), IPSL-CM6A-LR (G), MPI-ESM1-2-HR (H), MPI-ESM1-2-LR (I), CanESM5-CanOE (J), CNRM-ESM2-1 (K), MIROC-ES2L (L), MRI-ESM2-0 (M) and UKESM1-0-LL (N), where the black, red and blue line represents the total DIC, regenerated DIC and preformed DIC accumulation below 2000m depth (PgC/yr). Changing rates of the Southern-sourced Meridional Overturning Circulation (SMOC) and the Atlantic Meridional Overturning Circulation (AMOC) are also shown for each model.

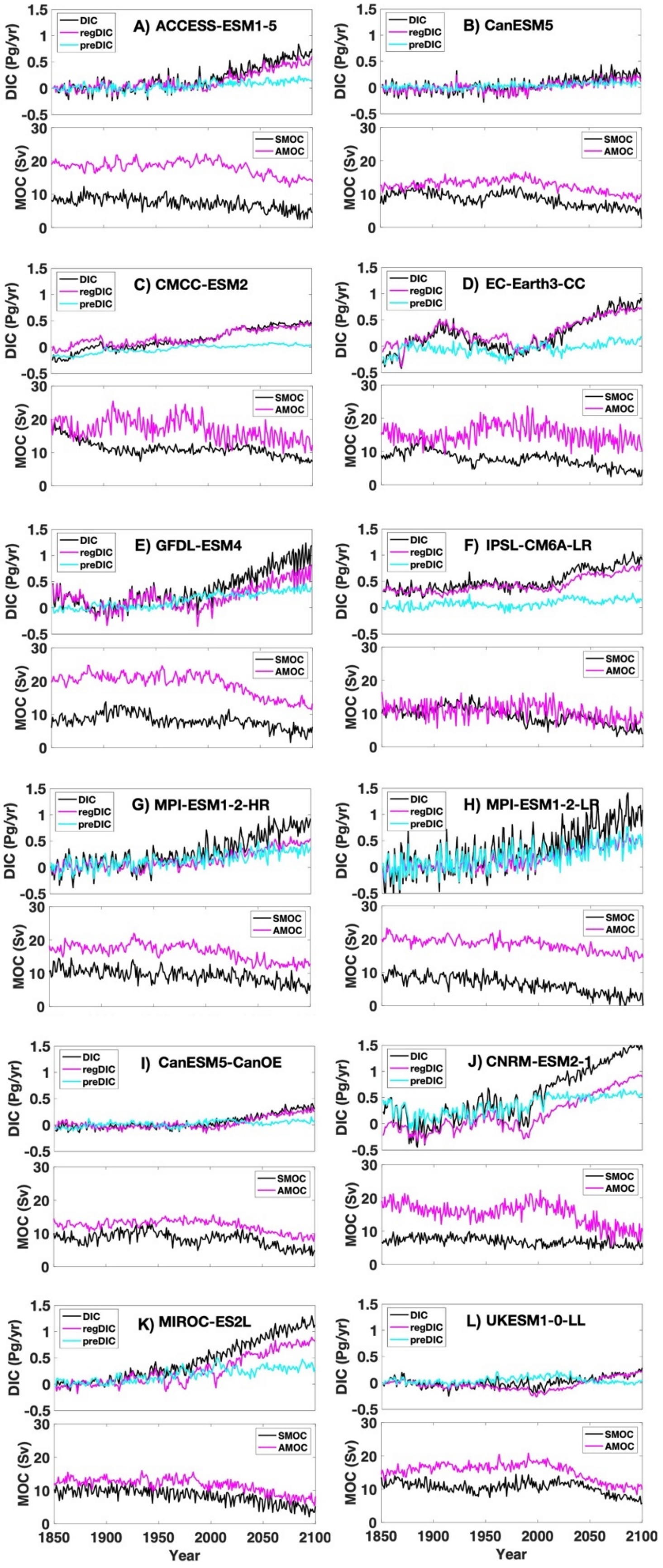
A) ACCESS-ESM1-5
B) CanESM5
C) CMCC-ESM2
D) EC-Earth3-CC
E) GFDL-ESM4
F) IPSL-CM6A-LR
G) MPI-ESM1-2-HR
H) MPI-ESM1-2-LR
I) CanESM5-CanOE
J) CNRM-ESM2-1
K) MIROC-ES2L
L) UKESM1-0-LL
DIC
regDIC
preDIC
SMOC
AMOC
DIC (Pg/yr)
MOC (Sv)
1.5
1
0.5
0
-0.5
30
20
10
0
1850
1900
1950
2000
2050
2100
Year

Figure 2.9. Deep ocean carbon accumulation and meridional overturning rates in twelve CMIP6 models under SSP2-4.5 scenario. The time series of DIC partitioning in ACCESS-ESM1-5 (A), CanESM5 (B), CMCC-ESM2 (C), EC-Earth3-CC (D), GFDL-ESM4 (E), IPSL-CM6A-LR (F), MPI-ESM1-2-HR (G), MPI-ESM1-2-LR (H), CanESM5-CanOE (I), CNRM-ESM2-1 (J), MIROC-ES2L (K) and UKESM1-0-LL(L), where the black, red and blue line represents the total DIC, regenerated DIC and preformed DIC accumulation below 2000m depth (PgC/yr). Changing rates of the Southern-sourced Meridional Overturning Circulation (SMOC) and the Atlantic Meridional Overturning Circulation (AMOC) are also shown for each model.

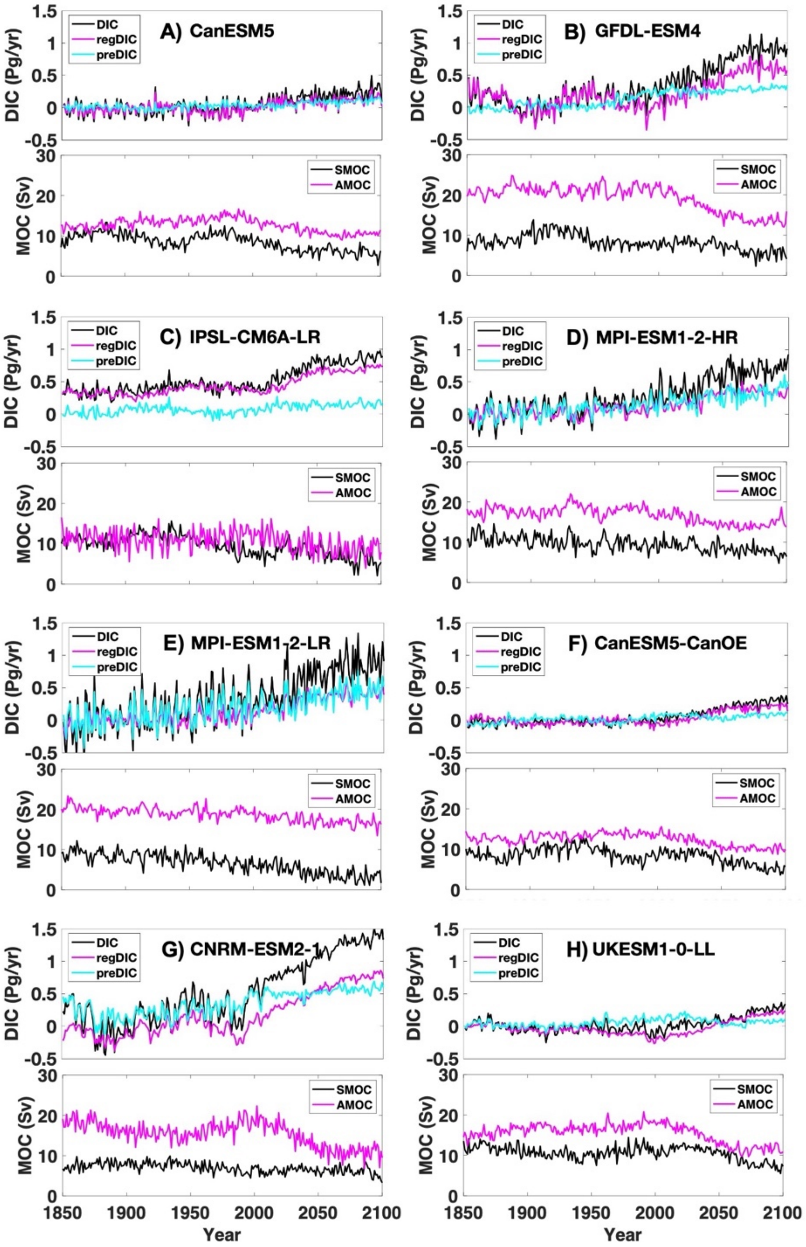

Figure 2.10. Deep ocean carbon accumulation and meridional overturning rates in eight CMIP6 models under the SSP1-2.6 warming scenario. The time series of DIC partitioning in CanESM5 (A), GFDL-ESM4 (B), IPSL-CM6A-LR (C), MPI-ESM1-2-HR (D), MPI-ESM1-2-LR (E), CanESM5-CanOE (F), CNRM-ESM2-1 (H) and UKESM1-0-LL (I), where the black, red and blue lines represent the total DIC, regenerated DIC and preformed DIC below 2000m depth (PgC/yr). Changing rates of the Southern-sourced Meridional Overturning Circulation (SMOC) and the Atlantic Meridional Overturning Circulation (AMOC) are also shown for each model.

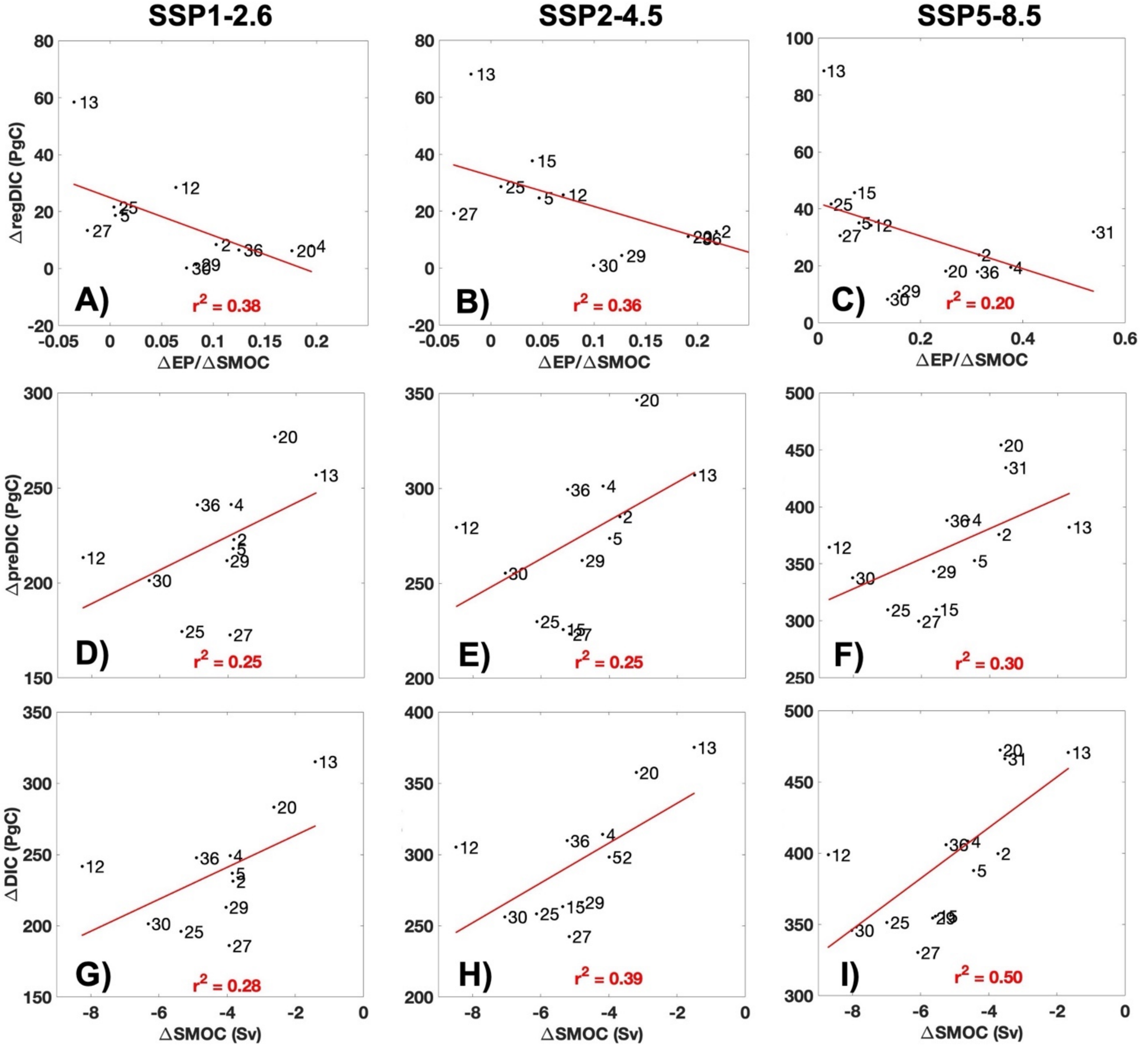

Figure 2.11. Slowing SMOC rates on intermediate ocean carbon uptake. The intermediate water (100-2000m) storage of regenerated dissolved inorganic carbon (DIC) (top row, A-C), preformed DIC (middle row, D-F), and total DIC (bottom row, G-I) by year 2100 (2080-2099 compared to 1850-1869) from eleven CMIP6 SSP1-2.6 projections (left column), twelve CMIP6 SSP2-4.5 projections (middle column), and thirteen CMIP6 SSP5-8.5

projections (right column) are compared with the relative declines of export production and SMOC rates (regenerated DIC) and declines in SMOC rate (preformed DIC and total DIC) by year 2100 (2080-2099 compared to 1850-1869). Plotted numbers indicate model number in table S1.

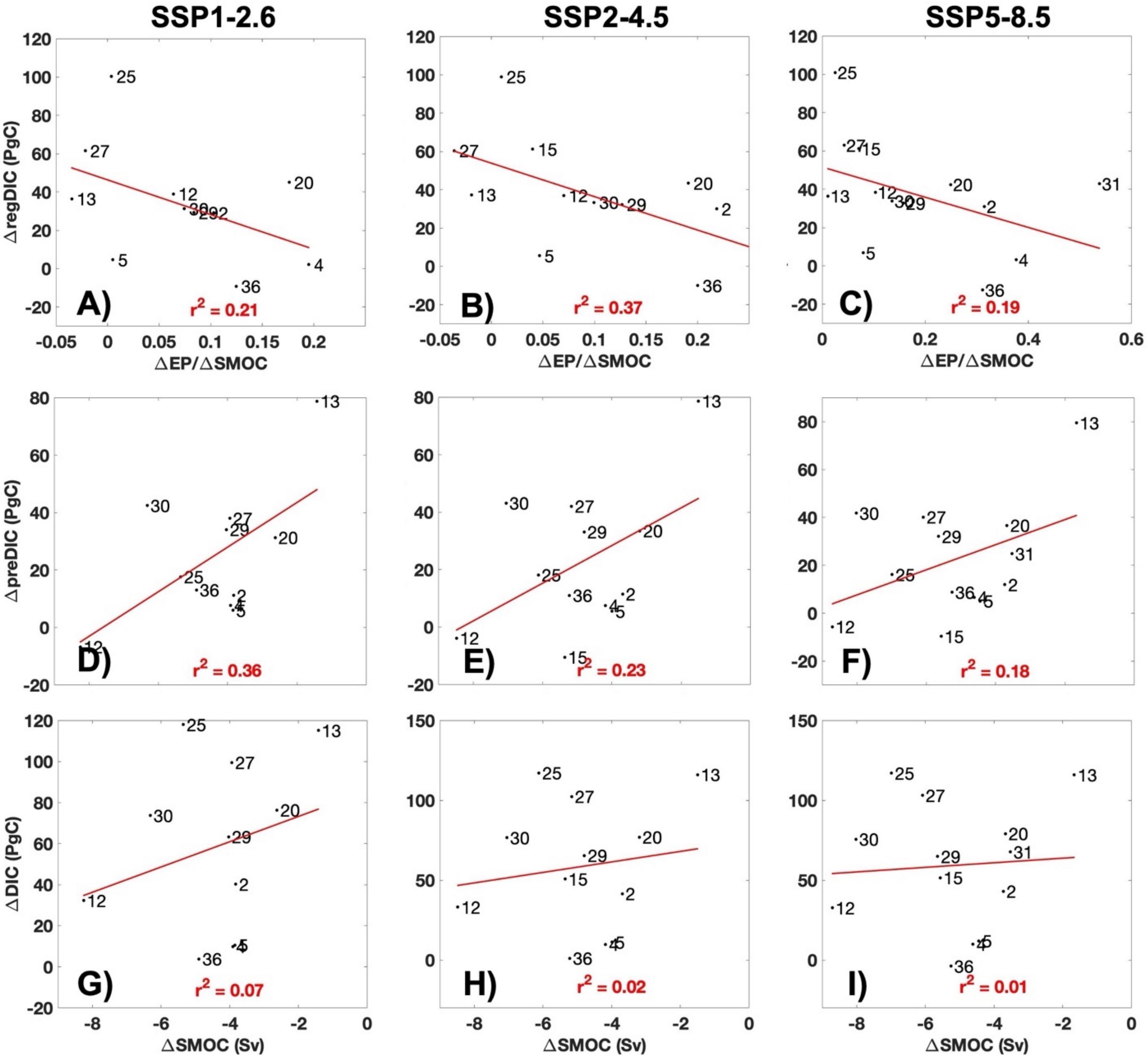

Figure 2.12. Slowing SMOC rates on deep ocean carbon uptake. The deep water (>2000m) storage of regenerated dissolved inorganic carbon (DIC) (top row, A-C), preformed DIC (middle row, D-F), and total DIC (bottom row, G-I) by year 2100 (2080-2099 compared to 1850-1869) from eleven CMIP6 SSP1-2.6 projections (left column), twelve CMIP6 SSP2-4.5 projections (middle column), and thirteen CMIP6 SSP5-8.5 projections (right column) are compared with the relative declines of export production and SMOC rates (regenerated DIC) and declines in SMOC rate (preformed DIC and total DIC) by year 2100 (2080-2099 compared to 1850-1869). Plotted numbers indicate model number in table S1.

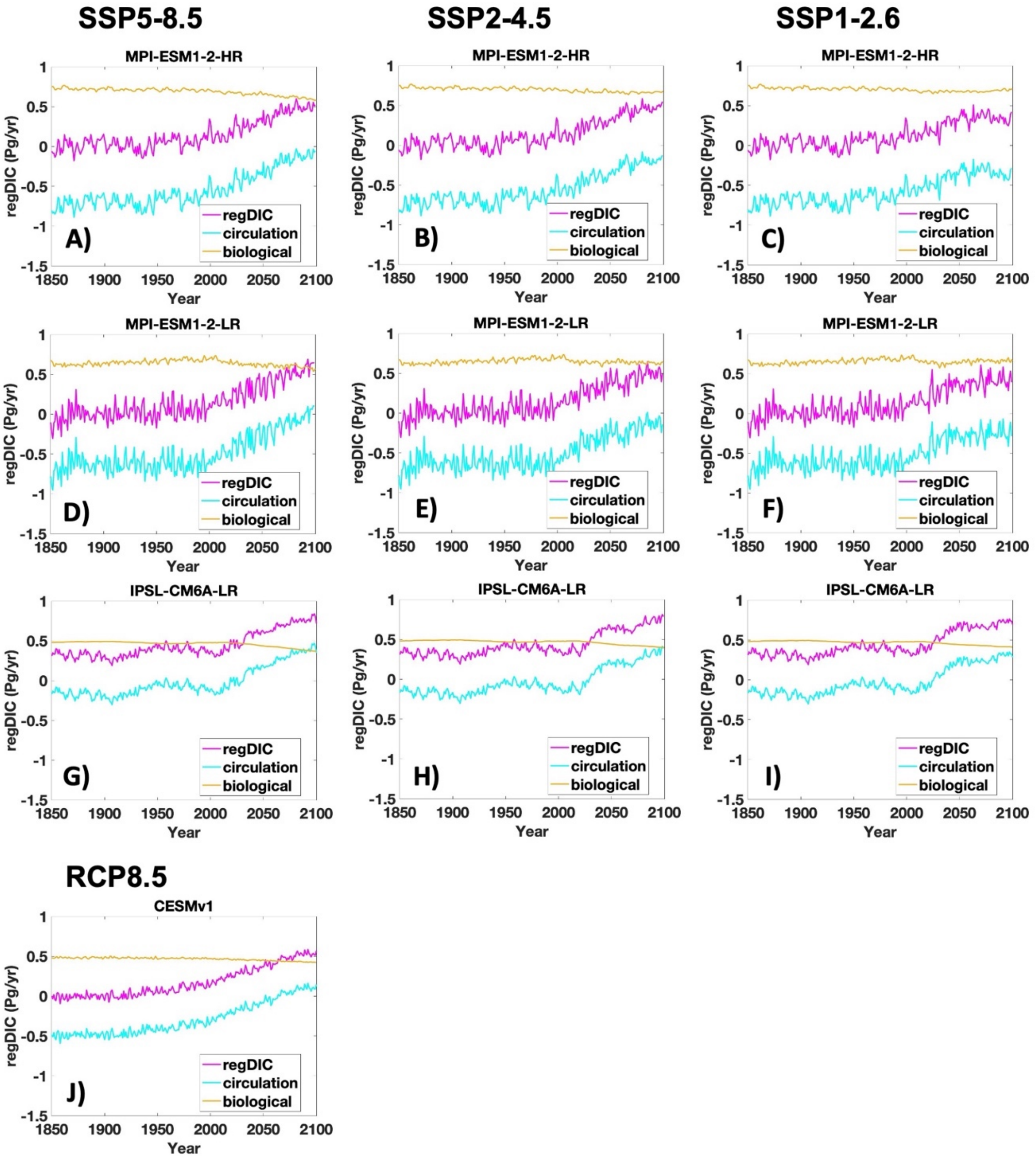

Figure 2.13. Separating biology and circulation impacts on regenerated DIC accumulation in the deep ocean. The contribution of varying circulation and sinking biological export to the deep ocean (> 2000m) regenerated DIC accumulation for CESMv1, two versions of the MPI-ESM1 model and IPSL-CM6A-LR model from the CMIP6 under three climate scenarios.

Table 2.2. The CMIP6 models included in the MOC analysis. The 36 CMIP6 models included in the meridional overturning circulation computation. Only models with all necessary outputs available and a net northward bottom flow out of the Southern Ocean

were included. Extended output to year 2300 was only available for a subset of the models. "Yes" indicates model output available and no indicates not available.

	Model name	Historical	SSP5-8.5		SSP2-4.5		SSP1-2.6	
			To 2100	To 2300	To 2100	To 2300	To 2100	To 2300
1	ACCESS-CM2	Yes	Yes	No	Yes	No	Yes	Yes
2	ACCESS-ESM1-5	Yes	Yes	No	Yes	No	Yes	Yes
3	BCC-CSM2-MR	Yes	Yes	No	Yes	No	Yes	No
4	CanESM5	Yes	Yes	Yes	Yes	No	Yes	Yes
5	CanESM5-CanOE	Yes	Yes	No	Yes	No	Yes	No
6	CESM2	Yes	Yes	No	Yes	No	Yes	No
7	CESM2-FV2	Yes	No	No	No	No	No	No
8	CESM2-WACCM	Yes	Yes	Yes	Yes	No	Yes	Yes
9	CESM2-WACCM-FV2	Yes	No	No	No	No	No	No
10	CIESM	Yes	Yes	No	Yes	No	Yes	No
11	CMCC-CM2-SR5	Yes	Yes	No	Yes	No	Yes	No
12	CMCC-ESM2	Yes	Yes	No	Yes	No	Yes	No
13	CNRM-ESM2-1	Yes	Yes	No	Yes	No	Yes	No
14	EC-Earth3	Yes	Yes	No	Yes	No	Yes	No
15	EC-Earth3-CC	Yes	Yes	No	Yes	No	No	No
16	EC-Earth3-Veg	Yes	Yes	No	Yes	No	Yes	No
17	FGOALS-f3-L	Yes	Yes	No	Yes	No	Yes	No
18	FGOALS-g3	Yes	Yes	No	Yes	No	Yes	No
19	GFDL-CM4	Yes	Yes	No	Yes	No	Yes	No
20	GFDL-ESM4	Yes	Yes	No	Yes	No	No	No
21	GISS-E2-1-G-CC	Yes	No	No	No	No	No	No
22	GISS-E2-1-G	Yes	No	No	No	No	No	No
23	INM-CM4-8	Yes	Yes	No	Yes	No	Yes	No
24	INM-CM5-0	Yes	Yes	No	Yes	No	Yes	No
25	IPSL-CM6A-LR	Yes	Yes	Yes	Yes	No	Yes	Yes
26	MIROC6	Yes	Yes	No	Yes	No	Yes	No
27	MIROC-ES2L	Yes	Yes	No	Yes	No	Yes	No
28	MPI-ESM1-2-HAM	Yes	No	No	No	No	No	No
29	MPI-ESM1-2-HR	Yes	Yes	No	Yes	No	Yes	No
30	MPI-ESM1-2-LR	Yes	Yes	No	Yes	No	Yes	No
31	MRI-ESM2-0	Yes	Yes	Yes	Yes	No	Yes	Yes
32	NorCPM1	Yes	No	No	No	No	No	No
33	NorESM2-LM	Yes	Yes	No	Yes	No	Yes	No
34	NorESM2-MM	Yes	Yes	No	No	No	No	No
35	SAM0-UNICON	Yes	No	No	No	No	No	No
36	UKESM1-0-LL	Yes	Yes	No	Yes	No	Yes	No

Table 2.3. The CMIP5 models included in the MOC analysis. The 24 CMIP5 models included in the meridional overturning circulation computation under RCP8.5 warming scenario. Only the models with necessary outputs available and some net northward bottom flow out of the Southern Ocean were included. Extended output to year 2300 was only available for a subset of the models.

	Model name	Historical	To 2100	To 2300
1	ACCESS1-0	Yes	Yes	No
2	ACCESS1-3	Yes	Yes	No
3	CanESM2	Yes	Yes	No
4	CNRM-CM5	Yes	Yes	Yes
5	CSIRO-Mk3-6-0	Yes	Yes	Yes
6	FGOALS-g2	Yes	Yes	No
7	GFDL-CM3	Yes	Yes	No
8	GFDL-ESM2G	Yes	Yes	No
9	GFDL-ESM2M	Yes	Yes	No
10	GISS-E2-R	Yes	Yes	Yes
11	GISS-E2-R-CC	Yes	Yes	No
12	HadGEM2-CC	Yes	Yes	No
13	HadGEM2-ES	Yes	Yes	Yes
14	INMCM4	Yes	Yes	No
15	IPSL-CM5A-MR	Yes	Yes	No
16	IPSL-CM5A-LR	Yes	Yes	Yes
17	IPSL-CM5B-LR	Yes	Yes	No
18	MIROC5	Yes	Yes	No
19	MPI-ESM-MR	Yes	Yes	No
20	MPI-ESM-LR	Yes	Yes	No
21	MRI-CGCM3	Yes	Yes	No
22	MRI-ESM1	Yes	Yes	No
23	NorESM1-ME	Yes	Yes	No
24	NorESM1-M	Yes	Yes	No

Table 2.4. Model mean 1990s overturning rates from CMIP6 (36 models) and CMIP5 (24 models) for the Atlantic Meridional Overturning Circulation (AMOC) and the Southern Meridional Overturning Circulation (SMOC) cells are compared with observation-based estimates (reproduced from Cessi, 2019). Maximum transport for AMOC is the maximum overturing at 30 °N over depths 0-3000 m. Maximum SMOC transport is the maximum overturning at 30°S over the depth range 2500-5000 m.

	Estimate	Sources*	Transport at 30°S (Sv)	Maximum transport (Sv)
AMOC	Models			
	CMIP5 Mean	1	12.0±4.7	17.1±5.8
	CMIP6 Mean	2	15.0±4.4	19.2±4.5
	Observation-based			
	Lumpkin & Speer, 2007	3	12	18
	Talley, 2013	3	13	18
	Meinen et al., 2018	4	15 (at 34.5°S)	NA
	McCarthy et al., 2015	5	NA	17.0
	ECCO4	6	15	19
	Mean		13.8±1.5	18.0±0.8
SMOC	Transport at 30°S (Sv)			
	Models			
	CMIP5 Mean	1	10.3±5.7	11.7±5.1
	CMIP6 Mean	2	6.7±3.4	8.4±3.5
	Observation-based			
	Talley, 2013	3	29	29
	Kunze, 2017	5	NA	20
	De Lavergne et al., 2016	5	NA	15
	Lumpkin & Speer, 2007	3	20.9	20.9
	ECCO4	6	15	20
	Mean		21.6±7.0	21.0±5.1

*: 1. CMIP5 model mean (24 models, Table S2); 2. CMIP6 model mean (36 models, Table S1); 3. Hydrography; 4. Moored density profiles; 5. Diapycnal mixing rates; 6. ECCO4, Estimating the Circulation and Climate of the Ocean v4 - assimilation of observations.

Methods

The CMIP5 and CMIP6 Ensembles

We analyze simulations from a set of 24 ESMs that were submitted to the Earth System Grid Federation as a part of CMIP5 and 36 ESMs that participated in CMIP6 to study the changing of overturning circulation and carbon sequestration under the business-as-usual scenarios in CMIP5 (RCP8.5-ECP8.5) and three warming scenarios from CMIP6 (SSP5-8.5+LTE, SSP2-4.5, SSP1-2.6) (tables 2.2-2.3). We use the meridional overturning circulation output variable "msftmz" and “msftyz” if available and integrate the meridional transport output "vmo" for the models not having "msftmz” or “msftyz”. Required physical ocean variables also included potential temperature and salinity to compute the density for assessing the ocean stratification. SMOC rate is defined as the maximum cell strength at 30^{o}S over depths of 2500-5000m. AMOC rate is defined as the maximum overturning between 0-3000m at 30^{o}N. The relative contributions of AMOC and SMOC is dependent on the boundary between the upper and abyssal cells of MOC, defined as the depth at the equator where the stream function is equal to zero. The AABW export from the Southern Ocean is defined as the net northward bottom flow across 50^{o}S in each model.

We also use CMIP6 models to study the carbon sequestration by dividing the dissolved inorganic carbon (variable "dissic") into regenerated and preformed fractions based on the apparent oxygen utilization (AOU):

$$regDIC = r_{C:O_2} \cdot AOU$$

$$preDIC = DIC - regDIC$$

where AOU = O_2sat – O_2 and O_2sat is the saturation dissolved oxygen concentration of a water parcel in contact with the atmosphere. The oxygen variables in CMIP6 models are "o2", and we computed the saturated O_2 (O_2sat) using the potential temperature and salinity to represent the effect of oxygen solubility changes. The regenerated dissolved inorganic phosphorus and nitrogen (DIP and DIN) are thus defined as:

$$regDIP = r_{P:C} \cdot regDIC$$

$$regDIN = r_{N:C} \cdot regDIC$$

where $r_{P:C} = 1/117$, $r_{N:C} = 16/117$, $r_{C:O2} = 117/138$ as fixed stoichiometric ratios (Moore et al., 2004). The preformed fraction of DIP and DIN are thus defined as:

$$preDIP = DIP - regDIP$$

$$preDIN = DIN - regDIN$$

where DIP and DIN are retrieved from CESMv1-RCP8.5 outputs directly. For the models with the remineralization variable "bddtdic" (MPI-ESM1-2-HR, MPI-ESM1-2-LR and IPSL-CM6A-LR), we separate the change in the deep ocean regenerated DIC sequestration into contributions from biological and physical processes. Relevant output from the CMIP5 and CMIP6 models are available from the Earth System Grid Federation (https://www.earthsystemgrid.org).

CMIP5 Community Earth System Model (CESMv1) RCP8.5-ECP8.5 Simulation

The CESMv1-RCP8.5 was used for CMIP5 and it simulates multiple plankton functional groups, key growth-limiting nutrients (nitrogen, phosphorus, iron, silicon), carbon, alkalinity, and oxygen (Moore et al., 2004). The circulation is simulated using CCSM4 ocean component (Danabasoglu et al., 2012; Gent et al., 2011). The model configuration details and spin up were previously reported (Lindsay et al., 2014) along with analysis of the historical uptake and storage of anthropogenic CO_2 in the oceans (Long et al., 2013). Evaluation of the marine ecosystem dynamics, biogeochemistry, and climate change impacts under RCP4.5 and RCP8.5 up to the year 2100 have been documented (Moore et al., 2013; Misumi et al., 2014), and were extended to 2300 along the RCP8.5-ECP8.5 scenario (Randerson et al., 2015; Moore et al., 2018). We build on these previous analyses of this simulation, and compare with the CMIP6 results. RCP8.5-ECP8.5 is a high-end, emissions-as-usual scenario with prescribed atmospheric CO_2 values reaching 1962 ppm before leveling off for the last 50 years of the simulation. It was part of the CMIP5 simulations. Additional CESM documentation and source code are available online (www2.cesm.ucar.edu), and the model output files from this simulation are available through the Earth System Grid Federation (ESGF) data delivery system at (https://www.earthsystemgrid.org/dataset/ucar.cgd.ccsm4.randerson2015.html).

In the RCP8.5-ECP8.5 simulation, global mean surface air temperature increases 9.6°C, warming more than 25°C in polar regions (Randerson et al., 2015). We previously documented large increases in net primary production (NPP) and export production (EP) in the high-latitude Southern Ocean driven by climate forcings (warming surface waters, declining sea ice cover, shifting winds), which stripped out a higher percentage of the nutrients upwelling at the Antarctic Divergence, reducing the northward flow of nutrients in the surface Ekman layer. The increased export production sinking into the upwelling waters drives a subsurface nutrient buildup (~100-1000m, "nutrient trapping") (Moore et al., 2018). Subsurface concentrations of nitrate, phosphate, and silicate in this trapping region increase substantially and are still rising at the end of the simulation in the year 2300. Upper-ocean nutrient concentrations declined everywhere outside the Southern Ocean, leading to steady declines in biological production and export to the ocean interior. By 2300 global-scale NPP decreases by 15%, and the global carbon export at 100m declines by 30% (Moore et al., 2018).

Development of the Offline Tracer Transport Model

It is difficult to separate the roles of the changing physical circulation from the changing biological processes using standard climate model output. We, therefore, constructed an offline tracer transport model from which we diagnose the separate effects of the changes in the circulation and the changes of the biogeochemical transformations. To this end, we retrieved the velocity field and diffusivity coefficients from the CESMv1-RCP8.5 output and constructed a time-dependent tracer transport operator,

$$\boldsymbol{T}(t) \equiv \nabla \cdot [\boldsymbol{u}(t) - \boldsymbol{K}(t) \cdot \nabla]$$

with a 1-year time resolution, i.e., $\boldsymbol{T}(t)$ consists of a series of sparse matrices, one per year, in which annual averages replace the continuous $\boldsymbol{u}(\boldsymbol{t})$ and $\boldsymbol{K}(\boldsymbol{t})$. No-flux conditions are built into the operator at all the solid basin boundaries and the sea surface. The parent ocean model in CESMv1 is POP2 (Gent et al., 2011).

On the discretized model mesh, tracer fields are represented by a column vector whose components represent the tracer concentrations at the mesh points. Multiplication of such a vector by $\boldsymbol{T}(t)$ yields the advective-diffusive flux divergence of the tracer. For example, if $c(t)$ represents a tracer concentration field with source-minus-sink given by $S(t)$, then the time-evolution of c is governed by the following system of ordinary differential equations

$$\frac{dc}{dt} + \boldsymbol{T}(t)c = S(t). \qquad (1)$$

To separate the contribution of changing circulation from changing export production on the carbon storage in the deep ocean, we perform offline simulations using modified versions of Eq. (1) as described below.

Partitioning Regenerated and Preformed DIC in CESMv1-RCP8.5 with the Offline Model

When studying the impacts of overturning circulation and climate change on ocean tracers, it is often helpful to partition the tracers into their regenerated and preformed components. *Regenerated* DIC consists of inorganic carbon that was remineralized from organic carbon or $CaCO_3$ in the ocean interior. When DIC comes into contact with the surface layer where it can participate in the air-sea exchange of CO_2 it is relabeled as *preformed* DIC. The contribution of dissolved organic carbon to the deep export is small, and it is neglected in this study. We achieve this relabeling using a short restoring timescale of one day. Thus, the governing equation for regenerated DIC is given by

$$\frac{\partial c_{reg}}{\partial t} = -\boldsymbol{T}(t)c_{reg} - \boldsymbol{L}c_{reg} + S(t), \qquad (2)$$

$$c_{reg}(1850) = c_{reg,0}, \qquad (3)$$

where $\boldsymbol{L}$ is a diagonal matrix operator with non-zero elements for diagonal entries corresponding to surface grid boxes. For those entries, the elements are given by the reciprocal of the surface restoring timescale. The source of regenerated carbon is given by

$$S(t) = r_{C:O_2} \cdot OUR(t) + D_{\mathrm{CaCO_3}}(t), \qquad (4)$$

where the oxygen utilization rate, $OUR(t)$, and the calcium carbonate dissolution rate, $D_{\mathrm{CaCO_3}}(t)$, consist of annually-averaged values extracted from the CESMv1-RCP8.5 model output.

The initial condition, specified in 1850, is obtained by assuming that the system was in a steady-state equilibrium for $t < 1850$ and then solving the resulting linear system

$$[\,\boldsymbol{T}(\mathbf{1850}) + \boldsymbol{L}\,]c_{reg,0} = S(1850). \qquad (5)$$

The governing equation for the preformed DIC is given by

$$\frac{\partial c_{pre}}{\partial t} = -\boldsymbol{T}(t)c_{pre} - \boldsymbol{L}(c_{pre} - \mathrm{DIC(t)}), \qquad (6)$$

$$c_{pre}(1850) = c_{pre,0}, \qquad (7)$$

where DIC(t) is the total dissolved inorganic carbon extracted from the CESMv1-RCP8.5 output. The fast surface restoring term ensures that c_{pre} = DIC(t) in the top layer of the model. Below the surface $c_{pre}(t) < \mathrm{DIC}(t)$ because of the absence of the regenerated carbon source in the c_{pre} governing equation. The initial condition, again specified in 1850, is obtained by assuming a pre-1850 steady state and solving the resulting linear system

$$[\,\boldsymbol{T}(\mathbf{1850}) + \boldsymbol{L}\,]c_{pre,0} = \boldsymbol{L}\,\mathrm{DIC}(1850). \qquad (8)$$

Note that because the tracer transport equation is linear, the regenerated carbon can be further decomposed into three parts

$$c_{reg}(t) = c_{reg,0} + \Delta c_{reg,1} + \Delta c_{reg,2}, \quad (9)$$

where

$$\frac{\partial \Delta c_{reg,1}}{\partial t} = -\boldsymbol{T}(t)\Delta c_{reg,1} - \boldsymbol{L}\Delta c_{reg,1} + S(1850), \qquad (10)$$

$$\Delta c_{reg,1}(1850) = 0, \quad (11)$$

corresponds to the time evolution of the regenerated carbon that was remineralized before 1850, and

$$\frac{\partial \Delta c_{reg,2}}{\partial t} = -\boldsymbol{T}(t)\Delta c_{reg,2} - \boldsymbol{L}\Delta c_{reg,2} + \big(S(t) - S(1850)\big), \qquad (12)$$

$$\approx -\boldsymbol{T}(1850)\Delta c_{reg,2} - \boldsymbol{L}\Delta c_{reg,2} + \big(S(t) - S(1850)\big), \qquad (13)$$

$$\Delta c_{reg,2}(1850) = 0, \quad (14)$$

corresponds to the time evolution of the carbon anomaly due to the change in the carbon regeneration rate after 1850. As shown by direct computation (Fig. 2.2.14) the approximation in going from (12) to (13) where we replace the time-dependent transport operator with its 1850 value is a very good one. The negligible effect of the interaction between the time-dependence of the transport operator and the time-dependence of the biological source allows us to interpret $\Delta c_{reg,1}(t)$ and $\Delta c_{reg,2}(t)$ as a separation of the change in the regenerated carbon inventory into contributions due to the change in the physical circulation and the change in the biological production.

Potential Bias of the Offline Model and the traditional AOU method

We first compare CESMv1-RCP8.5 regenerated DIC accumulation computed from the offline model (equation (2)-(3)) and with the inorganic carbon regeneration computed using the AOU method (Fig. 2.14). The patterns are very similar but, approximately 10-20% more regenerated DIC is sequestered in the deep ocean in the offline model estimate. The main reason for this difference is due to the neglect of carbon regeneration associated with the dissolution of $CaCO_3$ in the AOU calculation.

There are multiple possible errors in the offline model compared with the parent POP2 ocean model. Before doing the offline tracer calculations, we coarse grained the tracer transport operator using the method from the POP2 nominal 1^ox1^o horizontal resolution to a roughly 2^ox2^o horizontal resolution (Gent et al., 2011). We also coarse grained the time variable from a 3 hour time-step size in POP2 to an annual time-step size for the offline model. Furthermore, the parent POP2 model in the CESMv1-RCP8.5 simulation has not reached complete equilibrium in 1850 causing a slight drift in the deep ocean that is not associated with imposed greenhouse forcing. In contrast, our offline calculations are based on an exact preindustrial ($t < 1850$) steady state.

The traditional AOU method has been widely used to calculate the regenerated fraction of DIC in the ocean by assuming that surface oxygen concentration is saturated, which introduces some error to the estimation. We explicitly simulate preformed O_2 to compute the True Oxygen Utilization (TOU) in the offline model to evaluate the uncertainties caused by the AOU method (Ito et al., 2004). The accumulation rate of regenerated DIC computed from the AOU method compares well with the TOU method in the whole water column (~5% uncertainties), even though the AOU methods underestimated the deep ocean regenerated DIC by 0.03 PgC-0.13 PgC and overestimated the intermediate ocean regenerated DIC by 0.01 PgC-0.12 PgC depending on the century (Fig. 2.15).

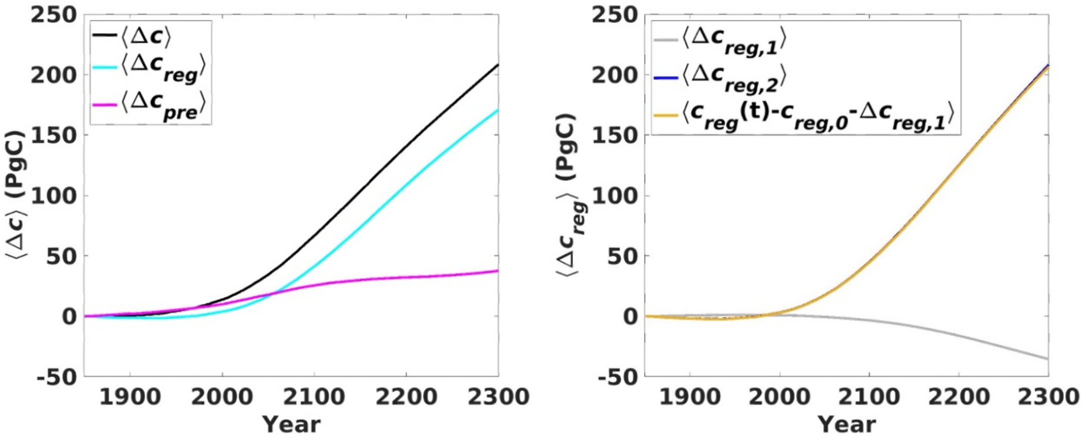

Figure 2.14. Partitioning of deep-ocean DIC storage in the offline model. Left panel shows changes in the deep-ocean carbon inventory, $\langle \Delta c \rangle$, partitioned into preformed $\langle \Delta c_{pre} \rangle$ and regenerated $\langle \Delta c_{reg} \rangle$ parts. The right panel shows the changes in the deep-ocean (depth > 2000 m) regenerated carbon inventory separated into the part remineralized before 1850 (gray line), a part that is due to change in the post-1850 regeneration rate computed by fixing the transport operator to its 1850 value (dark yellow). The blue line is nearly identical to dark yellow line, indicating that equation (13) is a good approximation of equation (12), see Methods. The angle brackets denote the volume integral over depths greater than 2000 m.

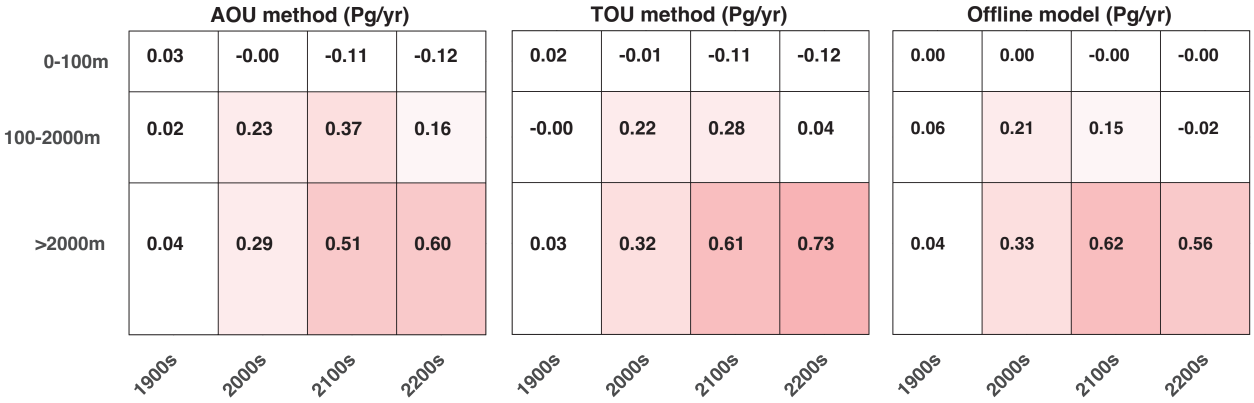

AOU method (Pg/yr)

	1900s	2000s	2100s	2200s
0-100m	0.03	-0.00	-0.11	-0.12
100-2000m	0.02	0.23	0.37	0.16
>2000m	0.04	0.29	0.51	0.60

TOU method (Pg/yr)

	1900s	2000s	2100s	2200s
0-100m	0.02	-0.01	-0.11	-0.12
100-2000m	-0.00	0.22	0.28	0.04
>2000m	0.03	0.32	0.61	0.73

Offline model (Pg/yr)

	1900s	2000s	2100s	2200s
0-100m	0.00	0.00	-0.00	-0.00
100-2000m	0.06	0.21	0.15	-0.02
>2000m	0.04	0.33	0.62	0.56

Figure 2.15. Comparison of the regenerated DIC accumulation calculated by the AOU method, TOU method and the offline model. The regenerated DIC accumulation rates in the surface ocean (0-100m), intermediate depths (100-2000m), and deep ocean (>2000m) averaged over the periods 1990-2000, 2000-2100, 2100-2200, and 2200-2300 computed from the AOU method in CESMv1 (left panel), TOU method (middle panel) and with the offline model (right panel) (PgC/yr).

Supplementary Information

Meridional Overturning Circulation in the CMIP5 and CMIP6 Models

There are substantial differences in the simulated global overturning circulation across the CMIP5 and CMIP6 models. The CMIP5 models have a larger spread (24 models) in the MOC rates compared to the CMIP6 models (Fig. 2.1, Fig. 2.6, tables 2.1, 2.2). AMOC ranges widely from less than 5 Sv to 35 Sv from the preindustrial to the 2100s under the RCP8.5-ECP8.5 warming scenario, though almost all the models showed a decreasing trend as expected (Fig. 2.6). Compared with the observational estimates, the strength of overturning circulation did not show noticeable improvement from CMIP5 to CMIP6. Both CMIP5 and CMIP6 models estimate the AMOC well at ~18Sv, consistent with observational estimates (table 2.2). However, both the CMIP5 and CMIP6 models strongly underestimate the strength of the SMOC (table 2.2). There are five models in CMIP5 extending to 2300, and all show continuing declines in the SMOC and the AMOC after year 2100 (Fig. 2.6). CMIP6 model mean SMOC continues to decline to ~2 Sv by the year 2300. The model mean CMIP6 AMOC also has a large reduction before stabilizing at about 5 Sv (Fig. 2.1). Under moderate warming scenarios (SSP1-2.6 and SSP2-4.5), both AMOC and SMOC weaken from the preindustrial to 2100, but they decline more slowly than under SSP5-8.5 (Fig. 2.1, Fig. 2.6).

Shutdown of AABW Formation and the SMOC in CESMv1

AABW formation slows due to increasing stratification in the Weddell Sea and the Ross Sea, key formation regions for AABW formation, which leads to the slowdown of the SMOC. The slowdown and apparent shutoff of dense AABW formation is noticeable in the oxygen fields averaged over the shelf depths (200-400m, Fig. 2.7A). Early in the simulation, high oxygen concentrations are seen in the southern Weddell and Ross seas, indicating waters recently in contact with the atmosphere. Over time the increasing stratification breaks the connection to surface waters, and oxygen concentrations then approach the much lower values seen offshore, first in the Weddell Sea by the 2090s and with only a small patch of high O_2 water in the Ross Sea by the 2190s (Fig. 2.7A). By the 2290s oxygen concentrations decline dramatically across the Southern Ocean at these depths as increasing temperatures, decrease density at the surface, and increasing stratification that ensures that winter mixing does not reach 200m depth in the region. The low oxygen concentrations demonstrate this lack of ventilation (Fig. 2.7A).

Stratification in the Weddell Sea (< 60 ^{o}S) increases rapidly beginning just before the year 2100 and levels out near the end of the simulation after rising by more than a factor of 2 (Fig. 2.7B). The increase is more gradual in the Ross Sea and begins earlier, though the increase in both regions it accelerates with increasing loss of the southern sea ice cover (Moore et al., 2018). The increasing stratification in both regions is primarily driven by reductions in surface salinity. The southern Weddell and Ross seas do not warm as much with climate change (1-2°C) as the offshore waters of the Southern Ocean (~6-9 °C) by 2300. These regions are kept cooler by the cold winds blowing off Antarctica and are the only place in the Southern Ocean where some sea ice still forms by 2300 (Moore et al., 2018). The salinity-driven vertical density gradients in the high latitude Southern Ocean and a strongly salinity-dominated Arctic Ocean stratification suggest that polar ocean physics, circulation, and biogeochemistry will be sensitive to increasing freshwater runoff from the Greenland and Antarctic ice sheets with climate warming.

Factors Influencing the strength and volume of SMOC in the CMIP6 models

The strength of SMOC is defined as the maximum northward transport between 2500 and 5000m at the latitude 30°S, across the CMIP6 models that SMOC ranges widely, from 2 Sv to 15 Sv in the present climate. One important reason is that the surface buoyancy forcing is not well constrained, making it challenging to assess the fidelity of the AABW formation rate. Fig. 2.7C shows the negative correlation between upper ocean stratification (density difference between 400m and 10m) in the latitudes 75°S-65°S and the strength of SMOC. The models with strong upper ocean stratification most underestimated SMOC, including CESMv2 and CIESM (models 5 and 9). The relative fraction of SMOC and AMOC to the global MOC is significant for circulation and ocean carbon storage patterns. The depth of the boundary between the MOC cells ranges widely in the CMIP6 models (Fig. 2.7D). In the models with a deep separation boundary, the upper cell extends deeper, which squeezes the abyssal cell into a small depth band and decreases its northward transport.

Ocean Carbon Storage in the CMIP6 Models

We compared carbon sequestration in the CMIP6 models that reported the variables needed to compute the sequestration and in the CESMv1 out to year 2100. We use the AOU method to separate regenerated DIC from the preformed DIC for the CMIP6 models, which implies that the carbon regeneration due to $CaCO_3$ dissolution is lumped into the preformed DIC component. Thus, the preformed DIC is likely somewhat overestimated. All the models showed increasing storage of total DIC, regenerated DIC, and preformed DIC from the preindustrial era to 2100. In the deep ocean (> 2000m) the accumulation of regenerated DIC increases more quickly than preformed DIC storage, and accounts for 50% or more of deep ocean DIC storage by 2100 in all the models (Figs. 2.8-2.10).

In terms of the models with remineralization outputs available (variable name "remoc"), we separated the regenerated DIC into both biological and circulation-driven fractions (Fig. 2.13). The models consistently show a decreasing biological surface export of carbon in a warming climate. However, the increase in the regenerated DIC from the slowing circulation more than compensates (Fig. 2.13). These results support our conclusion that most of the carbon accumulation in the deep ocean is due to the slowdown of global overturning circulation that dominates over the decreasing (or flat in a couple of models) export flux from the surface.

Ocean Carbon Storage in CESMv1 (RCP8.5-ECP8.5)

Global Ocean dissolved inorganic carbon concentrations gradually increase over time as the oceans take up more and more anthropogenic CO_2, especially in the Southern Ocean. Ocean uptake of CO_2 peaks at ~5.5 PgC/yr in the late 21st century and then declines steadily over time, even as atmospheric CO_2 continues to rise, as surface waters become increasingly saturated (Moore et al., 2018, Kwiatkowski et al., 2019). The DIC increase in the surface ocean is much larger than in the deep ocean, due to the direct uptake of anthropogenic CO_2 from the atmosphere (Fig. 2.9). In the deep ocean, the DIC buildup over time is due mainly to the accumulation of carbon via the biological pump (~93% of deep ocean DIC increase). Thus, preformed DIC, which could include both natural and anthropogenic carbon, accounts for only ~7% of the deep ocean DIC storage by year 2300 (Fig. 2.9).

Chapter 3: Surface-to-Interior Transport Timescales and Ventilation Patterns in a Time-Dependent Circulation Driven by Sustained Climate Warming

Abstract

The effect of climate warming in response to rising atmospheric CO_2 on the ventilation of the ocean remains uncertain. Here we develop an offline tracer-transport model to characterize the ventilation patterns and timescales in the time-evolving circulation for the 1850-to-2300 period as simulated with the Community Earth System Model version 1 (CESMv1) under a business-as-usual warming scenario. We find that by 2300 2.1% less water originates from the high-latitude deep water formation regions (both hemispheres) compared to 1850. In compensation, there is an increase in the water originating from the subantarctic. Slowing meridional overturning circulation causes a gradual increase in mean age during the 1850 to 2300 period, with a globally averaged mean-age increase of ~110 years in 2300.

Where and when the water will be re-exposed to the atmosphere depends on the post-2300 circulation. For example, if we assume that the circulation persists in its year-2300 state (scenario 1), the mean interior-to-surface transit time in year 1850 is ~1140 years. In contrast, if we assume that the circulation abruptly recovers to its year-1850 state (scenario 2), the mean interior-to-surface transit time in 1850 is only ~740 years. By 2300, these differences become even larger; in scenario 1, the mean interior-to-surface transit time increases by ~200 years, whereas scenario 2 decreases by ~80 years. The dependence of interior-to-surface transit time on the future ocean circulation produces an additional unavoidable uncertainty in the long-term durability of marine carbon dioxide removal strategies.

Main text

The surface patterns and timescales with which the interior ocean is ventilated determine the ocean's ability to modulate the Earth's climate by taking up and redistributing heat and carbon (Katavouta et al., 2019). Here we focus on key timescales: the mean age, i.e., the mean transit time for water to be transported from the sea surface into the interior, and the mean first-passage time, i.e., the mean transit time for water to be transported from the ocean interior back to the surface. The theory describing transit-time distributions for stationary flows and its connection to the ideal-age tracer that is included in many Earth System Models (e.g., Moore et al., 2018) is well-developed (Delhez et al., 1999; Holzer et al., 2000; Khatiwala et al., 2001; Deleersnijder et al., 2001; Primeau 2005). At steady-state in a time-invariant flow, the ideal age is equal to the mean of the last-passage time distribution, i.e., to the mean age (Primeau, 2005). The mean of the first-passage time distribution has received less attention, but it is particularly useful for quantifying carbon sequestration (DeVries et al., 2012; Siegel et al., 2021). However, in situations where the ocean circulation is evolving in time due to global warming, neither the mean age nor the mean first-passage time has received much attention.

Indeed, most previous studies have focused on the present-day circulation, treating it as stationary with no secular trends in the overturning circulation (e.g., Primeau, 2005, DeVries and Primeau, 2011; Shah et al., 2017; Rousselet et al., 2021). Recently, Chamberlain et al. 2019, and Holzer et al. 2020, examined mean transit times in ocean circulation states diagnosed from a transient climate change simulation. However, they treated the decadal-mean snapshots captured during a transient climate warming simulation as if they could be applied indefinitely into the past and future without considering the fact that the snapshots were part of a climate state that was evolving on longer timescales. Here we apply transit-time diagnostics to a time-evolving flow without making any stationarity assumption. Moreover, we do this in the context of a transient climate change simulation for the 1850-to-2300 period in a business-as-usual warming scenario in which the global overturning circulation eventually collapses (Moore et al. 2018).

We aim to answer two questions: 1) What are the ocean ventilation time scales in a situation where the circulation is evolving in time due to climate warming? 2) What are the regional variations in the fraction of the interior ocean volume ventilated from different regions of the surface ocean, and how are these regional fractions changing with time?

In the Method section, we describe the development of an offline model for a CESM CMIP5 simulation. We also provide a detailed mathematical strategy based on the theory of Green functions to address our questions in a computationally efficient way. The Results section describes the time-evolving circulation and ocean stratification before presenting our ventilation diagnostics. These include two-dimensional maps showing the fraction of the interior ocean volume ventilated from different surface regions and zonally-averaged depth-latitude plots of the mean age averaged over decades separated by 100 years. We also show a time series of the globally-averaged mean age and mean first-passage time from 1850 to 2300. The Discussion and Summary section summarizes the paper's key findings and lists some limitations of the study and prospects for future work.

Methods

Development of the Offline Tracer Transport Model

To investigate ocean ventilation patterns and timescales, we developed an offline tracer transport model using outputs from the Community Earth System Model CESM1.0 POP2. We applied it to a simulation under a high-end warming scenario RCP8.5-ECP8.5 for the period from the year 1850 to 2300 (see Moore et al., 2018 for more details about this particular simulation). The simulation is part of the Coupled Model Intercomparison Project phase 5 (CMIP5).

Our offline model is implemented as a series of annual transport operators written in the form of sparse matrices. Previous studies have validated that the Transport Matrix Method (TMM) faithfully represented most aspects of the parent online model (Bardin et al., 2016; Kvale et al., 2017). The action of the transport operator $\boldsymbol{T}(\mathrm{t})$ on a tracer field, yields the advective-diffusive flux divergence of the tracer. The transport operator $\boldsymbol{T}(\mathrm{t})$ comprises three physical processes, advection, horizontal diffusion and vertical diffusion:

$$\boldsymbol{T}(\mathrm{t}) \equiv \boldsymbol{A}(\mathrm{t}) + \boldsymbol{D}(\mathrm{t}) + \boldsymbol{H}(\mathrm{t})$$

where $\boldsymbol{A}$ includes both the explicit advection and the bolus advection driven by the GM eddy parameterization. The Redi diffusive flux divergence associated with the GM scheme is incorporated in the $\boldsymbol{H}$ and $\boldsymbol{D}$ diffusion operators. The vertical diffusion associated with the KPP mixing scheme is also folded into $\boldsymbol{D}$. We separate the transport operator into these three parts, so that we can use different time-stepping schemes (see below) for the different processes.

To reconstruct the Redi diffusivity tensor, we computed the isopycnal slope from the saved annual-averaged density fields. We also used the saved annual-averaged isopycnal, horizontal and vertical diffusivity fields. To reconstruct the advection operator, we combined the saved annual-averaged explicit velocity with the GM bolus velocity fields. This approach is similar to the one used in Primeau (2005) and Chamberlain et al. (2019) but different than the method used in Kvale et al. (2017) and Bardin and Primeau (2014), which used the impulse response functions to contruct the advection and diffusion operators (Khatiwala et al., 2005). In terms of the spatial discretization, we followed the scheme described in the POP manual (Smith et al., 2010). However, we neglected the variable thickness of the top layer of the model. We therefore corrected the annual-averaged velocity field to ensure that its three-dimensional divergence vanishes. The correction was applied to the horizontal velocity in the top model layer following the method described in Bardin and Primeau (2014). No-flux conditions are built into the operator at all the solid basin boundaries and the sea surface.

The offline model's resolution is the original CESMv1 resolution. In total, there are n = 4,241,988 wet grids in the model, of which n_s = 85813 are in the surface layer. Thus, $\boldsymbol{T}(t)$ consists of 451 $n \times n$ sparse matrices for the period from the year 1850 to 2300. For example, if $\boldsymbol{c}$ represents a tracer concentration field, then it can be represented as a $n \times 1$ column vector, $\boldsymbol{c}$. the time tendency of the tracer $\boldsymbol{c}$ is governed by the following system of ordinary differential equations

$$\frac{d\boldsymbol{c}}{dt} + \boldsymbol{T}(t)\boldsymbol{c} = \boldsymbol{s}(t), \qquad (1)$$

where $\boldsymbol{s}(t)$ is a discretized source and sink function expressed as a column vector. Because we do not know what the circulation will be beyond the year 2300 in our analysis we assume that the circulation is constant after year 2300. We consider two scenarios. In one we assume that the year-2300 circulation persists without changing for $t > 2300$. In the second one, we assume that the circulation abruptly returns to its 1850 state and stays permanently in the 1850 state for $t > 2300$.

This offline model can be stepped forward and backward in time by employing an implicit first-order Euler-backward scheme for vertical diffusion, an explicit (3rd order Adam-Bashforth) scheme for advection, and the Euler-forward scheme for horizontal diffusion and source and sink terms. The time step is set to one hour.

Surface-to-Interior Ventilation Patterns and Timescales in a Time-dependent Flow

If we consider a fluid particle in the ocean interior at time t, its residence time, defined as the time between successive surface contacts, can be decomposed into two parts

$$\tau(t) = \tau^{\downarrow}(t) + \tau^{\uparrow}(t). \qquad (2)$$

where $\tau^{\downarrow}$ is the surface-to-interior transit time, also known as the age or last-passage time, and $\tau^{\uparrow}$is the interior-to-surface transit time, also known as the first-passage time (Primeau, 2005; Primeau and Holzer, 2006). In an advective-diffusive flow, water parcels have a distribution of transit times. Our focus is on the properties of these time-dependent distributions rather than on the transit times of individual Lagrangian particles.

For our discretized ocean circulation model, each grid-box can be characterized by a pair of transit-time distributions, which can be organized as $\boldsymbol{g}^{\downarrow}(\tau^{\downarrow};t)$ and $\boldsymbol{g}^{\uparrow}(\tau^{\uparrow};t)$. Note that for a water parcel in the ocean interior at time t, the interior-to-surface transit-time distribution depends on the circulation at times greater than t, while the surface-to-interior transit time distribution depends on the circulation at times less than t. These distributions can be expressed in terms of the Green functions for the forward and time-reversed adjoint transport equations subject to a rapid loss term in the top model layer. Specifically, the interior-to-surface transit time distribution is given by

$$\boldsymbol{g}^{\uparrow}\left(\tau^{\uparrow};t\right) = \boldsymbol{R}_s \boldsymbol{V} \boldsymbol{G}^{\uparrow}\left(t+\tau^{\uparrow};t\right), \qquad (3)$$

where $\boldsymbol{G}^{\uparrow}$ is a space-discretized version of the Green function for the transport equation

$$\frac{\partial}{\partial t}\boldsymbol{G}^{\uparrow}(t;t') + [\boldsymbol{T}(t)+\boldsymbol{R}]\boldsymbol{G}^{\uparrow}(t;t') = 0, \qquad (4)$$

$$\boldsymbol{G}^{\uparrow}(t';t') = \boldsymbol{V}^{-1}$$

in which $\boldsymbol{T}(t)$ is the discretized advective-diffusive tracer flux divergence operator written in matrix form; $\boldsymbol{R}$ is the loss frequency expressed as a diagonal matrix whose only non-zero elements are in the columns (and rows) corresponding to the surface grid-boxes. The elements of $\boldsymbol{R}$ are given by $R_{ii} = (1\ \mathrm{hr})^{-1}$ if i corresponds to a grid box in the top layer of the model and zero otherwise. In equation (2), $\boldsymbol{V}$ is a diagonal matrix whose non-zero elements are the volumes of the model grid boxes. The matrix $\boldsymbol{R}_s$ is an $n_s \times n$ matrix formed from the n_s rows of $\boldsymbol{R}$ corresponding to the model's grid boxes in direct contact with the atmosphere. Thus $\boldsymbol{g}^{\uparrow}\left(\tau^{\uparrow};t\right)d\tau^{\uparrow}$ is an $n_s \times n$ matrix whose ij-th element gives the fraction of the water volume in the j-th grid box at time t that will first come in contact with the atmosphere in the i-th surface grid box and whose interior-to-surface transit times will be between $\tau^{\uparrow}$ and $\tau^{\uparrow} + d\tau^{\uparrow}$.

Similarly, the surface-to-interior transit time distribution is given by

$$\boldsymbol{g}^{\downarrow}(\tau^{\downarrow};t) = \boldsymbol{R}_s \boldsymbol{V} \boldsymbol{G}^{\downarrow}(t+\tau^{\downarrow};t), \qquad (5)$$

where $\boldsymbol{G}^{\downarrow}$ is the green function for the time-reversed adjoint equation

$$\frac{\partial}{\partial t}\boldsymbol{G}^{\downarrow}(t'-t;t') + [\boldsymbol{T}^{\dagger}(t'-t) + \boldsymbol{R}]\boldsymbol{G}^{\downarrow}(t'-t;t') = 0, \qquad (6)$$

$$\boldsymbol{G}^{\downarrow}(t';t') = \boldsymbol{V}^{-1},$$

where $\boldsymbol{T}^{\dagger}(t'-t) = \boldsymbol{V}^{-1}\boldsymbol{T}^{T}(t'-t)\boldsymbol{V}$ is the adjoint tracer transport matrix. The ij-th element of $\boldsymbol{g}^{\downarrow}(\tau^{\downarrow};t)$ is the fraction of the water volume in the j-th grid box at time t that was last in contact with the atmosphere in the i-th surface grid box and whose surface-to-interior transit times are between $\tau^{\downarrow}$and $\tau^{\downarrow} + d\tau^{\downarrow}$.

The forward and adjoint Green functions, $\boldsymbol{G}^{\uparrow}$ and $\boldsymbol{G}^{\downarrow}$ can be related to each other. Using the semi-group property of the the Green function, we have

$$\boldsymbol{G}^{\uparrow}(t_1;t_0) = \boldsymbol{G}^{\uparrow}(t_1;t)\boldsymbol{V}\boldsymbol{G}^{\uparrow}(t;t_0). \qquad (7)$$

Equation (7) simply states that propagating an initial condition from t_0 to t_1 is equivalent to propagating the solution from t_0 to some intermediate time, t, and then from t to t_1. Differentiating equation (7) with respect to t gives

$$0 = \frac{\partial \boldsymbol{G}^{\uparrow}(t_1;t)}{\partial t}\boldsymbol{V}\boldsymbol{G}^{\uparrow}(t;t_0) + \boldsymbol{G}^{\uparrow}(t_1;t)\boldsymbol{V}\frac{\partial \boldsymbol{G}^{\uparrow}(t;t_0)}{\partial t}, \qquad (8)$$

and then using equation (4) to eliminate the time derivative in the second term on the right yields

$$0 = \frac{\partial \boldsymbol{G}^{\uparrow}(t_1;t)}{\partial t}\boldsymbol{V}\boldsymbol{G}^{\uparrow}(t;t_0) - \boldsymbol{G}^{\uparrow}(t_1;t)\boldsymbol{V}(\boldsymbol{T}(t) + \boldsymbol{R})\boldsymbol{G}^{\uparrow}(t;t_0). \qquad (9)$$

Post-multiplying equation (9) by $\left(\boldsymbol{V}\boldsymbol{G}^{\uparrow}(t;t_0)\right)^{-1}$ yields

$$\frac{\partial \boldsymbol{G}^{\uparrow}(t_1;t)}{\partial t} - \boldsymbol{G}^{\uparrow}(t_1;t)\boldsymbol{V}(\boldsymbol{T}(t)+\boldsymbol{R})\boldsymbol{V}^{-1} = 0,$$

then taking the transpose yields

$$\frac{\partial\left(\boldsymbol{G}^{\uparrow}(t_1;t)\right)^T}{\partial t} - (\boldsymbol{T}^{\dagger}(t)+\boldsymbol{R})\left(\boldsymbol{G}^{\uparrow}(t_1;t)\right)^T = 0. \quad (10)$$

We now do a change of variables from $t = t' - t^*$ to get

$$-\frac{\partial\left(\boldsymbol{G}^{\uparrow}(t_1;t'-t^*)\right)^T}{\partial t^*} - (\boldsymbol{T}^{\dagger}(t'-t^*)+\boldsymbol{R})\left(\boldsymbol{G}^{\uparrow}(t_1;t'-t^*)\right)^T = 0. \quad (11)$$

Comparing equation (11) and to equation (6), reveals the relationship between $\boldsymbol{G}^{\uparrow}(t;t')$ and $\boldsymbol{G}^{\downarrow}(t;t')$

$$\boldsymbol{G}^{\downarrow}(t'-t;t') = \left(\boldsymbol{G}^{\uparrow}(t';t'-t)\right)^T. \quad (12)$$

2.2.1 Surface-to-Interior Ventilation Patterns

Computing the full $\boldsymbol{G}^{\uparrow}$ and $\boldsymbol{G}^{\downarrow}$ is computationally too expensive because each column requires the simulation of an independent tracer. However, not all the information that could be extracted from the Green function is needed for our diagnostics. We are interested in the volume of the ocean re-exposed to the atmosphere through each surface pixel averaged over all possible transit times, i.e.,

$$\langle \boldsymbol{h}_s^{\uparrow} \rangle(t') = \int_0^{\infty} \boldsymbol{A}_s^{-\mathbf{1}} \boldsymbol{g}^{\uparrow}\left(\tau^{\uparrow}; t'\right) \boldsymbol{V}\mathbf{1} d\tau^{\uparrow}, \qquad (13)$$

where these volumes have been scaled by the area of the surface pixels to get equivalent thicknesses. In the above expressions, $\boldsymbol{A}_s$ is an $n_s \times n_s$ diagonal matrix formed from the horizontal areas of the model's grid boxes; $\mathbf{1}$ is an $n \times 1$ vector of ones so that the factor of $\boldsymbol{V}\mathbf{1}$ to the right of $\boldsymbol{g}^{\uparrow}$ acts to initialize the tracer concentration to unity everywhere inside the ocean. The fact that $\boldsymbol{g}^{\uparrow}\boldsymbol{V}\mathbf{1}$ is an $n \times 1$ column vector implies that the $\langle \boldsymbol{h}_s^{\uparrow} \rangle$ diagnostic can be computed from a single tracer. Thus we introduce the following tracer equation,

$$\frac{\partial}{\partial \tau^{\uparrow}} \boldsymbol{c}\left(\tau^{\uparrow}; t'\right) + \left[\boldsymbol{T}\left(t' + \tau^{\uparrow}\right) + \boldsymbol{R}\right] \boldsymbol{c}\left(\tau^{\uparrow}; t'\right) = 0, \qquad (14)$$

$$\boldsymbol{c}(0; t') = \mathbf{1},$$

where $\boldsymbol{c}$ is the tracer concentration so that equation (13) can be rewritten as

$$\langle \boldsymbol{h}_s^{\uparrow} \rangle(t') = \int_0^{\infty} \boldsymbol{R}_s \boldsymbol{V} \boldsymbol{c}\left(\tau^{\uparrow}; t'\right) d\tau^{\uparrow}, \qquad (15)$$

where we used equation (3) and the fact that $\boldsymbol{c}$ can be expressed in terms of the Green function, $\boldsymbol{c}\left(\tau^{\uparrow}; t'\right) = \boldsymbol{G}^{\uparrow}\left(t' + \tau^{\uparrow}; t'\right)\boldsymbol{V}\mathbf{1}$.

To further limit the needed computation, we evaluate integral in equation (13) for three separate values of t'. Thus, we start three tracer simulations using equation (14) starting from $t' = 1850$, $t' = 2090$ and $t' = 2290$ and time-step forward in time from $\tau^{\uparrow} = 0$ to $\tau^{\uparrow} = 2300 - t'$ (i.e., for 450 years, 240 years and 10 years respectively). The resulting tracer fields provide the integrand for the $\tau^{\uparrow} = 0$ to $\tau^{\uparrow} = 2300 - t'$ part of the integral in equation (15). The remaining part of the integral represents the forward integration from the year 2300 and can be obtained by direct matrix inversion because we assume that $\boldsymbol{T}$ is constant after year 2300:

$$\boldsymbol{c}^{\infty}(t') \equiv \int_{2300-t'}^{\infty} \boldsymbol{c}(\tau^{\uparrow};t')d\tau^{\uparrow} = [\boldsymbol{T}_{+} + \boldsymbol{R}]^{-\mathbf{1}}\boldsymbol{c}(2300-t';t'). \qquad (16)$$

where $\boldsymbol{T}_{+}$ is the time-invariant transport operator assumed to apply for the period after year 2300. We consider two scenarios for $\boldsymbol{T}_{+}$ after year 2300. In scenario 1 the circulation is assumed to persist in its year-2300 state indefinitely with $\boldsymbol{T}_{+} = \boldsymbol{T}(2300)$ while in scenario 2 the circulation is assumed to abruptly return to its year-1850 state after 2300 with $\boldsymbol{T}_{+} = \boldsymbol{T}(1850)$. Putting all this together we have

$$\langle \boldsymbol{h}_{s}^{\uparrow}\rangle(t') = \int_{0}^{2300-t'} \boldsymbol{A}_{s}^{-\mathbf{1}}\boldsymbol{R}_{s}\boldsymbol{V}\boldsymbol{c}(\tau^{\uparrow},t')d\tau^{\uparrow} + \boldsymbol{A}_{s}^{-\mathbf{1}}\boldsymbol{R}_{s}\boldsymbol{V}\boldsymbol{c}^{\infty}(t')\,. \qquad (17)$$

Finally, using $\langle \boldsymbol{h}_{s}^{\uparrow}\rangle$, the water volume fractions in 1850, 2090 and 2290 that will be first re-exposed to the atmosphere at each sea-surface pixel can be written as:

$$\langle \boldsymbol{f}_{s}^{\uparrow}\rangle(t') = \frac{\boldsymbol{A}_{\boldsymbol{s}}\langle \boldsymbol{h}_{s}^{\uparrow}\rangle(t')}{\mathbf{1}^{\boldsymbol{T}}\boldsymbol{V}\mathbf{1}}. \qquad (18)$$

Similarly, to compute the equivalent thickness for the flux of water that enters the ocean through each surface pixel we need to evaluate

$$\langle \boldsymbol{h}_{s}^{\downarrow}\rangle(t') = \int_{0}^{\infty} \boldsymbol{A}_{s}^{-\mathbf{1}}\boldsymbol{g}^{\downarrow}(\tau^{\downarrow};t')\boldsymbol{V}\mathbf{1}d\tau^{\downarrow}. \qquad (19)$$

We thus introduce the following adjoint tracer transport equation,

$$\frac{\partial}{\partial\tau^{\downarrow}}\boldsymbol{c}\big(\tau^{\downarrow};t'\big)+\big[\boldsymbol{T}^{\dagger}\big(t'-\tau^{\downarrow}\big)+\boldsymbol{R}\big]\boldsymbol{c}\big(\tau^{\downarrow};t'\big)=0, \qquad (20)$$

$$\boldsymbol{c}(0;t')=\ \mathbf{1}$$

so that equation (19) can be rewritten as

$$\langle\boldsymbol{h}_s^{\downarrow}\rangle(t')=\int_0^{\infty}\boldsymbol{R}_s\boldsymbol{V}\boldsymbol{c}\big(\tau^{\downarrow};t'\big)d\tau^{\downarrow}\,. \qquad (21)$$

Again, we further reduce the computational costs by focussing on three times $t'=1850$, $t'=2090$ and $t'=2290$. Thus, we start three tracer simulations using equation (20) starting from $t'=2290$, $t'=2090$ and $t'=1850$ and time-step backward in time from $\tau^{\downarrow}=0$ to $\tau^{\downarrow}=t'-1850$ (i.e., for 440 years, 240 years and 0 years respectively). The resulting tracer fields provide the integrand for the $\tau^{\downarrow}=0$ to $\tau^{\downarrow}=t'-1850$ part of the integral in equation (21). The remaining part of the integral represents the backward integration from the year 1850 and can be obtained by direct matrix inversion because we assume that $\boldsymbol{T}$ is constant before 1850:

$$\boldsymbol{c}_{-\infty}(t')\equiv\int_{t'-1850}^{\infty}\boldsymbol{c}\big(\tau^{\downarrow};t'\big)d\tau^{\downarrow}=[\boldsymbol{T}^{\dagger}(1850)+\boldsymbol{R}]^{-\mathbf{1}}\boldsymbol{c}(t'-1850;t'), \qquad (22)$$

Thus

$$\langle\boldsymbol{h}_s^{\downarrow}\rangle(t')=\boldsymbol{A}_s^{-\mathbf{1}}\boldsymbol{R}_s\boldsymbol{V}\boldsymbol{c}_{-\infty}(t')+\int_0^{t'-1850}\boldsymbol{A}_s^{-\mathbf{1}}\boldsymbol{R}_s\boldsymbol{V}\boldsymbol{c}(\tau^{\downarrow},t')d\tau^{\downarrow}. \qquad (23)$$

As before, the volume fractions of water in 1850, 2090 and 2290 that was last ventilated to the atmosphere at each surface pixel can be written as

$$\langle \boldsymbol{f}_s^{\downarrow} \rangle(t') = \frac{\boldsymbol{A_s} \langle \boldsymbol{h}_s^{\downarrow} \rangle(t')}{\mathbf{1}^{\boldsymbol{T}} \boldsymbol{V} \mathbf{1}}. \qquad (24)$$

2.2.2 Surface-to-Interior Timescales

In addtion to the volume fractions, we also present mean interior-to-surface transit times (i.e., mean first-passage time) from each interior ocean pixel to anywhere at the surface. Specifically,

$$\langle \tau^{\uparrow} \rangle^{T}(t') = \int_{t'}^{\infty} \tau^{\uparrow} \mathbf{1}_s^{T} \boldsymbol{g}^{\uparrow}(\tau^{\uparrow}; t') d\tau^{\uparrow}, \qquad (25)$$

where $\langle \tau^{\uparrow} \rangle$ is a row matrix of size of $1 \times n$ whose components are the mean first-passage times from each of the n model gridboxes. From equation (3) and the fact that $\mathbf{1}^{T} \boldsymbol{R} = \mathbf{1}_s^{T} \boldsymbol{R}_s$, we rewrite equation (25) as

$$\langle \tau^{\uparrow} \rangle^{T}(t') = \int_{t'}^{\infty} \tau^{\uparrow} \mathbf{1}^{T} \boldsymbol{R} \boldsymbol{V} \boldsymbol{G}^{\uparrow}(t' + \tau^{\uparrow}; t') d\tau^{\uparrow}, \qquad (26)$$

Note that applying the operator $\mathbf{1}^{T} \boldsymbol{V}$ to a tracer field corresponds to the integral over the volume of the ocean. Thus $\mathbf{1}^{T} \boldsymbol{V} \boldsymbol{T} \boldsymbol{f} \equiv 0$ for any $\boldsymbol{f}$ because the transport operator, written in flux-divergence form, conserves tracer mass. Equation (26) can thus be written as

$$\begin{aligned} \langle \tau^{\uparrow} \rangle^{T}(t') &= \int_{t'}^{\infty} \tau^{\uparrow} \left[\mathbf{1}^{T} \boldsymbol{V} \boldsymbol{R} \boldsymbol{G}^{\uparrow}(t' + \tau^{\uparrow}; t') + \mathbf{1}^{T} \boldsymbol{V} \boldsymbol{T}(t') \boldsymbol{G}^{\uparrow}(t' + \tau^{\uparrow}; t') \right] d\tau^{\uparrow}, \\ &= \int_{t'}^{\infty} \tau^{\uparrow} \mathbf{1}^{T} \boldsymbol{V} \left(\boldsymbol{R} + \boldsymbol{T}(t') \right) \boldsymbol{G}^{\uparrow}(t' + \tau^{\uparrow}; t') d\tau^{\uparrow}, \qquad (27) \end{aligned}$$

in which we added a term equal to zero. Doing so allows us to use equation (4) to rewrite equation (27) as follows:

$$\langle\tau^{\uparrow}\rangle^{T}(t') = -\int_{t'}^{\infty} \mathbf{1}^{T}\boldsymbol{V}\left[\tau^{\uparrow}\frac{\partial \boldsymbol{G}^{\uparrow}(t'+\tau^{\uparrow};t')}{\partial\tau^{\uparrow}}\right]d\tau^{\uparrow},$$

$$= \int_{t'}^{\infty} \mathbf{1}^{T}\boldsymbol{V}\boldsymbol{G}^{\uparrow}(t'+\tau^{\uparrow};t')d\tau^{\uparrow}, \qquad (28)$$

where we used integration by parts to go from the first to second line. If we now take the transpose of equation (28) we get

$$\langle\tau^{\uparrow}\rangle(t') = \int_{t'}^{\infty} \boldsymbol{G}^{\uparrow\boldsymbol{T}}(t'+\tau^{\uparrow};t')\boldsymbol{V}\mathbf{1}d\tau^{\uparrow},$$

$$= \int_{t'}^{\infty} \boldsymbol{G}^{\downarrow}(t';t'+\tau^{\uparrow})\boldsymbol{V}\mathbf{1}d\tau^{\uparrow},$$

$$= \int_{2300}^{\infty} \boldsymbol{G}^{\downarrow}(t';t'+\tau^{\uparrow})\boldsymbol{V}\mathbf{1}d\tau^{\uparrow} + \int_{t'}^{2300} \boldsymbol{G}^{\downarrow}(t';t'+\tau^{\uparrow})\boldsymbol{V}\mathbf{1}d\tau^{\uparrow}, \qquad (29)$$

which is the solution of the following equation:

$$\frac{\partial\langle\tau^{\uparrow}\rangle}{\partial t} + [\boldsymbol{T}^{\dagger}(t) + \boldsymbol{R}]\langle\tau^{\uparrow}\rangle = \mathbf{1}, \qquad (30)$$

subject to either of the following initial condition

$$\langle\tau^{\uparrow}\rangle(2300) = (\boldsymbol{T}^{\dagger}(2300) + \boldsymbol{R})^{-1}\mathbf{1},$$

or

$$\langle\tau^{\uparrow}\rangle(2300) = (\boldsymbol{T}^{\dagger}(1850) + \boldsymbol{R})^{-1}\mathbf{1}.$$

The first initial condition corresponds to the scenario in which the circulation is assumed to persists in the year 2300 state (scenario 1). The second initial condition corresponds to the assumption that the circulation abruptly recovers to its year 1850 state (scenario 2).

Similarly, the mean surface-to-interior transit times (i.e., mean last-passage time or mean age) at each pixel can be directly solved from the following equation

$$\frac{\partial\langle\tau^{\downarrow}\rangle}{\partial t} + [\boldsymbol{T}(t)]\langle\tau^{\downarrow}\rangle = \boldsymbol{R}\langle\tau^{\downarrow}\rangle + \mathbf{1}, \quad (31)$$

subject to the following initial condition

$$\langle\tau^{\downarrow}\rangle(1850) = (\boldsymbol{T}(1850) + \boldsymbol{R})^{-1}\mathbf{1}. \quad (32)$$

Equation (31) takes the form of the ideal age equation that is implemented in many ocean general circulation. It is important to note, however, the equation (31) only yields the mean of the TTD when it is initialized using the fully spun-up boundary condition given in equation (32).

3. Results

3.1 Global Overturning Circulation and Buoyancy Frequency

The global overturning circulation contains the upper cell and abyssal cell (Fig. 3.1). In our model, the preindustrial circulation is characterized by upwelling in the Antarctic Divergence (14.0 Sv) and equatorial upwelling zones (57.6 Sv). This upwelling is balanced by the downwelling that is driven by the convergence of surface wind-driven currents in the subtropical regions. A part of the water that is upwelled in the Antarctic (Circumpolar Deep Water, hereafter CDW) is transported southward as it loses buoyancy. This water forms Antarctic Bottom Water (AABW) and drives the abyssal cell of the southern meridional overturning circulation (SMOC, 9.0 Sv). In the Northern Hemisphere, the formation of North Atlantic Deep Water (NADW) drives the upper cell of the Atlantic meridional overturning circulation (AMOC) (21.7 Sv). The strength of AMOC and SMOC in our model compares well with the CMIP6 model mean strength of overturning circulation, even though the strength of SMOC is grossly underestimated compared with observational estimates (Liu et al., 2023).

In a warming climate, the formation of AABW and NADW weakens due to the stronger stratification driven by the gain of buoyancy, which leads to a slowdown of the global overturning circulation (Weijer et al., 2020; Heuzé, 2021; Liu et al., 2023). Furthermore, stronger westerlies drive stronger upwelling in the Antarctic Divergence zone, which is balanced by stronger downwelling in the subtropical gyres (Fig. 3.1G). This behavior is consistent with other estimates (Bracegirdle et al., 2013; Waugh, 2014; Waugh et al., 2013), even though the magnitude of these changes can vary across different estimates. Also by the end of the 21st century, the equatorial upwelling is 6.7 Sv weaker due to weaker equatorial easterlies compared to its preindustrial level in our model. Again, this behavior is generally consistent with other ESMs (Terada et al., 2020). Finally, the weaker equatorial easterlies also lead to a 3.0-6.8 Sv decrease of the wind-driven subtropical downwelling in both hemispheres (Fig. 3.1G). In the north Atlantic, the formation of NADW weakens by more than 50% by the end of the 21st century under the business-as-usual warming scenario, which is consistent with CMIP model studies and accordingly drives the weakening overturning circulation (Liu et al., 2019; Weijer et al., 2020).

Overall, the changes of overturning circulation will affect the ventilation of the ocean, but it is difficult to assess this effect directly. Moreover, most streamlines do not cross the surface mixed layer, making it difficult to relate changes in the overturning circulation with changes in ventilation. The complex relationship between the changing circulation and ventilation in a warming climate motivates us to develop a mathematical method to clearly quantify the transport timescales and ventilation patterns in a time-evolving ocean circulation.

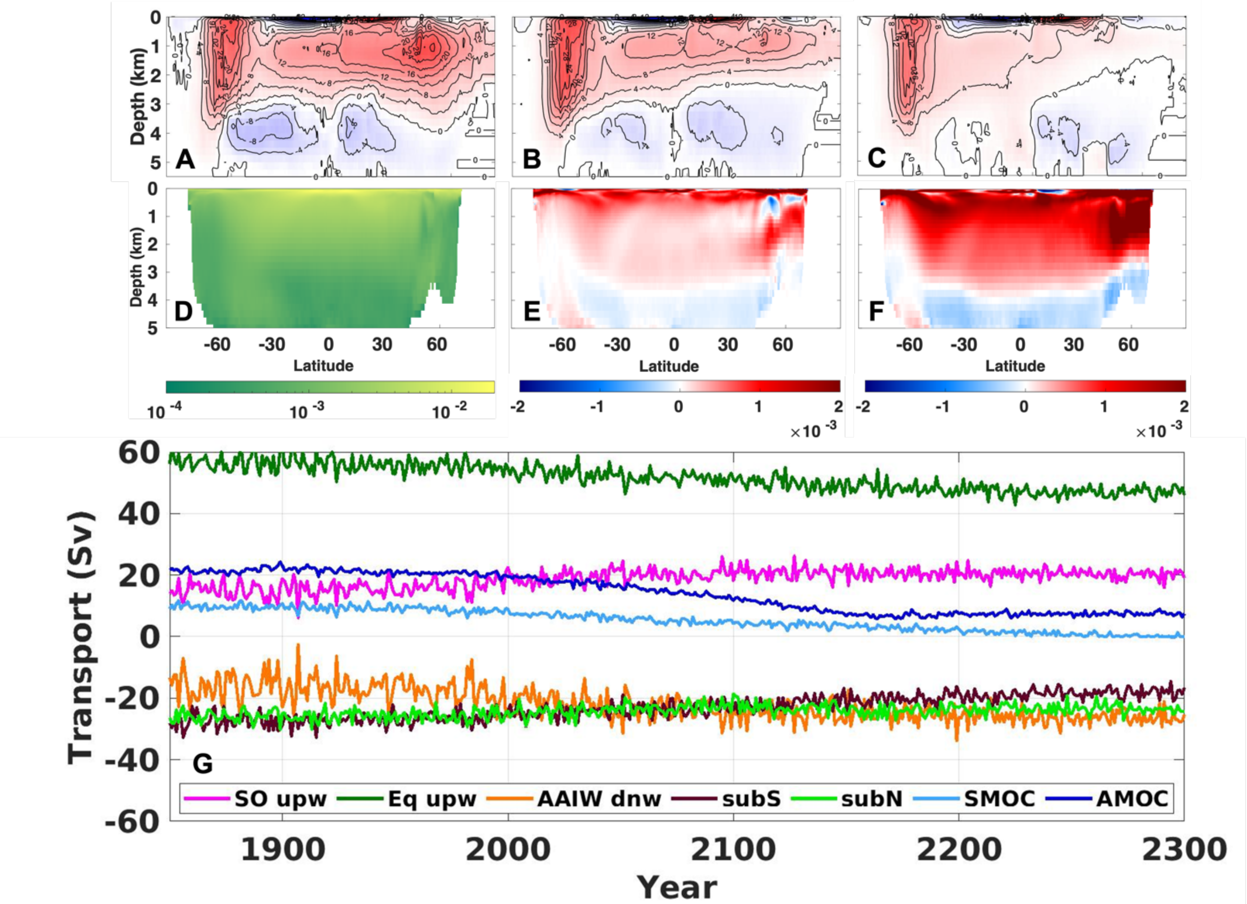

Figure 3.1. Ocean circulation and buoyancy frequency. CESMv1 global meridional overturning stream functions in A) preindustrial era (1850-1859), B) 2090s and C) 2290s. CESMv1 zonal mean buoyancy frequency in D) preindustrial era (1850-1859), E) the differences between 1850s and 2090s and F) the differences between 1850s and 2290s. G) represents key aspects of global ocean circulation: vertical transport at 100m of the Antarctic Divergence upwelling (SO, south of 60^{o}S), equatorial upwelling (Eq upw, 18S-18N), subantarctic downwelling (AAIW dnw, i.e., AAIW/SAMW formation, 60S-35S), southern hemisphere subtropical downwelling (subS, 35S-18S) and northern hemisphere subtropical downwelling (subN, 18N-35N), the strength of SMOC and AMOC (unit: Sv).

3.2 Ventilation volumes

The fraction of the ocean ventilated from each surface location provides a useful summary of the ocean's transport pathways. To summarize the results, we followed DeVries and Primeau (2012) and divided the surface into 7 broad zonal bands, which we further divided into separate basins, resulting in 17 patches that cover the whole ocean (Fig. 3.2). Fig. 3.3 shows a color map of these fractions per unit area for the year 1850 along with the change from 1850 to 2100 and from 1850 to 2300. Under the assumption that the ocean was in steady state up to the year 1850, our calculation shows that disproportionately more water was ventilated from high latitudes. We find that 27.2% and 37.2% of the total ocean volume were last ventilated from the North Atlantic and the Southern Ocean (i.e., Antarctic + Subantarctic), respectively (Fig. 3.3).

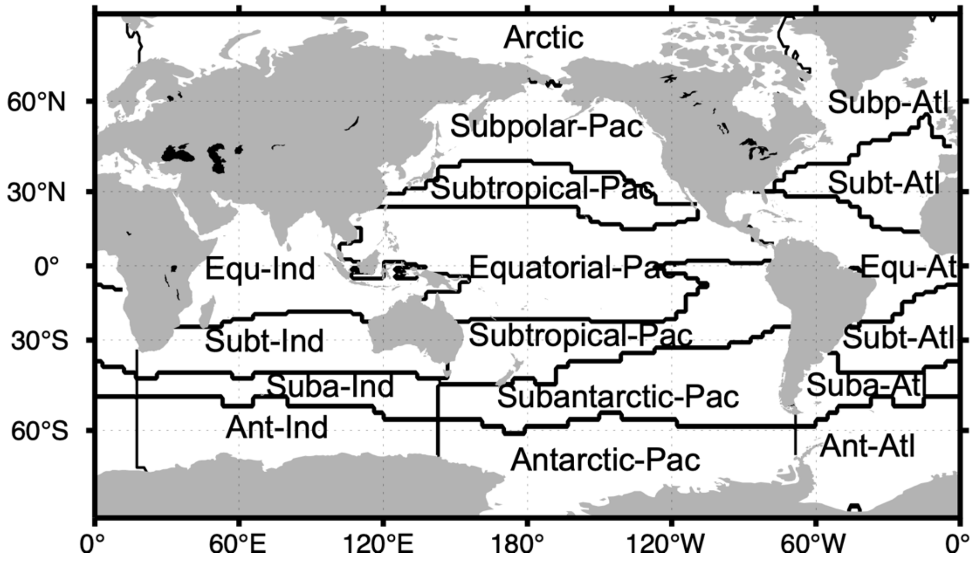

Figure 3.2. The separation of 17 surface patches. "Ant", "Suba", "Subt", "Equ", and "Subp" are short for Antarctic, Subantarctic, Subtropical, Equatorial and Subpolar, respectively.

Generally, our results show similar surface ventilation patterns as those obtained from data-constrained models (Gebbie and Huybers, 2010; DeVries and Primeau, 2012). One conspicuous exception is in the Southern Ocean. We estimated the fraction ventilated from the Antarctic region to be only 14.4% (Fig. 3.3), whereas DeVries and Primeau (2012) estimated 36%. This underestimation is possibly due to the inadequate representation of AABW formation in CESMv1. In the model, AABW formation is much lower than observation-based estimates and occurs through open-ocean convection instead of sinking along the Antarctic continental slope as is the case in the real world, a problem found in many Earth system models (Heuzé, 2021).

Our model shows how the simulated global water-mass ventilation changes as the climate warms. Consistent with the MOC weakening in a warming climate, we see the largest ventilation decreases in the North Atlantic and Weddell Sea. Of the total ocean volume, 1.9% less originates from the North Atlantic in 2290 compared to 1850. In the Weddell Sea, the decline is more gradual with 0.9% and 0.7% decreases in the 1850-2090 and 2090-2290 periods. To compensate the ventilation decreases in the North Atlantic and Weddell Sea, there are significant ventilation increases in the subantarctic region. These increases indicate stronger AAIW and SAMW formation rates (Fig. 3.1G) which are driven by stronger westerlies as a result of climate warming (Russell et al., 2006; Bracegirdle et al., 2013).

Besides these basin scale ventilation changes, there are also sub-basin scale ventilation-pattern shifts in response to climate warming. For example, the NADW formation regions shift, leading to less water originating from the Labrador Seas and more from the Norwegian-Greenland Seas (Fig. 3.3). This could be due to a weaker NAO in a warming

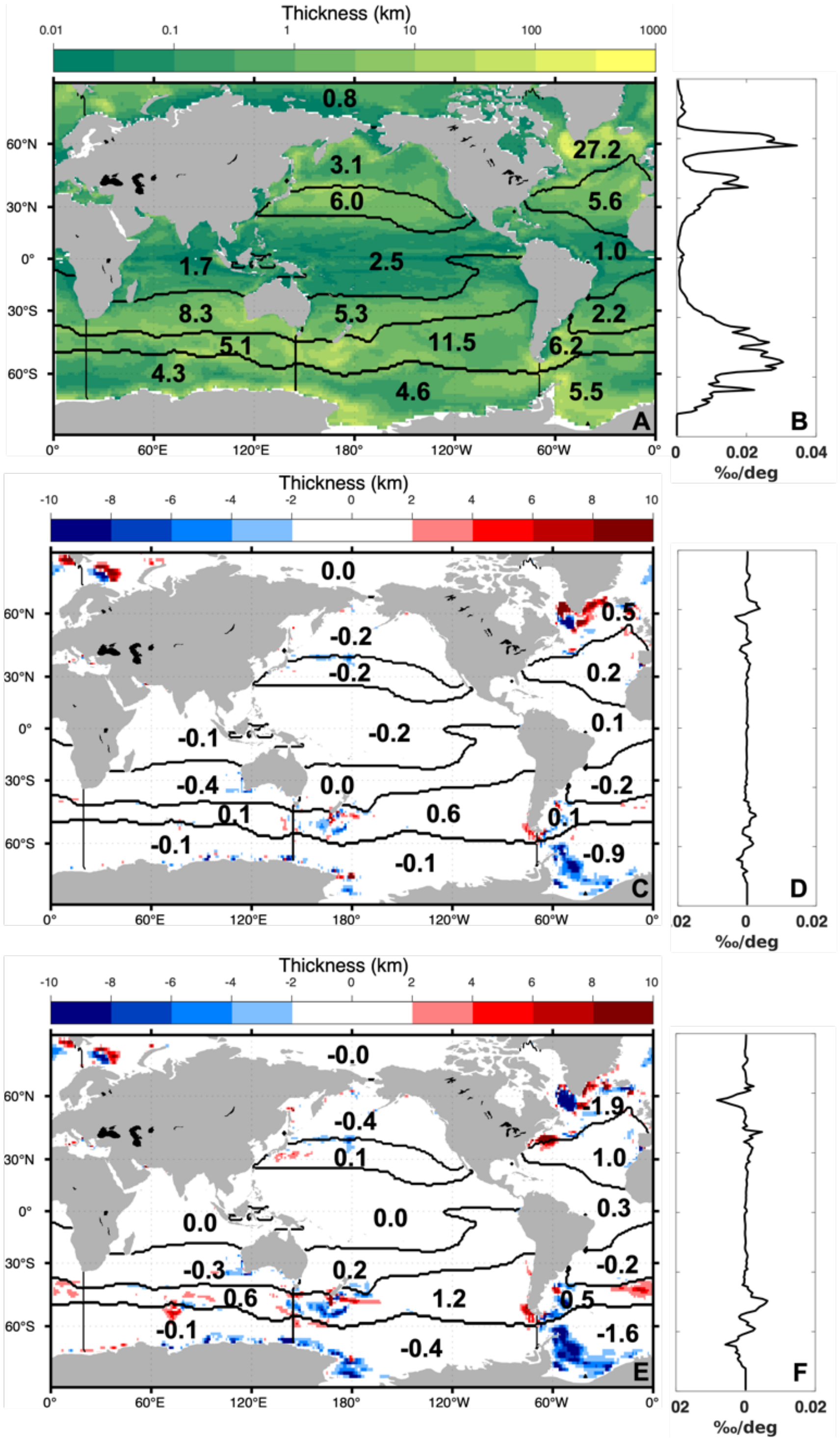

Figure 3.3. The surface sources of global ocean waters. The left panels represent the equivalent thickness from the oceanic volume that originated in each surface pixel, scaled by the surface area of each pixel (A) in the year 1850, (C) the difference between 2090 and 1850 and (E) the difference between 2290 and 1850 (unit: km). The color-scale follows a base-ten logarithm of the field in panel (A). The black number indicates the fraction (in percent) of

the whole water column that made last contact with the surface ocean in each region defined by the solid lines. The right panels show the zonal integration of the fraction along with each latitude bin (1°) (B) in the year 1850, (D) the difference between 2090 and 1850 and (F) the difference between 2290 and 1850 (unit: ‰/deg).

climate, as similar shifts on decadal timescales have been observed in decades with a weak NAO: The NADW originating from the Labrador Sea is weaker compared with the decades with a strong NAO, resulting in a weaker AMOC (Yeager and Danabasoglu, 2014).

The surface patterns showing where the interior ocean volume will eventually be re-exposed to the atmosphere depend both on the circulation changes from the year 1850 to 2300 and after the year 2300. As discussed in the Methods, we consider two scenarios that have the same time-dependent circulation up to the year 2300, but that differ afterwards. In scenario 1 the circulation is assumed to persist in its year-2300 state indefinitely while in scenario 2 the circulation is assumed to abruptly return to its year-1850 state after 2300. These two scenarios provide crude bounds on what could happen after atmospheric CO_2 stabilizes.

In general, most of the total water volume will ventilate the surface in the upwelling zones, regardless of the future circulation scenarios. The Southern Ocean (Antarctic + Subantarctic) is the largest region to ventilate the ocean water in the future, which will re-expose more than 45% of the total volume of the year-1850 ocean water to the atmosphere depending on the circulation scenarios. It is followed by regions with equatorial upwelling and intensified western boundary currents, such as Kuroshio Extension and Gulf Stream (Fig. 3.4).

In scenario 1, most of the ventilation changes occur between years 1850 and 2090 (Fig. 3.4). Of the total ocean volume in 1850, 62.7% will eventually ventilate to the surface in the Southern Ocean. In 2090, 1.7% more will ventilate in the Southern Ocean compared with the year 1850, whereas the fraction of the total ocean volume ventilating in the Southern Ocean will not change from the year 2090 to the year 2290. This increase is due to stronger Southern Ocean upwelling driven by stronger westerlies as a result of climate warming (Russell et al., 2006; Moore et al., 2018). To compensate for the ventilation increase, there is less water ventilation occurring in the Kuroshio Extension and Gulf Stream. In scenario 2, as the Southern Ocean will experience weaker upwelling after the year 2300, only 46.5% of the total ocean volume in 1850 will eventually be exposed to the atmosphere in the Southern Ocean. This number is about 16.2% less than it is in scenario 1. Over time, most of the ventilation changes occur between years 2090 and 2290 in scenario 2. Spatially, the ventilation changes showed contrary patterns with the changes in scenario 1.

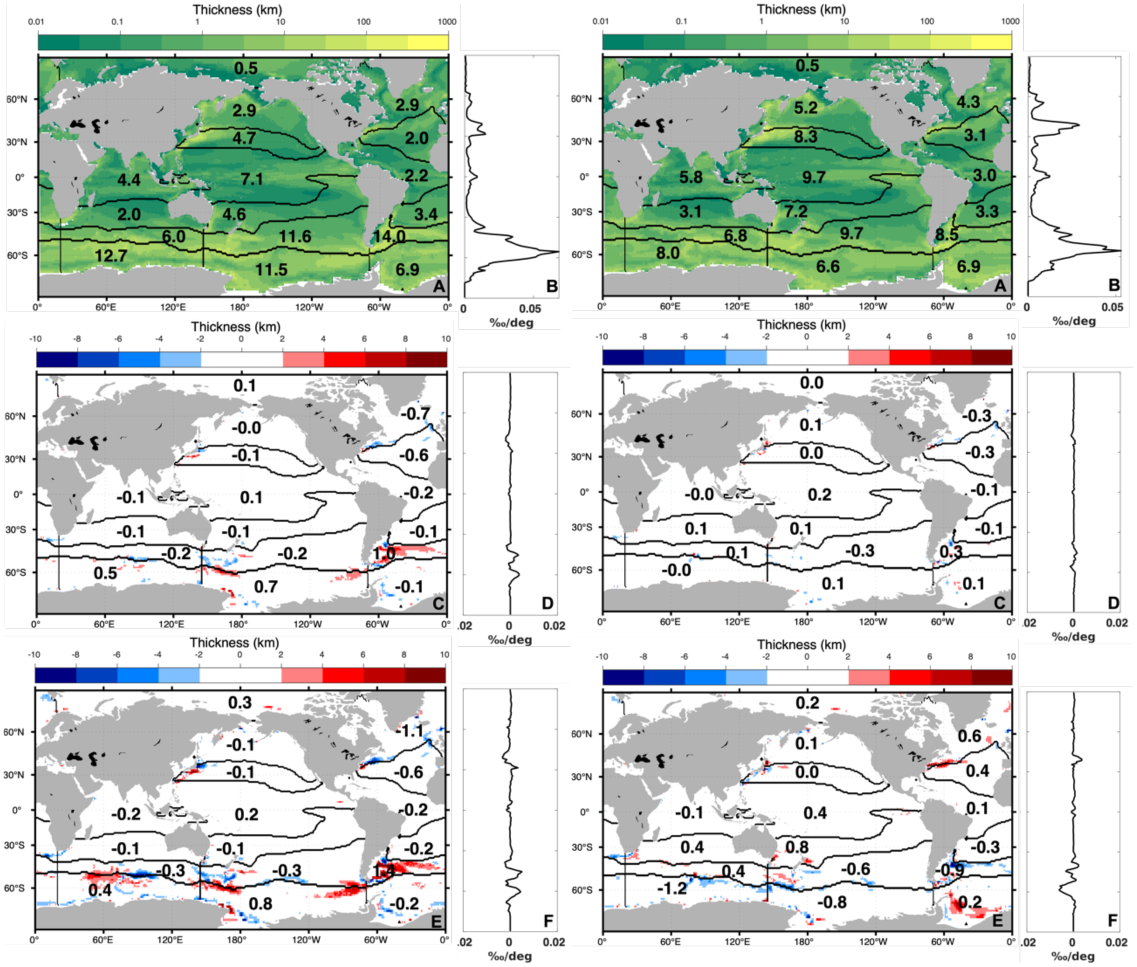

Figure 3.4. The fraction of whole water column where it made its next contact with the surface at each ocean grid in the experiment of scenario1 (left panels) and scenario2 (right panels). From the top to the bottom represents the fraction of the water column ventilating in each region in the year 1850 (top panel), year 2090 – year 1850 (middle panel) and year 2290 – year 1850 (bottom panel). The regions are defined by the solid black lines.

3.3 The mean age

As discussed in the introduction, the mean age is a useful diagnostic to characterize the timescales of ocean ventilation. It represents the elapsed time since a water parcel in the ocean interior made its last contact with the ocean surface. Fig. 3.5 shows zonally-averaged latitude-depth sections and a time series of the global mean age for year 1850, along with the difference in the mean ages at year 2090 minus year 1850 and year 2290 minus year 1850. Globally, the deep ocean has the oldest mean age of more than 1600 years for year 1850. The mean ages in the deep water formation regions (high latitudes) are much younger than the low latitudes. The upper ocean becomes slightly younger in the equatorial and subtropics, possibly due to the weakening downwelling despite the ocean becomes more stratified. With climate warming, the upper ocean becomes more stratified (Capotondi et al., 2012; Li et al., 2020), which correlates with the decreasing age in the upper ocean, decoupling from the deep water. As the global overturning circulation continues to slow down out to the year 2300, the mean age continues to increase, especially in the deepwater formation regions. It is worth noting that most of the changes in mean ages occur after year 2090 as most MOC slowdown and stratification increase occur after year 2090, supporting the conclusion in Moore et al., 2018 that it is important to extend the climate simulations beyond the 21st century.

To summarize, Fig. 3.5D shows the mean age for the whole ocean as a function of time. As climate warms, the global-averaged mean age increases from ~670 in 1850 to ~780 years in 2300. The upward trend in the mean age is still strong in year 2300 (Fig. 3.5D).

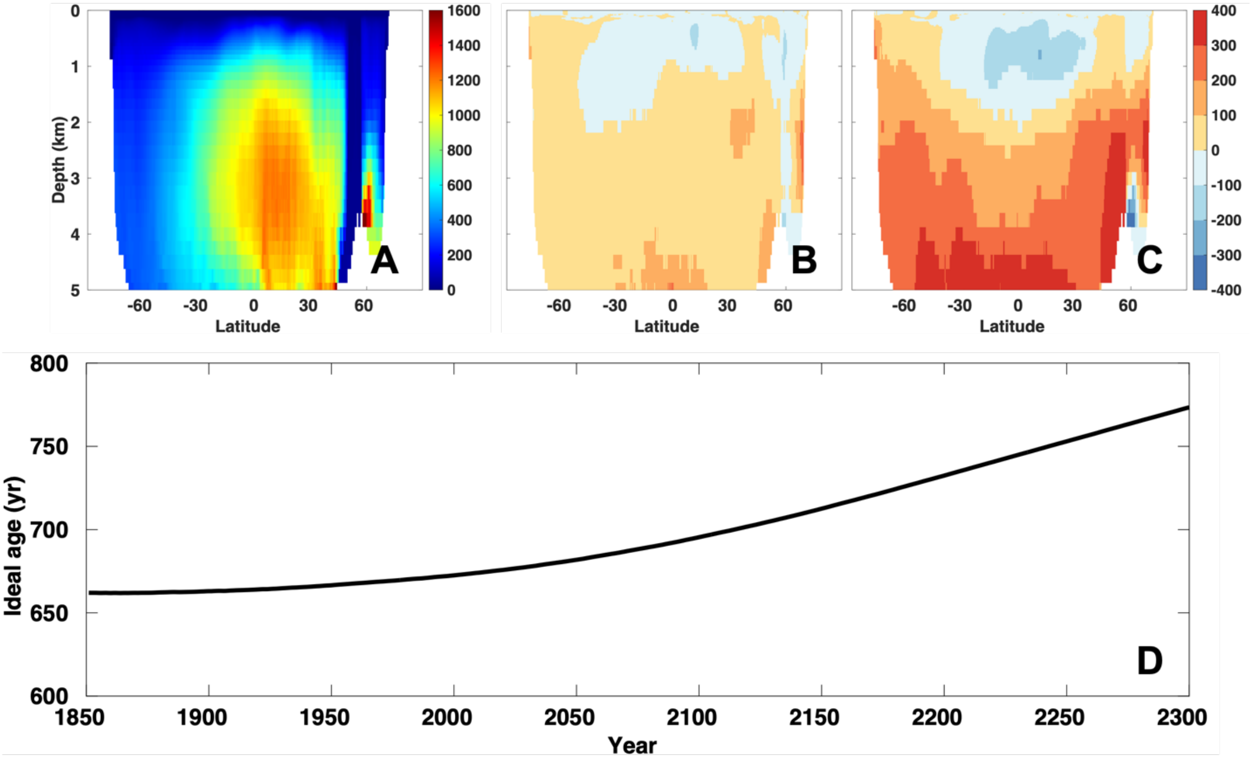

Figure 3.5. The global mean age. The top row shows zonally-averaged contour plots of the mean age in A) year 1850, B) the differences between the years 2090 and 1850 and C) the differences between the year 2290 and 1850. Panal D shows the time series of ideal age from the preindustrial era to year 2300 (unit: year).

3.4 The mean first-passage time

The mean first-passage time is a diagnostic of the time needed for a water parcel in the ocean interior to be transported back to the surface where it comes in contact with the atmosphere. Naturally, the first passage distribution for some time t' depends on the behavior of the ocean circulation at times $t > t'$. In particular it depends on the circulation at times beyond year 2300 when our climate simulation ends. As discussed in the Methods, we consider two scenarios that have the same time-dependent circulation up to year 2300, but that differ after year 2300. In scenario 1 the circulation is assumed to persist in its year-

2300 state indefinitely while in scenario 2 the circualtion is assumed to abruptly return to its year-1850 state after year 2300. While the results are qualitatively similar for the two scenarios, there are significant quantitative differences.

Our calculations show that, as expected, the mean first-passage time is longer in the deep ocean than in the upper ocean regardless of the scenario (Fig. 3.6A, 3.6D). Also, independent of scenario, the mean first-passage time for the deep waters is generally shorter at high latitudes compared to lower latitudes. This behavior is due to deep convection at high latitudes that can ventilate the deep ocean by rapidly mixing deep waters with the surface. However, the different assumptions about what happens after year 2300 have a large impact on the deep ocean's mean first-passage time. For example, in the northern-hemisphere, the zonally-averaged mean first-passage time in the deep ocean is approximately 800 years longer for scenario 1 compared to scenario 2 (c.f. ~2300 yrs for scenario1 vs. ~1500 years for scenario 2; Fig. 3.6A, 3.6D).

In scenario 1 the mean first-passage time increases almost everywhere and is particularly pronounced in the location of deep-water formation in the northern hemisphere and in regions downstream of the North Atlantic deep convection site (Fig. 3.6B, 3.6C). The change shown in Fig. 3.6B demonstrates the influence of the decline of the maximum AMOC strength from 20 Sv to 12 Sv between 1850 and 2090 (see Fig. 3.1G). The further decline in the strength of AMOC from 12 Sv to 7 Sv between years 2090 and 2290 has a relatively smaller impact on the mean first-passage time (c.f. Fig. 3.6C versus Fig. 3.6B). This behavior shows the importance of eddy-diffusive transport, which prevents the first-passage time from increasing to infinity as the overturning circulation collapses. The importance of diffusive transport has also been highlighted by Holzer et al. (2021).

In scenario 2 if we compare the change in the mean first-passage time for year 1850 to that of year 2090, we see an increase in the upper ocean and a decrease in deeper waters (Fig. 3.6E). This pattern of change can be understood in terms of the mean first-passage time itself. Where the mean first-passage time is on the order of 200 years or less, the weaker ventilation associated with the slowdown in the circulation for the 2090-to-2290 period will have a relatively large impact. In contrast, where the mean first passage time is much greater than 200 years, the post-2300 circulation dominates. Because in scenario 2 this circulation is a return to the vigorous 1850 circulation, we see a decrease in the year-2090 mean first-passage time over most of the deep ocean. On the other hand, if we compare the mean first-passage time for the year-1850 to that of the year-2290, we see a decrease almost everywhere (Fig. 3.6F). In this case, the whole ocean experiences the more vigorous 1850 circulation. The AMOC slowdown that occurred during the 1850-to-2300 period does not affect the year-2300 first passage-time distribution.

To summarize, Fig. 3.6G shows the mean first-passage time for the whole ocean. What we assume for the circulation after year-2300, when our simulation ends, has a significant impact. Assuming that the year-2300 circulation persists indefinitely, the whole-ocean mean first-passage time is about ~1140 years in 1850. As climate warms, the global-averaged mean first-passage time increases to ~1340 yrs in 2300. If, instead, we assume that in the year-2300, the circulation abruptly returns to its 1850 state the mean first-passage time is only ~740 years in 1850 and then decreases back to ~650 years.

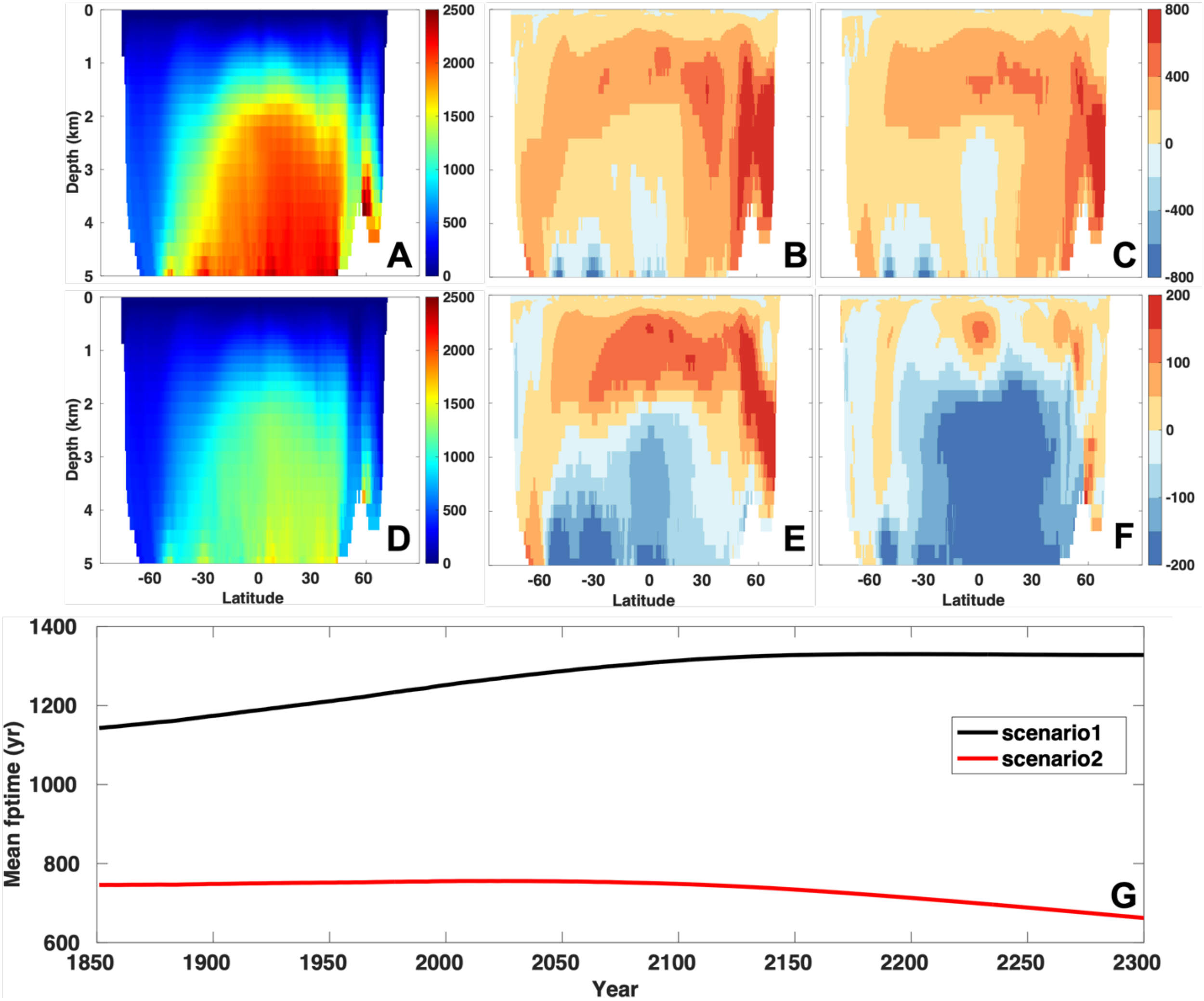

Figure 3.6. The global mean first passage time. The panels in the top row (A-C) correspond to scenario 1 in which the year-2300 circulation is assumed to persist indefinitely. The panels in the second row correspond to scenario 2, where the circulation is assumed to abruptly return to its 1850 state after year 2300 (D-F). The zonal average of the first-passage time was averaged for the 1850-1859 decade (A and D). Panels B and E show the differences between the 2090-2099 and 1850-1859 decadal averages. Panels C and F show the differences between 2290-2299 and 1850-1859 decadal averages. Panel G shows the time series of the globally-integrated first-passage time for each scenario (unit: years).

4. Summary and Discussion

We applied the theory of transit time distributions (TTD) to a transient circulation obtained from a realistic climate simulation in CESMv1 run from the year 1850 to the year 2300 under the RCP8.5-ECP8.5 climate scenario. We computed how the global ventilation patterns evolve in a transient circulation using the forward and adjoint transport operators derived from the CESMv1 simulation. In addition, we showed that the ideal age equation applied to a transient flow yields the time-evolving mean age provided that the ideal age is initialized with the mean of the TTD at the beginning of the simulation. Similarly, we showed that the mean first-passage time satisfies an equation similar to the ideal age equation except that it uses the time-reversed adjoint transport operator. We used these equations to compute the time-evolving mean age and mean first-passage time.

Ours is the first calculation that provides a proper treatment of the time-evolving ventilation patterns and timescales in a global circulation model subject to climate change. Previous calculations, for example, DeVries and Primeau (2012) and Gebbies and Huyber (2010) assumed the circulation to be in a steady state. Holzer et al. (2020) considered a time-evolving circulation, but they treated a sequence of decadal averaged transport operators as if they were steady-state circulations frozen in time and computed the ventilation patterns for each decade.

Under ongoing climate warming, of the total ocean volume, 2.1% less originates from the high latitudes (AABW and NADW formation regions) due to the slowdown of the global overturning circulation. In compensation, 2.2% more water originates from subantarctic regions. This indicates that the stronger upwelling in the Antarctic Divergence zone is balanced by stronger downwelling in the subtropical gyres (Fig. 3.1D). The fractions of the ocean ventilated in the future depend on the post-2300 circulation. The most conspicuous signal of the changes in future ventilation patterns is in the Southern Ocean, with the strongest upwelling zone. In the scenario that the circulation persists forever after the year 2300 (scenario 1) of the total ocean volume, 16.2% more of the year-1850 water will eventually ventilate in the Southern Ocean than the scenario with post-2300 circulation abruptly returning to its 1850-state (scenario 2). Of the total ocean volume of the year-2290 water, 15.1% more will eventually ventilate in the Southern Ocean in scenario 1 compared to scenario 2.

The ventilation timescales are also subject to climate change. We found that the slowing of overturning circulation leads to an increase of the global-averaged mean age by 17.2% (110 years) from 1850 to 2300. In contrast, using Holzer et al. (2020)'s approximation which treated a sequence of decadal averaged transport operators as if they were steady-state circulations frozen in time, we find that the global-averaged mean age increases from ~670 years to 1172 years. This indicates that the Holzer et al. (2020) approximation greatly overestimated the impacts of slowing overturning circulation on the mean age. The time-evolving circulation, along with the future circulation recovery trajectories, have large impacts on the global-averaged mean first-passage time. The Holzer et al. (2020) approximation did not consider the multiple potential circulation recovery trajectories after year 2300. In our study, we considered two circulation recovery scenarios after year 2300. In scenario 1 which the circulation at year 2300 persists infinitely, the global-averaged mean first-passage time increases from ~1140 years to ~1340 years from 1850 to 2300. In scenario 2 which the circulation at year 2300 abruptly recovers to its year-1850 state, the global-averaged mean first-passage time decreases from ~740 years to ~650 years. Therefore, to better estimate the mean first-passage time, we need to extend the model runs further into the far future (Frölicher et al, 2020; Schmittner et al., 2008). Without extending the simulation into the far future, we can only discuss the short time part of the first-passage time distribution because the mean of the whole distribution would not be available.

The increase in water mean age allows more nutrients to accumulate in the deep ocean before its returning back to the surface, leading to the decline of export productivity (Moore et al., 2018). Additionally, the increase in the mean age also allows more time for exported biogenic carbon to accumulate at depth, sequestering more carbon in the deep ocean by the biological pump (Liu et al., 2023) and potentially causing deoxygenation (Gnanadesikan et al., 2007). However, the mean first-passage time (Primeau, 2005) has received much less attention, but it is an equally important characteristic of ocean ventilation. It sheds light on the efficiency of the biological carbon pump by characterizing how long carbon exported to the deep ocean will remain isolated from the atmosphere (DeVries et al., 2012). Similarly, the time-evolving mean first-passage time provides a useful diagnostic for the long-term efficacy of carbon dioxide removal (CDR) strategies that aim to sequester carbon into the deep ocean (Siegel et al., 2021).

Several caveats apply to our study. First, our offline model is developed from the CESMv1 circulation, which underestimates the strength of the SMOC (Liu et al., 2023). In the offline model, we neglect the seasonal variabilities of the circulation, which could affect the mean age and mean first-passage time. Secondly, the circulation recovery trajectories after 2300 are highly uncertain, and we considered only two extreme scenarios. This limited exploration of possible future scenarios adds additional uncertainty to our mean first-passage time and ventilation patterns diagnostics. Finally, our study focused on one specific high-end climate scenario; other scenarios should be considered in future work.

Chapter 4: Long-term responses of the ocean carbon sink driven by multiple interacting ocean processes

Abstract

Ocean uptake of atmospheric CO_2 results from complex interactions between biological and physical processes. However, the impacts of each ocean process on the ocean carbon sink remains unclear. This study utilizes a linear inverse phosphorus and carbon cycling model to assess the relative contribution of various mechanisms to the global ocean carbon sink from 1850 to 2300 under a business-as-usual warming scenario (RCP8.5-ECP8.5). Sensitivity experiments are conducted to estimate the natural and anthropogenic components of ocean carbon uptake for multiple mechanisms. Rising atmospheric CO_2 is the primary driver of anthropogenic carbon uptake, whereas increasing temperature leads to natural carbon outgassing. The impact of time-evolving circulation on natural and anthropogenic carbon largely offset each other, but considering the biological processes that vary with circulation, the ocean carbon sink is reduced by about 580 PgC from 2100 onwards, potentially resulting in an extra 280 ppm increase in atmospheric CO_2 concentration compared with constant biological export production. Rising sea surface temperature plays a secondary role, leading to an extra 96 ppm increase of atmospheric CO_2. Changes in piston velocity have a minimal impact on the ocean carbon sink. This study provides insights into predicting the future of the global carbon cycle and its impacts on climate.

Introduction

The ocean absorbs approximately 25% of anthropogenic CO_2 emissions annually (Ciais et al., 2013; Friedlingstein et al., 2022). Because ocean carbon uptake occurs on millennia-scale timescales, understanding long-term changes in the ocean carbon cycle is critical for predicting the long-term evolution of the climate system (Plattner et al., 2008; Zickfeld et al., 2013).

Climate change reduces oceanic CO_2 uptake from the atmosphere, increasing CO_2 concentration in the atmosphere and causing further warming (Friedlingstein et al., 2006; Randerson et al., 2015). Global ocean carbon uptake is driven by rising atmospheric CO_2 in the first order, but it is also significantly modulated by multiple ocean processes (e.g. Ito et al., 2015; Bernardello et al., 2014). Typically, all extra carbon the ocean absorbs from atmosphere is referred to as anthropogenic carbon because it is driven by human induced CO_2 emissions. The assumption of this interpretation is that the natural atmospheric and ocean carbon pools do not significantly change (Sabine et al., 2004; Gruber et al., 2019; Khatiwala et al., 2009). However, state-of-the-art models agree that natural carbon is outgassing as climate warms (Fu et al., 2022; Holzer and DeVries, 2022), which indicates that the understanding the partitioning between natural and anthropogenic carbon uptake is necessary to understand the total ocean carbon sink.

Previous studies have suggested that temperature-driven feedback is the dominant mechanism affecting the ocean carbon sink. As the climate warms, the solubility of CO_2 in the ocean decreases, which in turn reduces ocean carbon uptake and further increases atmospheric CO_2 (Joos et al., 1999; Plattner et al., 2001; Matsumoto et al., 2010). However, the impacts of varying ocean circulation on the ocean carbon sink is still under debate. Some studies have found that changes in ocean circulation primarily reduce ocean carbon uptake by inhibiting the mixing of anthropogenic carbon into the deep ocean (Sarmiento et al., 1998; Matear and Hirst, 1999). These studies often assume that the strength of the biological pump remains constant and do not account for any climate-driven changes. Ridge and McKinley (2021) employed a 1D conceptual diffusive model to quantify the relative contributions of individual mechanisms and concluded that circulation changes have a negligible effect on anthropogenic ocean carbon uptake under moderate and high-end warming scenarios.

In contrary, Zickfeld et al. (2008) argued, based on an earth system model of intermediate complexity, that the reduction in ocean carbon uptake is largely due to a decline in the marine export of organic particulate matter, emphasizing the need to consider the changing role of biological pumps. Yamamoto et al. (2018) argued that varying circulation has only a minor direct role in the reduction of CO_2 uptake when the decline in the biological export production is considered under the scenario that CO_2 levels increase 1% per year from preindustrial levels until they reach four times those levels. Liu et al. (2023) argued that a slowing overturning circulation would reduce the total ocean carbon sink, based on comprehensive analysis of both ocean carbon pumps in the CMIP6 climate projections.

No previous studies have separated the contributions of individual mechanisms to natural and anthropogenic carbon cycling under the "business-as-usual" scenario extending into the year 2300. Here we use an offline, inverse model to quantify the impacts of key processes on ocean carbon uptake using time-varying physical state and circulation extracted from the Community Earth System Model (CESM) ECP8.5-ECP8.5 simulation. The extracted circulation is combined with a simplified inverse biogeochemical model to simulate the ocean biological pump and carbon cycling. In the combined model, each process can be held at preindustrial values or to change through time, allowing for quantitative assessment of the role of each process in total ocean carbon uptake.

The remainder of this paper is organized as follows: Section 2 outlines the model and experimental design. Sections 3.1 and 3.2 show the global map of natural and anthropogenic carbon uptake, as well as the model's physical and biological diagnostics. Section 3.3 focuses on the individual mechanisms affecting global ocean carbon uptake. Section 3.4 investigates the impacts of time-evolving circulation on both natural and anthropogenic carbon cycle. Section 3.5 investigates the role of changing biological export both natural and anthropogenic carbon cycle. Finally, Section 4 summarizes main findings of this study and discusses future implications of these findings on climate predictions.

2. Methods

2.1 Data

Observational concentrations of dissolved inorganic phosphorus (DIP), dissolved inorganic carbon (DIC), and ALK are downloaded from the Global Ocean Data Analysis Project website - the second version (GLODAPv2) (Lauvset et al., 2022). The data are then binned into the Community Earth System Model (CESMv1) grid that has a horizontal resolution of $1^{\circ} \times 1^{\circ}$ and vertically 60 layers with finer resolution in the upper ocean and coarser resolution in the deep ocean. The NPP product, carbon-based net primary production from Sea-viewing Wide Field-of-view Sensor (SeaWiFS CbPM averaged from Sep. 1997 to Dec. 2010), is from the Ocean Productivity website managed by Oregon State University (http://orca.science.oregonstate.edu/npp_products.php) and is then interpolated to the CESMv1 grid. The annual temperature, salinity, phosphorus and silicate are from CESMv1 outputs. The annual transport operators are also constructed from CESMv1 velocity and diffusivity coefficients (see Liu et al., 2023 for details). The climatological ocean phosphorus is from World Ocean Atlas 2018 (Garcia et al., 2019; Locarnini, 2018).

2.2 Biogeochemical Inverse Model

The model couples the cycling of phosphorus (P) and carbon (C). The phosphorus model is the base model that provides a biological uptake rate ($L(\mathbf{r})$, where $\mathbf{r}$ is a position coordinate) in P units, which is then converted to a DIC uptake rate in the carbon model by incorporating a variable C:P ratio ($r_{\mathrm{C:P}}$). In the P-cycle model, the DIP assimilation rate is modeled using a spatial pattern obtained from satellite-derived NPP (mg C m^{-2} day^{-1}) and a gridded surface DIP climatology as follows

$$L(\boldsymbol{r}) \equiv \begin{cases} \alpha \dfrac{[\frac{1}{r_{C:P}} \frac{NPP(\boldsymbol{r})}{NPP_0}]^{\beta}}{\frac{[DIP]_{obs}(\boldsymbol{r})}{[DIP]_0}}, if\ z < z_c \\ 0, \qquad otherwise \end{cases} \tag{1}$$

where NPP$_0$ and [DIP]$_0$ are 1 mmol C m^{-2} day^{-1} and 1 μM that are functioned to remove dimensions of NPP and DIP. α and β are adjustable parameters that are constrained by observational datasets. $r_{\mathrm{C:P}}$ is C:P ratio that is used to convert NPP from C unit to P unit, and it is modeled as $r_{C:P} = (0.006 + 0.0069[\mathrm{DIP}]_{obs})^{-1}$ (Galbraith and Martiny, 2015). z and z_C are water depth and the euphotic zone depth, respectively. Photosynthesis is assumed to occur only in the euphotic zone and to be zero below. The euphotic zone is defined as the top ten model layers (100 m).

2.2.1 Phosphorus model

We consider three pools of phosphorus: dissolved inorganic phosphorus (DIP), dissolved organic phosphorus (DOP) and particle organic phosphorus (POP), whose concentrations are denoted as DIP, DOP and POP (mmol/m^3). The biological production converts most DIP into POP directly, while a small portion σ goes to DOP pool before remineralizing back into phosphate at a constant rate. The remaining production $1 - \sigma$ is allocated to sinking POP. The advective-diffusive transport of dissolved tracers is computed using annual transport operators which include the information of climate-driven varying circulation. The particulate tracer POP is only transported vertically.

The governing equation for phosphorus tracers is:

$$\frac{d}{dt}\begin{bmatrix} DIP \\ POP \\ DOP \end{bmatrix} + \begin{bmatrix} \boldsymbol{T}(t) + L(\boldsymbol{r}) + k_g I & 0 & k_d I \\ -(1-\sigma)L & S + k_p I & 0 \\ -\sigma L & -k_p I & \boldsymbol{T}(t) + k_d I \end{bmatrix} \begin{bmatrix} DIP \\ POP \\ DOP \end{bmatrix} = \begin{bmatrix} k_g \overline{DIP} \\ POP \\ DOP \end{bmatrix} \qquad (2)$$

where $L(\boldsymbol{r})$ is the spatially varying rate for the biological uptake rate of phosphate (defined in equation (1)). The resulting spatial variations in the value of $L(\boldsymbol{r})$ parameterize differences in biological production due to light density, grazing pressure, and the availability of nutrients other than phosphate. Note that $L(\boldsymbol{r})$ is identically equal to zero in the aphotic zone (i.e., deeper than 100m). $\boldsymbol{T}(t) \equiv \nabla \cdot [\boldsymbol{\mu}(t) - \boldsymbol{\kappa}(t) \cdot \nabla]$ is the advection-diffusion transport operator subject to no-flux boundary conditions at the surface and on the basin boundaries, and $S \equiv \nabla \cdot (\vec{w}[\mathrm{POP}])$ is a divergence operator representing the vertical transport of POP. $\vec{w}$ is the sinking speed of POP and is directed downward. $\vec{w}$ increases linearly with depth. The dissolution rate k_p is a vertically fixed constant so that the attenuation of the vertical flux of POP follows a powerlaw function, $F(z) = F(z_0)(z/z_0)^{-b}$, where $F(z)$ and $F(z_0)$ are fluxes at a depth of z and z_0, respectively. Here b is a constant and does not vary with temperature. The phosphorus model is solved forwardly from its preindustrial state, which is determined as the DIP, POP and DOP field solved from the steady-state version of equation (2).

$$\begin{bmatrix} \boldsymbol{T}(1850) + L(\boldsymbol{r}) + k_g I & 0 & k_d I \\ -(1-\sigma)L & S + k_p I & 0 \\ -\sigma L & -k_p I & \boldsymbol{T}(1850) + k_d I \end{bmatrix} \begin{bmatrix} DIP \\ POP \\ DOP \end{bmatrix} = \begin{bmatrix} k_g \overline{DIP} \\ POP \\ DOP \end{bmatrix} \qquad (3)$$

2.2.2 Carbon model

At each time step, the carbon cycling model is solved subsequently from the phosphorus model. In the carbon model, we consider five pools of carbon: dissolved inorganic carbon (DIC), dissolved organic carbon (DOC), particulate organic carbon (POC), particulate inorganic carbon (PIC) and alkalinity (ALK). The DIP assimilation rate (γ[DIP]) is denoted using **G** for simplicity and is converted to DIC assimilation rate by multiplying a C:P ratio ($r_{\mathrm{C:P}}$) that is allowed to vary spatially according to the modelled DIP concentration, $r_{\mathrm{C:P}} = (cc[\mathrm{DIP}] + dd)^{-1}$, where cc and dd are estimated as part of the optimization. The fraction, σ, of the organic carbon production allocated to POC and DOC pools is estimated as part of the inversion and does not need to be the same as the fraction σ_P allocated to the POP and DOP pools. The downward transport of POC is modeled using a flux divergence operator ($\mathbf{S}_{\mathrm{POC}}$), which is formulated in the same way as the POP sinking flux-divergence operator, $\mathbf{S}_{\mathrm{POP}}$, with independent adjustable parameters $b_{C\theta}$ and b_C that are determined as part of the inversion (**Table 1**). Unlike DIP, DIC is also subject to sea-to-air CO_2 exchange at the surface. This gas exchange is modeled according to the method used for phase 2 of the Ocean Carbon-Cycle Model Intercomparison Project (OCMIP-2). In addition, freshwater precipitation and evaporation can significantly impact surface ocean DIC and ALK concentrations. Precipitation will dilute, while evaporation will concentrate their concentrations. A virtual flux according to OCMIP-2 is applied to model for the effects of precipitation and evaporation on DIC and ALK ($\boldsymbol{F}_{vDIC}[\mathrm{DIC}]_s$ and $\boldsymbol{F}_{vALK}[\mathrm{ALK}]_s$, where $[\mathrm{DIC}]_s$ and $[\mathrm{ALK}]_s$ are the mean surface-ocean concentrations of DIC and ALK, respectively). Production of PIC is modeled to be proportional to the production of POC using two adjustable parameters r_{Si} and r_{RR} that are estimated by the optimization. The parameter r_{Si}

adjusts PIC production according to silicate concentration in the surface ocean in linear form ($R_{RR} = r_{Si}[\mathrm{SiO}_4^{3-}] + r_{RR}$).

The downward transport of PIC is modeled using a flux divergence operator ($\mathbf{F}_{\mathrm{PIC}}$), which generates a PIC flux profile that follows an exponential function $\mathbf{F}_{\mathrm{PIC}}(z) = F_0 \exp\left((z - z_0)/d\right)$, where d is PIC dissolution length scale whose value is estimated as part of the optimization (**Table 1**). Every mole of PIC production consumes two moles of ALK. In contrast, the dissolution of one mole of PIC releases two mols of ALK. From the perspective of carbon, photosynthesis and remineralization of organic matter do not change alkalinity. However, in photosynthesis and demineralization, chemical forms of nitrogen change, which influences alkalinity so that a mole of organic carbon production increases alkalinity by $r_{\mathrm{N:C}}$ moles, while a mole of organic carbon remineralization decreases alkalinity by $r_{\mathrm{N:C}}$ moles. The governing equation for carbon tracers is:

$$\frac{d}{dt}\begin{bmatrix} DIC \\ POC \\ DOC \\ PIC \\ ALK \end{bmatrix} + \begin{bmatrix} \boldsymbol{T}(t) - J_g & 0 & -k_d I & -k_p I & 0 \\ 0 & S - k_p I & 0 & 0 & 0 \\ 0 & -k_p I & T - k_d & 0 & 0 \\ 0 & 0 & 0 & S + k_p I & 0 \\ 0 & 0 & 0 & -2k_p I & \boldsymbol{T}(t) + k_g I \end{bmatrix} \begin{bmatrix} DIC \\ POC \\ DOC \\ PIC \\ ALK \end{bmatrix} =$$

$$\begin{bmatrix} -(I + (1 - \sigma)R)(G \cdot r_{C:P}) + \mathbf{F}_{v\mathrm{DIC}}[\mathrm{DIC}]_s \\ (1 - \sigma)(G \cdot r_{C:P}) \\ \sigma G \cdot r_{C:P} \\ R \cdot G \cdot r_{C:P} \\ k_g \overline{ALK} - \mathbf{F}_{vALK}[\mathrm{ALK}]_s \end{bmatrix} \quad (4)$$

Similarly, the carbon model is also solved forwardly and its initial condition is the steady-state solution of equation (5).

$$\begin{bmatrix} \boldsymbol{T}(1850) - J_g & 0 & -k_d I & -k_p I & 0 \\ 0 & S - k_p I & 0 & 0 & 0 \\ 0 & -k_p I & T - k_d & 0 & 0 \\ 0 & 0 & 0 & S + k_p I & 0 \\ 0 & 0 & 0 & -2k_p I & \boldsymbol{T}(1850) + k_g I \end{bmatrix} \begin{bmatrix} DIC \\ POC \\ DOC \\ PIC \\ ALK \end{bmatrix} = \begin{bmatrix} -(1+r)G \\ (1-\sigma)G \\ \sigma G \\ rG \\ k_g \overline{ALK} \end{bmatrix} \quad (5)$$

The values of all parameters in the phosphorus and carbon model are listed in **Table 4.1**.

Table 4.1. The optimal model parameters. The definitions of the parameters are presented in the Methods section.

Parameters	Values	Units
σ	1.2954×10^{-14}	Unitless
Q_{10P}	2.3433	Unitless
k_dP	3.4422×10^{-8}	s^{-1}
bP_T	1.1347	Unitless
bP	0.1419	Unitless
α	9.1742×10^{-8}	s^{-1}
β	0.1193	Unitless
bC_T	1.4151	Unitless
bC	0.0023	Unitless
d	4280	m
Q_{10C}	1.4560	Unitless
kdC	6.2877×10^{-8}	s^{-1}
r_{Si}	0.1627	L μM^{-1}
r_{RR}	0.0180	Unitless
cc	1.7075×10^{-4}	L μM^{-1}
dd	0.0056	Unitless

2.3 Sensitivity Experiments

To investigate the relative contribution of individual mechanisms to the global ocean carbon sink and its natural and anthropogenic components, two groups of sensitivity experiments were conducted (**Table 4.2**). Group A is designed to explore the role of each mechanism in the natural carbon cycle, with atmospheric CO_2 concentration held constant at preindustrial values. Experiment A1 serves as the control experiment, with all variables set to preindustrial values. Experiment A2 examines the effects of varying circulation, with the difference between A2 and A1 representing the role of circulation changes in the natural carbon cycle. The experiment A3 quantifies the role of varying biology, with the difference between A3 and A2 representing the impact of varying biological processes on natural carbon uptake. The experiment A4 evaluates the role of increasing sea surface temperature in natural carbon uptake, with the difference between A4 and A3 reflecting the impact of temperature on the natural carbon cycle. Finally, the experiment A5 is a full natural carbon run, with the difference between A5 and A4 representing the role of varying air-sea CO_2 exchange rate on natural carbon uptake.

Group B focuses on understanding the role of individual mechanisms in the total ocean carbon sink, with atmospheric CO_2 concentrations following the prescribed trajectories under the RCP8.5-ECP8.5 climate scenario. The difference between experiment B1 and A1 examines the effects of rising atmospheric CO_2, but with no radiative feedback in the model. The experiment B2 allows ocean circulation to change with time, with the difference between B2 and B1 representing the role of changing circulation in total ocean carbon uptake. The experiment B3 quantifies the impact of varying biology on total ocean carbon uptake, with the difference between B3 and B2 representing the role of biological processes in the total carbon sink. The experiment B4 assesses the impact of increasing sea surface temperature on total ocean carbon uptake, with the difference between B4 and B3 reflecting the role of temperature in the total carbon sink. Finally, the experiment B5 is a full climate run, with the difference between B5 and B4 representing the role of wind speed driven changes of air-sea CO_2 exchange rate in the total carbon sink.

Table 4.2. The configuration of sensitivity tests. The mark "√" means this variable changes with climate warming, and "×" means it is fixed at the levels of preindustrial times.

	Experiments	**pCO$_2$atm**	**Circulation**	**Biology**	**SST**	**Piston velocity**
A1	Control	×	×	×	×	×
A2	Circulation	×	√	×	×	×
A3	Circulation and biology	×	√	√	×	×
A4	Circulation, biology and SST	×	√	√	√	×
A5	Full nat	×	√	√	√	√
B1	pCO$_2$atm	√	×	×	×	×
B2	pCO$_2$atm and circulation	√	√	×	×	×
B3	pCO$_2$atm, circulation and biology	√	√	√	×	×
B4	pCO$_2$atm, circulation, biology and SST	√	√	√	√	×
B5	Full climate	√	√	√	√	√

3. Results

3.1 Ocean carbon uptake from the BGC model

Fig. 4.1 shows global maps of air-sea CO_2 flux and its natural and anthropogenic components from the preindustrial to year 2300. The contemporary global air-sea flux pattern is comparable to that of corresponding simulations in other Coupled Model Intercomparison Project6 (CMIP6) models and reconstructions from the observational pCO_2 dataset (Fig. 4.1A) (Landschutzer et al., 2014; Takahashi et al., 2009; Gloege et al., 2021). The equatorial upwelling zone acts as a natural carbon source to the atmosphere, while the North Atlantic serves as a significant carbon sink (Fig. 4.1D). However, there are some discrepancies between our model and observational-based CO_2 flux estimates in the Southern Ocean, where our model predicts a carbon sink, whereas observational data indicate a weak carbon source. This inconsistency could stem from the coarse resolution of our model, which inadequately represents the Southern Ocean's westerly winds and deep convection.

As anthropogenic CO_2 emissions increase, the globally integrated air-sea CO_2 flux gradually rises, indicating that the ocean absorbs more CO_2 from the atmosphere until about the year 2100. At the end of the twenty-first century, the global air-sea CO_2 flux reaches the maximum of approximately 5.5 PgC/yr, consistent with previous estimates from earth system models (Randerson et al., 2015). After the year 2100, the ocean continues to serve as a significant carbon sink, but it absorbs less CO_2 from the atmosphere. This is due to decreasing CO_2 emissions (Fig. 4.2), as previous studies have demonstrated that the ocean's ability to sequester carbon is dependent on CO_2 emission trajectories (McKinley et al., 2023).

Nevertheless, not all the changes in the carbon sink can be attributed to extra human-induced carbon emissions, as the natural carbon cycle also plays a crucial role in regulating the ocean carbon sink. Fig. 4.1 illustrates that the outgassing of natural carbon, especially in the Southern Ocean, intensifies with warming, resulting in reduced natural carbon storage in the ocean. This is balanced by strong uptake of anthrophonic CO2 (Fig. 4.1).

In a sum, the rising atmospheric CO_2 is the primary driver of the ocean carbon sink, and the ocean's capacity to sequester carbon from the atmosphere follows carbon emission trajectories. In a warming world, natural carbon outgassing intensifies, but this is more than offset by the large uptake of anthropogenic CO_2.

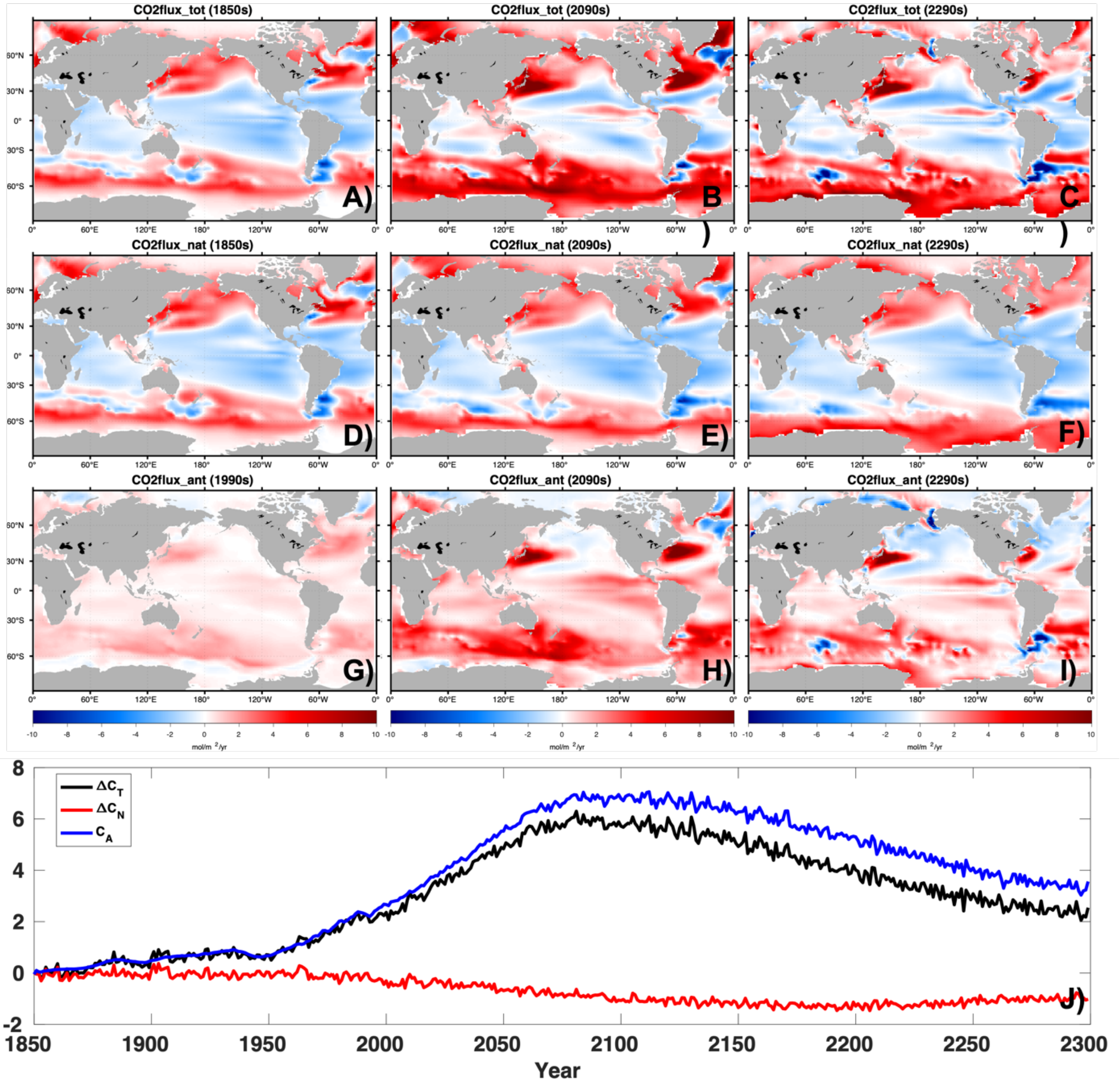

Figure 4.1. Global map and time series of air-sea CO_2 flux. Panels A-C, D-F, and G-I show the global distribution of the total, natural, and anthropogenic components of the air-sea CO_2 flux for the decades of 1990 (A, D, G), 2090 (B, E, H), and 2290 (C, F, I), respectively (unit: mol/m^2/yr). Panel G shows the time series of air-sea CO_2 flux for total carbon (black line), natural carbon (red line), and anthropogenic carbon (blue line) (unit: PgC/yr).

3.2 Multicentury changes of physical and biological variables

Various factors affect the air-sea CO_2 flux, including atmospheric CO_2 concentration, sea surface temperature, ocean circulation, and the exchange rate between the ocean surface and the atmosphere. The prescribed atmospheric CO_2 concentration rises from 284 ppm in the preindustrial era to 1960 ppm in the 2250s under the business-as-usual warming scenario (i.e., RCP8.5-ECP8.5) and then stabilizes (Fig. 4.2A). The atmospheric CO_2 increases faster before 2100 and more slowly after that (Fig. 4.2B), consistent with the trajectories of carbon emission rates.

A warming and more stratified ocean causes the global overturning circulation to slow down from preindustrial to year 2300. By year 2300, the Atlantic Meridional Overturning Circulation (AMOC) weakens to only 5 Sv, and the Southern Ocean Meridional Overturning Circulation (SMOC) completely shuts down (Fig. 4.2C-4.2E). Most of the changes occur after the year 2100, emphasizing the need to extend the study to the year 2300 (Moore et al., 2018). The sea surface temperature continues to rise, but the magnitude of the increase varies across the global ocean. The mean atmospheric surface temperature increase in 2300 is approximately 9.6°C higher than preindustrial levels. Warming surface waters reduce the solubility of CO_2 in seawater (Fig. 4.2F-4.2H, Moore et al., 2018). Global wind patterns also shift significantly in a warming climate. The Southern Ocean westerly winds intensify and move southward, with the potential to impact the natural carbon cycle and the air-sea CO_2 exchange rates.

In summary, multiple factors influence the air-sea CO_2 flux, including atmospheric CO_2 concentration, sea surface temperature, ocean circulation, and exchange rate between the ocean surface and the atmosphere. These variable factors interact with each other, resulting in changes in the air-sea CO_2 flux. It is essential to understand these changes and how they affect the ocean carbon sink to predict the future global carbon cycle and its impacts on climate.

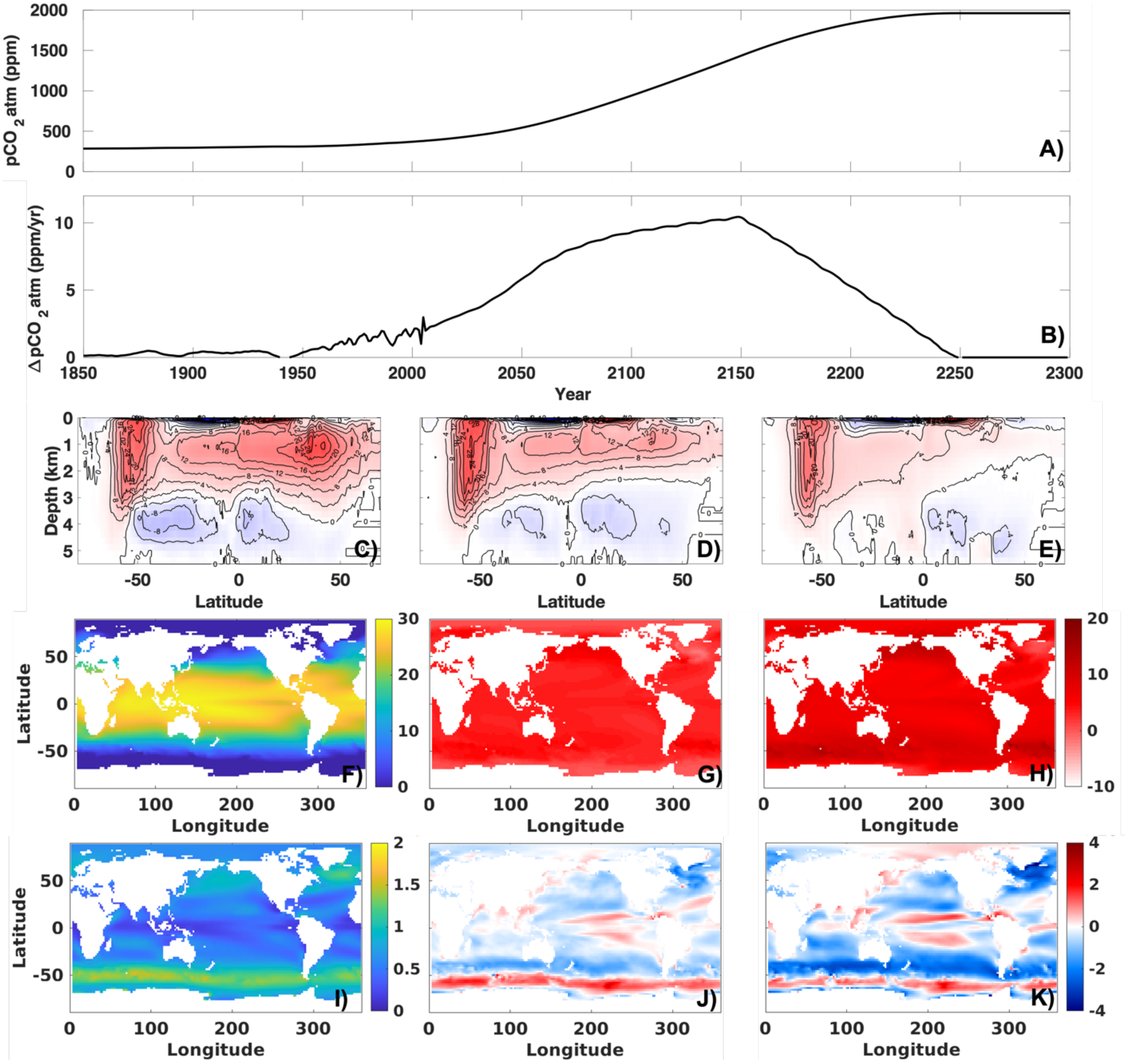

Figure 4.2. Global annual mean diagnostics from CESMv1. Panels A and B display the atmospheric pCO_2 (unit: ppm) and its annual increase (unit: ppm/yr) from 1850 to 2300 under the RCP8.5-ECP8.5 scenario. The third row shows the streamfunction: C) for the decade of 1850, D) the difference between 2090 and 1850, and E) the difference between 2290 and 1850 (unit: Sv). The fourth row displays sea surface temperature (SST), F) for the decade of 1850, G) the difference between 2090 and 1850, and H) the difference between 2290 and 1850 (unit: ^{o}C). The final row presents the piston velocity, I) for the decade of 1850, J) the difference between 2090 and 1850, and K) the difference between 2290 and 1850 (unit: $x10^{-4}$ m/s).

Understanding the Impact of Individual Mechanisms on Air-Sea CO_2 Flux

Ocean processes play a crucial role in regulating the ocean carbon sink by influencing both the natural and anthropogenic carbon cycles. In this section, we delve into the mechanisms that control the total ocean carbon sink and its natural and anthropogenic components.

Fig. 4.3 shows the time series of total carbon fluxes at the sea surface, including anthropogenic and natural contributions. The ocean's capacity to absorb carbon from the atmosphere peaks at approximately 5.5 PgC/yr by 2100 and gradually declines thereafter (Fig. 4.3A). This decline is mainly attributed to reduced CO_2 emissions into the atmosphere (Fig. 4.2B). In the absence of radiative feedback, the ocean sequesters a maximum of approximately 8 PgC/yr carbon till 2100 and subsequently decreases to 4.5 PgC/yr in 2300 (Fig. 4.3A, black line). However, when all feedbacks are included, the ocean carbon sink peaks at 5.5 PgC/yr in 2100 (Fig. 4.3A, pink line). This indicates that climate-driven changes in ocean processes will lead to a reduction of approximately 2.5 PgC/yr in carbon uptake from the atmosphere by 2100. Integrating until 2300, the climate-driven changes in ocean processes will result in about 750 PgC less stored in the ocean, which is equivalent to an extra 360 ppm increase in atmospheric CO_2 (Fig. 4.3B).

We further investigate the impacts of each individual mechanism on air-sea CO_2 uptake from the preindustrial era to 2300. The negligible difference between the black and red lines in Fig. 4.3A indicates that circulation changes alone do not have a significant effect on the ocean carbon sink. However, considering the biological processes that vary with circulation, especially including the declining export production in the ocean, will reduce the ocean carbon sink and result in an extra 280 ppm increase in atmospheric CO_2 concentration from preindustrial to year 2300. This finding aligns with the CMIP6 analysis that slowing overturning circulation reduces the total ocean carbon sink (Liu et al., 2023). An important advancement from previous studies is the realization that circulation changes alone do not significantly alter the ocean carbon sink, but the declining biological production (driven by the circulation slowdown) drives reductions the total carbon sink, by increasing surface CO_2 concentrations. Additionally, increasing sea surface temperatures reduce the solubility of CO_2 in seawater, leading to a further decrease in the ocean carbon sink, resulting in an accumulation of an extra 96 ppm increase in atmospheric CO_2 from preindustrial to 2300. Conversely, changes in piston velocity do not significantly affect the global carbon sink, despite the strengthening of Southern Ocean westerly winds in a warming world (Russell et al., 2006).

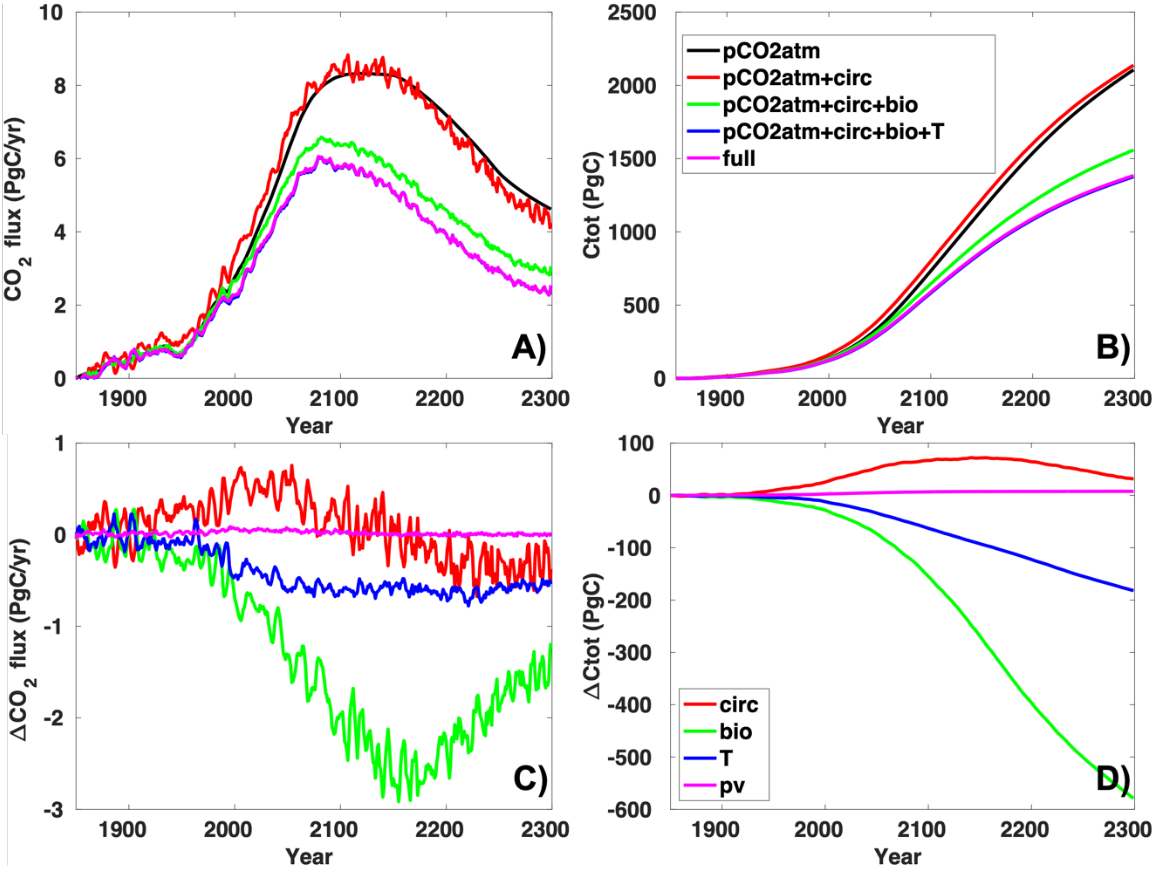

Figure 4.3. The effects of climate-driven varying circulation, biology, sea surface temperature and piston velocity on air-sea CO_2 flux and total carbon uptake. The air-sea CO_2 flux (unit: PgC/yr) and integrated DIC accumulation (unit: PgC) are shown in panels A) and B). The black, red, green, blue and meganta line represent the simulation with increasing atmospheric CO_2 (Exp B1), increasing atmospheric CO_2 and time-evolving circulation (Exp B2), increasing atmospheric CO_2, time-evolving circulation and changing biology (Exp B3), increasing atmospheric CO_2, time-evolving circulation, changing biology and rising SST (Exp B4) and full climate run (B5). The effects of each ocean processes on air-sea CO_2 flux are shown in panel C) and D). The red, green, blue and meganta lines represent the effect of time-evolving circulation, changing biology, SST and piston velocity, respectively.

3.4 Impacts of Individual Mechanisms on Natural and Anthropogenic Carbon

The assumption that anthropogenic carbon emissions solely contribute to the ocean's total carbon sink ignores the impact of natural carbon cycle changes (Holzer and DeVries, 2022) By holding atmospheric CO_2 constant at 280 ppm from 1850 to 2300 and allowing ocean processes to respond to climate warming, evidence shows that the ocean gradually becomes a carbon source to the atmosphere, leading to an accumulative outgassing of 320 PgC from the ocean to the atmosphere, equivalent to a 154 ppm increase in atmospheric CO_2 concentration. This carbon outgassing is consistent with results from other earth system models (Fu et al., 2022).

As climate warms, the ocean's evolving circulation patterns enhance its capacity to store natural carbon, resulting in increased carbon uptake by 500 PgC, equivalent to a 240 ppm decrease in atmospheric CO_2 concentration. However, when factoring in changes in ocean biology or the decrease in export productivity driven by circulation changes, the ocean becomes a modest natural carbon source. While stronger winds induced by climate warming increase natural carbon outgassing in the Southern Ocean due to stronger upwelling of carbon-rich water (Le Quere et al., 2007), the impact of slowing overturning circulation on deep ocean carbon storage offsets this effect. Additionally, rising sea surface temperatures lead to a gradual outgassing of natural carbon, resulting in approximately 300 PgC outgassed from preindustrial times to 2300, equivalent to an extra 144 ppm increase in atmospheric CO_2 (Fig. 4.4).

As expected from conservation, the uptake of anthropogenic carbon from the atmosphere is precisely the same amount as the sum of total ocean carbon uptake and the outgassed natural carbon. As the time-evolving circulation alone has a minimal effect on total ocean carbon sink (Fig. 4.3) and sequesters more natural carbon in the ocean, it is supposed to have a negative effect on the uptake of anthropogenic carbon. In the next section, we will go into further details on how ocean circulation separately affects natural and anthropogenic carbon storage.

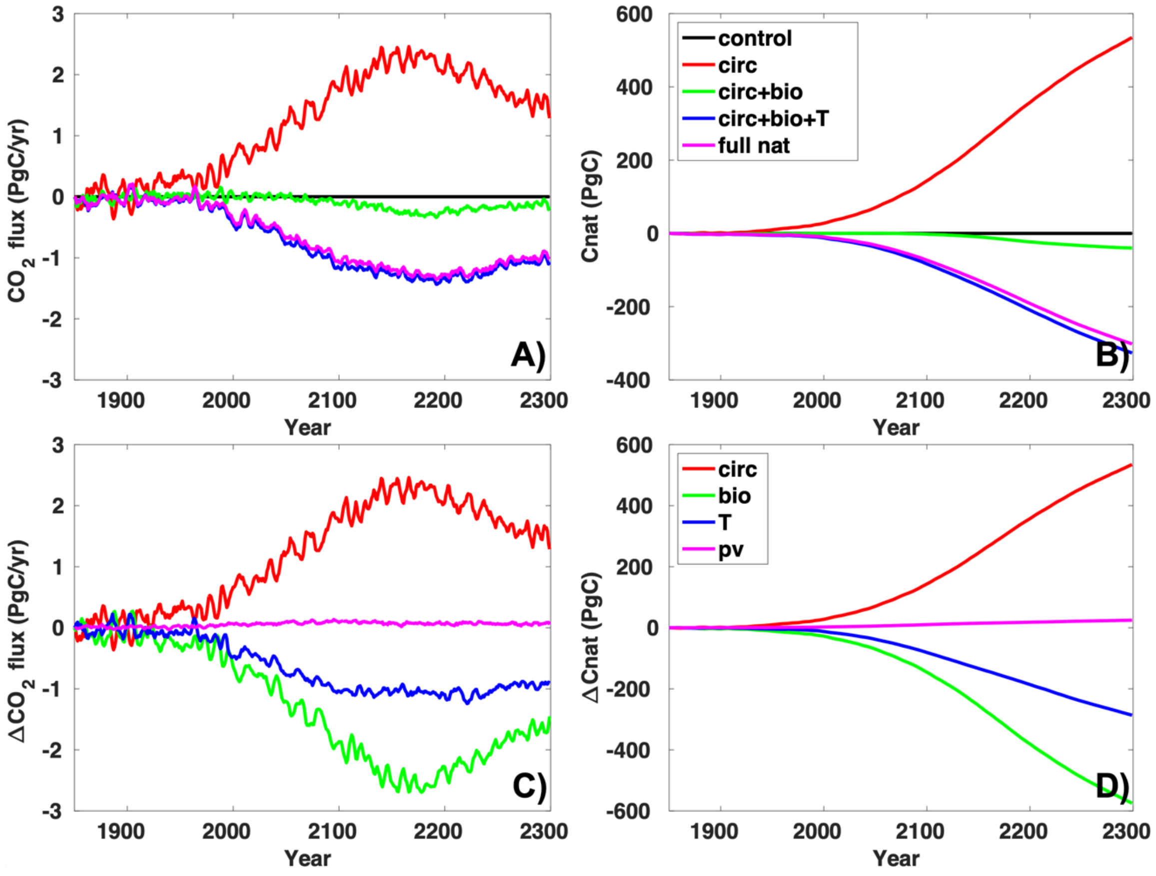

Figure 4.4. The effects of climate-driven varying circulation, biology, sea surface temperature and piston velocity on air-sea CO_2 flux and natural carbon storage. The air-sea CO_2 flux (unit: PgC/yr) and integrated DIC accumulation (unit: PgC) are shown in panels A) and B). The black, red, green, blue and meganta line represent the simulation with increasing atmospheric CO_2 (Exp B1), increasing atmospheric CO_2 and time-evolving circulation (Exp B2), increasing atmospheric CO_2, time-evolving circulation and changing biology (Exp B3), increasing atmospheric CO_2, time-evolving circulation, changing biology and rising SST (Exp B4) and full climate run (B5). The effects of each ocean processes on air-sea CO_2 flux are shown in panel C) and D). The red, green, blue and meganta lines represent the effect of time-evolving circulation, changing biology, SST and piston velocity, respectively.

4.5 The Impacts of Varying Ocean Circulation on the Ocean Carbon Sink

As discussed above, ocean circulation plays a crucial role in redistributing carbon, adjusting the distribution of dissolved inorganic carbon (DIC), and influencing the ocean's ability to absorb atmospheric CO_2. Two notable features emerge in the changes of ocean circulation as climate warms: First, the Southern Ocean upwelling intensifies as westerly winds strengthen (Russell et al., 2006; Moore et al., 2018); and second, the deep ocean overturning circulation weakens over time (Liu et al., 2023). We examine the global average DIC vertical profile to explore how time-evolving ocean circulation and its driving changes in biological export production affect the ocean carbon sink, including its natural and anthropogenic components, focusing on the decades of 2090 and 2290 (**Fig. 4.5**).

By the decade of 2090, we can see the reduced surface DIC but increased carbon sequestration in the deep ocean without factoring in the effect of the changing biological processes (black solid line in **Fig. 4.5A**). This vertical profile of total DIC includes both natural and anthropogenic components, with natural carbon closely mirroring the total carbon. The slowing overturning circulation separates the upper and deep ocean, slowing the vertical exchange of carbon and leading to less carbon in the upper ocean and more in the deep ocean (Moore et al., 2018). This effect is further supported by the longer carbon sequestration time, allowing deep ocean carbon to remain longer before returning to the surface. As a result, natural carbon storage in the deep ocean increases (red solid line in **Fig. 4.5A**). In contrast, the overturning circulation negatively impacts the uptake of anthropogenic carbon. A slower overturning circulation, compared to a constant one, leads to reduced anthropogenic carbon absorption from the atmosphere. This is because the slowing overturning circulation hinders the transport of anthropogenic carbon from the surface ocean to the deep ocean, consequently limiting further carbon uptake from the atmosphere (blue solid line in **Fig. 4.5A**). By the decade of 2290, anthropogenic carbon accumulates more at thermocline depths rather than at the surface (blue solid line in **Fig. 4.5B**). This is due to the vertical transport of excess anthropogenic carbon from the surface to the thermocline depths.

Taking into account both the effects of the evolving circulation and the decrease in biological export production, the ocean's total carbon absorption capacity is observed to be lower compared to a scenario with constant biological processes (as represented by the black dashed and solid lines in **Fig. 4.5A**). By 2090, the vertical profile of the impacts on total carbon follows the shape of natural carbon, which accumulates more in the deep ocean despite the decline in biological export production (red dashed and solid lines in **Fig. 4.5A**). This is because the longer sequestration time of natural carbon overcompensates for the decreased export production. In this context, anthropogenic carbon accumulation also experiences a shift with more concentration in the upper ocean and less at greater depths. In contrast to the DIC profile that does not consider decreases in biological export production, the upper ocean accumulates less anthropogenic carbon, as the increase in natural DIC decreases the ocean's buffering capacity to absorb anthropogenic carbon from the atmosphere (as demonstrated by the blue and red dashed and solid lines in **Fig. 4.5A**). By the decade of 2290, the effects of the changing circulation and biological export production on the vertical carbon distribution become more pronounced compared to the decade of 2090 (as seen in the black and red dashed and solid lines in **Fig. 4.5B**). Conversely, the impacts on anthropogenic carbon uptake seem to become less significant compared to the decade of 2090 (blue dashed and solid lines in **Fig. 4.5B**). This might be attributed to the saturation of the surface ocean and the consequent reduction in buffering capacity, leading to negligible changes in DIC due to the decrease in biological export production.

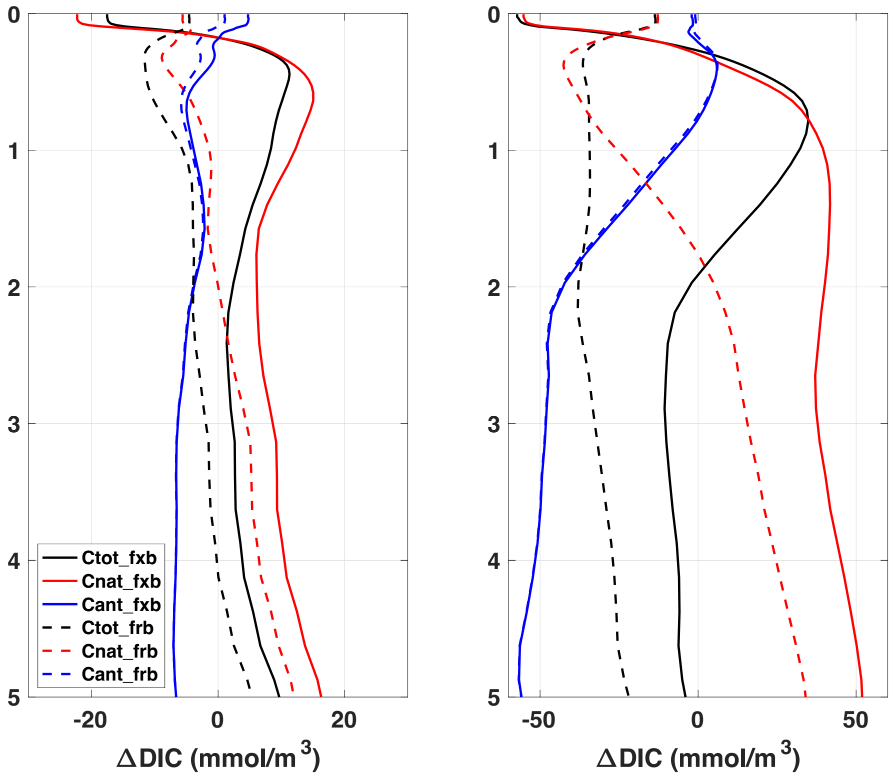

Figure 4.5. The impacts of time-evolving circulation and biological processes on DIC vertical profiles. Panels A) and B) represent the differences in DIC vertical profiles between time-evolving circulation (Exp A2, B2) and constant circulation (Exp A1, B1) in the decades of A) 2090 and B) 2290, respectively. The solid and dash lines represent the impacts of time-evolving circulation on the vertical DIC profiles without and with changes in biological processes. The black, red, and blue lines correspond to total DIC (Exp B2 - Exp B1), natural DIC (Exp A2 – Exp A1), and anthropogenic DIC (Exp B2 – Exp B1 – (Exp A2 – Exp A1)), respectively (unit: mmol/m^3).

In sum, the slowdown of overturning circulation leads to increased natural carbon sequestration in the deep ocean, while simultaneously reducing the ocean's capacity to absorb excess anthropogenic carbon from the atmosphere. The net effect is a reduction in the ocean carbon sink, particularly under a business-as-usual warming scenario.

4. Summary and Discussion

In this study, we integrated annual transport operators into an inverse biogeochemical model with phosphorus and carbon cycles to investigate the role of each ocean process in the ocean carbon sink and its natural and anthropogenic components from 1850 to 2300. We conducted two groups of sensitivity experiments: group A, focusing on the natural carbon cycle with constant atmospheric CO_2 concentration over the industrial period, and group B, focusing on the total ocean carbon sink with atmospheric CO_2 concentration following the RCP8.5-ECP8.5 climate scenario trajectories. To the best of our knowledge, this is the first study to quantify and analyze the role of each ocean mechanism in the ocean carbon sink and its natural and anthropogenic components. It is also the first time time-evolving transport operators have applied in an inverse biogeochemical model, providing a convenient tool to further disentangle the role of individual ocean processes on carbon and other biogeochemical cycles.

Under the business-as-usual warming scenario, the global ocean carbon sink peaks at about 5.5 PgC/yr in 2100 and decreases afterward, mainly due to reduced CO_2 emissions into the atmosphere (Meinshausen et al., 2011). Without considering radiative feedback, the oceans can take up to 8 PgC/yr in 2100, which means, when accounting for the ocean's net response to climate warming, there could be approximately 336 ppm increase in atmospheric CO_2 concentration from preindustrial times to the year 2300 by this negative feedback.

The primary driver of the ocean carbon sink is atmospheric CO_2, which directly affects the pCO_2 gradient between the atmosphere and the sea surface. Ocean circulation, believed to be the secondary driver, influences the ocean's capacity to absorb excess anthropogenic carbon from the atmosphere. Slowing overturning circulation reduces this capacity, potentially leading to a 280 ppm increase in atmospheric CO_2 when the effect on biology is factored in. Rising temperatures negatively impact the ocean carbon sink by reducing CO_2 solubility at the sea surface, leading to an extra 96 ppm increase in atmospheric CO_2 from 1850 to 2300. Although global wind patterns change over time, their effect on the ocean carbon sink through piston velocity canceled out regionally and is minimal.

Our study confirms gradual natural carbon outgassing as the climate warms (Fu et al., 2022; Holzer and DeVries, 2022). Ocean circulation alone sequesters more natural carbon in the deep ocean, making it a larger carbon reservoir despite increased outgassing in the Southern Ocean. However, when accounting for decreasing biological export production driven by slowing overturning circulation, this effect becomes minimal, resulting in the dominant role of increasing sea surface temperature (SST) in shaping natural carbon outgassing by decreasing CO_2 solubility at the surface.

Since the role of time-evolving ocean circulation on the ocean carbon sink is complex, we further decomposed its effects on the natural, anthropogenic, and total ocean carbon sinks. Our results show that stronger Southern Ocean upwelling leads to more natural carbon outgassing, but slowing overturning circulation tends to sequester more natural carbon in the deep ocean. However, slowing overturning circulation forces anthropogenic carbon to accumulate at the surface, decreasing the ocean's capacity to absorb more anthropogenic carbon from the atmosphere. The net effect of time-evolving circulation is to reduce the ocean carbon sink by affecting biological export production and surface DIC.

The detailed quantification of time-evolving ocean circulation on the ocean carbon sink improves our understanding of the role of ocean physics in modulating the global carbon cycle and climate. This could also be helpful to quantify the sources of a large spread of the contemporary and future ocean carbon sink in CMIP6 models (Fay and McKinley, 2021; Liu et al., 2023; McKinley et al., 2023). It also informs the estimation of the efficacy of ocean carbon dioxide removal (CDR) strategies, which typically assume that ocean circulation is in a steady state and will not change with climate (Siegel et al., 2021). Our study emphasizes the importance of the transient nature of ocean circulation on the global carbon cycle and its potential effects on the efficacy of ocean CDR strategies.

However, there are caveats to our study. The transport operator is derived from CESMv1 circulation, which significantly underestimates the strength of the SMOC (Liu et al., 2023). We also neglect the seasonal variability of circulation, which may introduce uncertainties in its effect on the ocean carbon cycle. The coarse resolution of our model may cause uncertainties in understanding local and regional effects of changing ocean circulation. Additionally, our biogeochemical model has fixed stoichiometry with time, potentially causing uncertainties in estimating ocean biological productivities and impacts on the ocean carbon sink (e.g., Wiseman et al., 2023; Kwon et al., 2022).

Future work should consider more moderate climate scenarios and focus on prognostic atmospheric CO_2 simulations, which are more realistic and allow for better diagnosis of climate impacts on ocean circulation and the global carbon budget.

Chapter 5: Conclusions and Future Work

There are significant uncertainties in the estimation of the future ocean carbon sink. While the spread in modern air-sea CO_2 fluxes can account for approximately 50% of these uncertainties, the impact of future ocean circulation changes, as well as the role of other ocean processes cannot be overlooked. In this dissertation, I utilized CMIP6 Earth System Models, an offline model with annual transport operators, and an inverse biogeochemical model to investigate the role of slowing overturning circulation, as well as other ocean processes, on the future ocean carbon sink. Additionally, I quantified its impact on ventilation timescales and patterns and discussed its potential impacts on the durability of certain marine CDR strategies which focus on sequestering carbon in the deep ocean.

The overturning circulation, including both upper and abyssal cells, slows as the climate warms. The magnitude of this slowdown depends on the warming scenarios, with greater slowdowns under high-end climate scenarios and less under more moderate ones. Notably, the SMOC nearly fully shuts down by 2300 under a business-as-usual scenario. The SMOC slowdown increases carbon sequestration by the biological pump, as it prolongs ocean carbon sequestration before releasing it back into the atmosphere. Although biological export productivity declines due to nutrient trapping in the deep ocean, this effect is overcompensated by longer sequestration times driven by slowing overturning circulation. Conversely, the slowing overturning circulation weakens the solubility pump, primarily by preventing anthropogenic carbon transport into the deep ocean, accumulating anthropogenic carbon at the sea surface and further limiting ocean surface CO_2 uptake. The net effect of slowing overturning circulation is a reduced ocean carbon sink until 2100 across multiple climate warming scenarios.

Through a series of sensitivity experiments, we investigated the role of time-evolving ocean circulation on carbon sinks, focusing separately on the natural carbon cycle and anthropogenic carbon uptake. As the climate warms, natural carbon outgassing occurs due to reduced ocean surface CO_2 solubility. Slowing overturning circulation increases natural carbon sequestration but, when combined with decreased export production, its effect on natural carbon is negligible. Slowing overturning circulation has little impact on anthropogenic carbon uptake but, when combined with declining export production, its effect on anthropogenic carbon uptake is negative. Temperature increases play a secondary role in affecting the ocean carbon sink. This study quantifies the role of individual ocean processes on both natural and anthropogenic carbon uptake.

Furthermore, slowing overturning circulation affects ocean ventilation timescales and patterns. The water mean age increases by approximately 110 years from 1850 to 2300. The impact on mean first-passage time remains uncertain, as it depends on future ocean circulation after year 2300. We consider two future circulation scenarios: persistent post-2300 circulation (scenario 1) and an abrupt return to year-1850 states (scenario 2). The mean first-passage time at the year 1850 is almost twice in scenario 1 than scenario 2. The global-averaged mean first-passage time increases over time in scenario 1 but decreases in scenario 2. However, if we are interested in the impact of slowing overturning circulation on the potential durability of ocean CDR strategies within the next 100 or 200 years, the post-2300 circulation is not a factor.

Looking ahead, the trajectory of future research should focus on two main aspects. First, there is a need for a more comprehensive representation of global ocean overturning circulation, particularly including the dynamic influence of ice sheets. Ice sheet dynamics, primarily their melting rates and contributions to freshwater input, could have significant impacts on oceanic biogeochemical cycles, especially the carbon cycle. A study by Swingedouw et al. (2021) has shown that meltwater from the Greenland ice sheet can influence AMOC strength. Fu et al. (2020) demonstrated that the growing freshwater lens in the Arctic Ocean will disrupt ecosystem function in the North Atlantic. Li et al., (2023) also argued the important role of ice sheet meltwater inputs in modulating the strength of SMOC. The iron inputs from the meltwater could affect biological productivity, particularly phytoplankton blooms, thereby increasing carbon sequestration (Moore et al., 2018). Consequently, a more realistic representation of meridional overturning circulation with ice sheet dynamics is needed to predict potential changes in the ocean carbon sink.

There are great uncertainties in quantifying the future ocean carbon sink and it prevents us from accurately calculating the allowable amount of additional emissions to limit global averaged temperature increases to less than 2^{o}C or 1.5^{o}C above preindustrial levels. These uncertainties stem primarily from our incomplete understanding of the mechanisms affecting the ocean carbon cycle and the representation of ocean physical and biological processes. Therefore, it's crucial that we investigate the causes behind the variations in the ocean carbon sink predictions provided by CMIP6 models. This could help us refine our current estimates and improve our future predictions of the ocean carbon sink.

Additionally, we need to evaluate the impact of a slowing overturning circulation on marine carbon dioxide removal (mCDR) strategies, aimed at sequestering carbon in the deep ocean. The slowdown of overturning circulation could potentially increase the carbon sequestration timescales, impacting the durability of these strategies. Many studies determining the durability of mCDR strategies assume that ocean circulation remains constant over time, neglecting the changes in overturning circulation in the context of climate warming (Siegel et al., 2021). It is therefore essential to quantify the effects of a slowing overturning circulation on the durability of ocean CDR strategies. Investigating these could provide pivotal insights into the potential consequences of climate change on carbon sequestration strategies, informing possible adaptations to these strategies in response to changing ocean circulation.

References

Bardin, Ann, et al. "Evaluation of the accuracy of an offline seasonally-varying matrix transport model for simulating ideal age." Ocean Modelling 105 (2016): 25-33.

Bardin, Ann, François Primeau, and Keith Lindsay. "An offline implicit solver for simulating prebomb radiocarbon." Ocean Modelling 73 (2014): 45-58.

Battaglia, Gianna, and Fortunat Joos. "Hazards of decreasing marine oxygen: the near-term and millennial-scale benefits of meeting the Paris climate targets." Earth system dynamics 9.2 (2018): 797-816.

Beadling, Rebecca L., et al. "Representation of Southern Ocean properties across coupled model intercomparison project generations: CMIP3 to CMIP6." Journal of Climate 33.15 (2020): 6555-6581.

Bernardello, Raffaele, et al. "Impact of Weddell Sea deep convection on natural and anthropogenic carbon in a climate model." Geophysical Research Letters 41.20 (2014): 7262-7269.

Bernardello, Raffaele, et al. "Response of the ocean natural carbon storage to projected twenty-first-century climate change." Journal of Climate 27.5 (2014): 2033-2053.

Bopp, Laurent, et al. "Multiple stressors of ocean ecosystems in the 21st century: projections with CMIP5 models." Biogeosciences 10.10 (2013): 6225-6245.

Bracegirdle, Thomas J., et al. "Assessment of surface winds over the Atlantic, Indian, and Pacific Ocean sectors of the Southern Ocean in CMIP5 models: Historical bias, forcing response, and state dependence." Journal of Geophysical Research: Atmospheres 118.2 (2013): 547-562.

Brennecka, Gregory A., et al. "Rapid expansion of oceanic anoxia immediately before the end-Permian mass extinction." Proceedings of the National Academy of Sciences 108.43 (2011): 17631-17634.

Bronselaer, Ben, and Laure Zanna. "Heat and carbon coupling reveals ocean warming due to circulation changes." Nature 584.7820 (2020): 227-233.

Caesar, Levke, et al. "Observed fingerprint of a weakening Atlantic Ocean overturning circulation." Nature 556.7700 (2018): 191-196.

Capotondi, Antonietta, et al. "Enhanced upper ocean stratification with climate change in the CMIP3 models." Journal of Geophysical Research: Oceans 117.C4 (2012).

Cessi, P., The Global Overturning Circulation. Annual Review of Marine Science, 11, 249–270 (2019).

Chamberlain, Matthew A., et al. "Transport matrices from standard ocean-model output and quantifying circulation response to climate change." Ocean Modelling 135 (2019): 1-13.

Chikamoto, Megumi O., and Pedro DiNezio. "Multi-Century Changes in the Ocean Carbon Cycle Controlled by the Tropical Oceans and the Southern Ocean." Global Biogeochemical Cycles 35.12 (2021): e2021GB007090.

Ciais, P., et al. "Attributing the increase in atmospheric CO2 to emitters and absorbers." Nature Climate Change 3.10 (2013): 926-930.

Clark, Peter U., et al. "Consequences of twenty-first-century policy for multi-millennial climate and sea-level change." Nature climate change 6.4 (2016): 360-369.

Danabasoglu, Gokhan, et al. "The CCSM4 ocean component." Journal of Climate 25.5 (2012): 1361-1389.

De Lavergne, Casimir, et al. “The impact of a variable mixing efficiency on the abyssal overturning.” Journal of Physical Oceanography 46.2 (2016): 663-681.

Deleersnijder, Eric, Jean-Michel Campin, and Eric JM Delhez. "The concept of age in marine modelling: I. Theory and preliminary model results." Journal of Marine Systems 28.3-4 (2001): 229-267.

Delhez, Eric JM, et al. "Toward a general theory of the age in ocean modelling." Ocean Modelling 1.1 (1999): 17-27.

DeVries, Tim. "The ocean carbon cycle." Annual Review of Environment and Resources 47 (2022): 317-341.

DeVries, Tim, and François Primeau. "Dynamically and observationally constrained estimates of water-mass distributions and ages in the global ocean." Journal of Physical Oceanography 41.12 (2011): 2381-2401.

DeVries, Tim, et al. "Decadal trends in the ocean carbon sink." Proceedings of the National Academy of Sciences 116.24 (2019): 11646-11651.

DeVries, Tim, Francois Primeau, and Curtis Deutsch. "The sequestration efficiency of the biological pump." Geophysical Research Letters 39.13 (2012).

DeVries, Tim, Mark Holzer, and Francois Primeau. "Recent increase in oceanic carbon uptake driven by weaker upper-ocean overturning." Nature 542.7640 (2017): 215-218.

Fay, Amanda R., and Galen A. McKinley. "Observed regional fluxes to constrain modeled estimates of the ocean carbon sink." Geophysical Research Letters 48.20 (2021): e2021GL095325.

Frajka-Williams, Eleanor, et al. "Atlantic meridional overturning circulation: Observed transport and variability." Frontiers in Marine Science (2019): 260.

Friedlingstein, Pierre, et al. "Global carbon budget 2021." Earth System Science Data 14.4 (2022): 1917-2005.

Friedlingstein, Pierre, et al. "Climate–carbon cycle feedback analysis: results from the C4MIP model intercomparison." Journal of climate 19.14 (2006): 3337-3353.

Friedlingstein, Pierre, et al. "Global carbon budget 2019." Earth System Science Data 11.4 (2019): 1783-1838.

Frölicher, Thomas L., and David J. Paynter. "Extending the relationship between global warming and cumulative carbon emissions to multi-millennial timescales." Environmental Research Letters 10.7 (2015): 075002.

Frölicher, Thomas L., and Fortunat Joos. "Reversible and irreversible impacts of greenhouse gas emissions in multi-century projections with the NCAR global coupled carbon cycle-climate model." Climate dynamics 35 (2010): 1439-1459.

Frölicher, Thomas L., et al. "Contrasting upper and deep ocean oxygen response to protracted global warming." Global biogeochemical cycles 34.8 (2020): e2020GB006601.

Fu, W., Randerson, J. T., Moore, J. K., Climate change impacts on net primary production (NPP) and export production (EP) regulated by increasing stratification and phytoplankton community structure in the CMIP5 models. Biogeosciences, 13, 5151–5170 (2016).

Fu, Weiwei, et al. "Evaluation of ocean biogeochemistry and carbon cycling in CMIP earth system models with the International Ocean Model Benchmarking (IOMB) software system." Journal of Geophysical Research: Oceans 127.10 (2022): e2022JC018965.

Fu, Weiwei, et al. "A growing freshwater lens in the Arctic Ocean with sustained climate warming disrupts marine ecosystem function." Journal of Geophysical Research: Biogeosciences 125.12 (2020): e2020JG005693.

Galbraith, E. D. & Martiny, A. C. A simple nutrient-dependence mechanism for predicting the stoichiometry of marine ecosystems. Proc Natl Acad Sci U S A 112, 8199-8204 (2015).

Garcia, H. et al. World ocean atlas 2018. Vol. 4: Dissolved inorganic nutrients (phosphate, nitrate and nitrate+ nitrite, silicate) (2019).

Gebbie, G., & Huybers, P. (2010). Total matrix intercomparison: A method for determining the geometry of water-mass pathways. Journal of Physical Oceanography, 40(8), 1710-1728.

Gent, Peter R., et al. "The community climate system model version 4." Journal of climate 24.19 (2011): 4973-4991.

Gloege, Lucas, et al. "Quantifying errors in observationally based estimates of ocean carbon sink variability." Global Biogeochemical Cycles 35.4 (2021): e2020GB006788.

Gnanadesikan, A., J. L. Russell, and Fanrong Zeng. "How does ocean ventilation change under global warming?." Ocean Science 3.1 (2007): 43-53.

Gruber, Nicolas, et al. "The oceanic sink for anthropogenic CO2 from 1994 to 2007." Science 363.6432 (2019): 1193-1199.

Hajima, Tomohiro, et al. "Millennium time-scale experiments on climate-carbon cycle with doubled CO2 concentration." Progress in Earth and Planetary Science 7.1 (2020): 1-19.

Henson, S. A., Sanders, R., Madsen, E., Morris, P. J., Le Moigne, F., & Quartly, G. D. (2011). A reduced estimate of the strength of the ocean's biological carbon pump. Geophysical Research Letters, 38(4).

Henson, Stephanie A., et al. "Uncertain response of ocean biological carbon export in a changing world." Nature Geoscience 15.4 (2022): 248-254.

Heuzé, Céline. "Antarctic bottom water and North Atlantic deep water in cmip6 models." Ocean Science 17.1 (2021): 59-90.

Holzer, Mark, and Tim DeVries. "Source-Labeled Anthropogenic Carbon Reveals a Large Shift of Preindustrial Carbon from the Ocean to the Atmosphere." Global Biogeochemical Cycles 36.10 (2022): e2022GB007405.

Holzer, Mark, and Timothy M. Hall. "Transit-time and tracer-age distributions in geophysical flows." Journal of the atmospheric sciences 57.21 (2000): 3539-3558.

Holzer, Mark, Matthew A. Chamberlain, and Richard J. Matear. "Climate-Driven Changes in the Ocean's Ventilation Pathways and Time Scales Diagnosed from Transport Matrices." Journal of Geophysical Research: Oceans 125.10 (2020): e2020JC016414.

Holzer, Mark, Tim DeVries, and Casimir de Lavergne. "Diffusion controls the ventilation of a Pacific Shadow Zone above abyssal overturning." Nature Communications 12.1 (2021): 1-13.

Hu, Aixue, et al. "Transient response of the MOC and climate to potential melting of the Greenland Ice Sheet in the 21st century." Geophysical Research Letters 36.10 (2009).

Ito, T., M. J. Follows, and E. A. Boyle. "Is AOU a good measure of respiration in the oceans?." Geophysical research letters 31.17 (2004).

Ito, Takamitsu, et al. "Sustained growth of the Southern Ocean carbon storage in a warming climate." Geophysical Research Letters 42.11 (2015): 4516-4522.

Jahn, Alexandra, and Marika M. Holland. "Implications of Arctic sea ice changes for North Atlantic deep convection and the meridional overturning circulation in CCSM4-CMIP5 simulations." Geophysical Research Letters 40.6 (2013): 1206-1211.

Jones, C. D., Ciais, P., Davis, S. J., Friedlingstein, P., Gasser, T., Peters, G. P., ... & Wiltshire, A. (2016). Simulating the Earth system response to negative emissions. Environmental Research Letters, 11(9), 095012.

Jones, C. D., & Friedlingstein, P. (2020). Quantifying process-level uncertainty contributions to TCRE and carbon budgets for meeting Paris Agreement climate targets. Environmental Research Letters, 15(7), 074019.

Katavouta, A., and Williams, R.G., Ocean carbon cycle feedbacks in CMIP6 models: contributions from different basins. Biogeosciences, 18, 3189-3218 (2021).

Katavouta, Anna, Richard G. Williams, and Philip Goodwin. "The effect of ocean ventilation on the transient climate response to emissions." Journal of Climate 32.16 (2019): 5085-5105.

Keller, D. P., Lenton, A., Littleton, E. W., Oschlies, A., Scott, V., & Vaughan, N. E. (2018). The effects of carbon dioxide removal on the carbon cycle. Current climate change reports, 4(3), 250-265.

Kessler, A., and J. Tjiputra. "The Southern Ocean as a constraint to reduce uncertainty in future ocean carbon sinks." Earth System Dynamics 7.2 (2016): 295-312.

Khatiwala, S., Martin Visbeck, and P. Schlosser. "Age tracers in an ocean GCM." Deep Sea Research Part I: Oceanographic Research Papers 48.6 (2001): 1423-1441.

Khatiwala, Samar, Martin Visbeck, and Mark A. Cane. "Accelerated simulation of passive tracers in ocean circulation models." Ocean Modelling 9.1 (2005): 51-69.

Koeve, Wolfgang, Paul Kähler, and Andreas Oschlies. "Does export production measure transient changes of the biological carbon pump's feedback to the atmosphere under global warming?." Geophysical Research Letters 47.22 (2020): e2020GL089928.

Kunze, Eric. “Internal-wave-driven mixing: Global geography and budgets.” Journal of Physical Oceanography 47.6 (2017): 1325-1345.

Kvale, Karin F., et al. "Evaluation of the transport matrix method for simulation of ocean biogeochemical tracers." Geoscientific Model Development 10.6 (2017): 2425-2445.

Kwiatkowski, Lester, et al. "Decline in Atlantic primary production accelerated by Greenland ice sheet melt." Geophysical Research Letters 46.20 (2019): 11347-11357.

Kwiatkowski, Lester, et al. "Twenty-first century ocean warming, acidification, deoxygenation, and upper-ocean nutrient and primary production decline from CMIP6 model projections." Biogeosciences 17.13 (2020): 3439-3470.

Kwon, Eun Young, et al. "Nutrient uptake plasticity in phytoplankton sustains future ocean net primary production." Science Advances 8.51 (2022): eadd2475.

Lago, Véronique, and Matthew H. England. "Projected slowdown of Antarctic bottom water formation in response to amplified meltwater contributions." Journal of Climate 32.19 (2019): 6319-6335.

Landschützer, Peter, et al. "Recent variability of the global ocean carbon sink." Global Biogeochemical Cycles 28.9 (2014): 927-949.

Landschützer, Peter, Nicolas Gruber, and Dorothee CE Bakker. "Decadal variations and trends of the global ocean carbon sink." Global Biogeochemical Cycles 30.10 (2016): 1396-1417.

Laufkötter, Charlotte, et al. "Projected decreases in future marine export production: the role of the carbon flux through the upper ocean ecosystem." Biogeosciences 13.13 (2016): 4023-4047.

Le Quéré, Corinne, et al. "Saturation of the Southern Ocean CO2 sink due to recent climate change." science 316.5832 (2007): 1735-1738.

Levin, Lisa A. "Manifestation, drivers, and emergence of open ocean deoxygenation." Annual review of marine science 10 (2018): 229-260.

Li, Guancheng, et al. "Increasing ocean stratification over the past half-century." Nature Climate Change 10.12 (2020): 1116-1123.

Li, Qian, et al. "Abyssal ocean overturning slowdown and warming driven by Antarctic meltwater." Nature 615.7954 (2023): 841-847.

Lindsay, Keith, et al. "Preindustrial-control and twentieth-century carbon cycle experiments with the Earth System Model CESM1 (BGC)." Journal of Climate 27.24 (2014): 8981-9005.

Liu, Wei, Alexey Fedorov, and Florian Sévellec. "The mechanisms of the Atlantic meridional overturning circulation slowdown induced by Arctic sea ice decline." Journal of Climate 32.4 (2019): 977-996.

Liu, Yi, et al. "Reduced CO2 uptake and growing nutrient sequestration from slowing overturning circulation." Nature Climate Change 13.1 (2023): 83-90.

Locarnini, M., et al. World ocean atlas 2018, volume 1: Temperature. (2018).

Long, Matthew C., et al. "Twentieth-century oceanic carbon uptake and storage in CESM1 (BGC)." Journal of Climate 26.18 (2013): 6775-6800.

Lovenduski, Nicole S., et al. "Enhanced CO2 outgassing in the Southern Ocean from a positive phase of the Southern Annular Mode." Global Biogeochemical Cycles 21.2 (2007).

Lovenduski, Nicole S., et al. "Multi-decadal trends in the advection and mixing of natural carbon in the Southern Ocean." Geophysical Research Letters 40.1 (2013): 139-142.

Lumpkin, Rick, and Kevin Speer. "Global ocean meridional overturning." Journal of Physical Oceanography 37.10 (2007): 2550-2562.

M.B. Osman, et al., Industrial-era decline in subarctic Atlantic productivity. Nature, 569, 551–555 (2019).

Mackie, Shona, et al. "Climate response to increasing Antarctic iceberg and ice shelf melt." Journal of Climate 33.20 (2020): 8917-8938.

Matear, Richard J., and Anthony C. Hirst. "Climate change feedback on the future oceanic CO2 uptake." Tellus B 51.3 (1999): 722-733.

Matsumoto, Katsumi, et al. "Characterizing post-industrial changes in the ocean carbon cycle in an Earth system model." Tellus B: Chemical and Physical Meteorology 62.4 (2010): 296-313.

McCarthy, Gerard D., et al. “Measuring the Atlantic meridional overturning circulation at 26 N.” Progress in Oceanography 130 (2015): 91-111.

McKinley, Galen A., et al. "Natural variability and anthropogenic trends in the ocean carbon sink." Annual review of marine science 9.1 (2017): 125-150.

McKinley, Galen A., et al. "Modern air-sea flux distributions reduce uncertainty in the future ocean carbon sink." Environmental Research Letters 18.4 (2023): 044011.

McNeil, B. I., and R. J. Matear. "The non-steady state oceanic CO 2 signal: its importance, magnitude and a novel way to detect it." Biogeosciences 10.4 (2013): 2219-2228.

Meinen, Christopher S., et al. "Meridional overturning circulation transport variability at 34.5 S during 2009–2017: Baroclinic and barotropic flows and the dueling influence of the boundaries." Geophysical Research Letters 45.9 (2018): 4180-4188.

Meinshausen, Malte, et al. "The RCP greenhouse gas concentrations and their extensions from 1765 to 2300." Climatic change 109.1 (2011): 213-241.

Misumi, K., et al. "The iron budget in ocean surface waters in the 20th and 21st centuries: projections by the Community Earth System Model version 1." Biogeosciences 11.1 (2014): 33-55.

Moore, J. Keith, et al. "Marine ecosystem dynamics and biogeochemical cycling in the Community Earth System Model [CESM1 (BGC)]: Comparison of the 1990s with the 2090s under the RCP4. 5 and RCP8. 5 scenarios." Journal of Climate 26.23 (2013): 9291-9312.

Moore, J. Keith, et al. "Sustained climate warming drives declining marine biological productivity." Science 359.6380 (2018): 1139-1143

Moore, J. Keith, Scott C. Doney, and Keith Lindsay. "Upper ocean ecosystem dynamics and iron cycling in a global three-dimensional model." Global Biogeochemical Cycles 18.4 (2004).

N. Gruber, et al., The oceanic sink for anthropogenic CO2 from 1994 to 2007. Science, 363, 1193-1199 (2019).

Nowicki, Michael, Tim DeVries, and David A. Siegel. "Quantifying the carbon export and sequestration pathways of the ocean's biological carbon pump." Global Biogeochemical Cycles 36.3 (2022): e2021GB007083.

O'Neill, Brian C., et al. "The scenario model intercomparison project (ScenarioMIP) for CMIP6." Geoscientific Model Development 9.9 (2016): 3461-3482.

Ödalen, Malin, et al. "The influence of the ocean circulation state on ocean carbon storage and CO 2 drawdown potential in an Earth system model." Biogeosciences 15.5 (2018): 1367-1393.

Palevsky, H. I., & Doney, S. C. (2018). How choice of depth horizon influences the estimated spatial patterns and global magnitude of ocean carbon export flux. Geophysical Research Letters, 45(9), 4171-4179.

Palter, J. B., et al. "Fueling export production: nutrient return pathways from the deep ocean and their dependence on the Meridional Overturning Circulation." Biogeosciences 7.11 (2010): 3549-3568.

Plattner, G-K., et al. "Feedback mechanisms and sensitivities of ocean carbon uptake under global warming." Tellus B: Chemical and Physical Meteorology 53.5 (2001): 564-592.

Plattner, G-K., et al. "Long-term climate commitments projected with climate–carbon cycle models." Journal of Climate 21.12 (2008): 2721-2751.

Prend, Channing J., et al. "Indo-Pacific sector dominates Southern Ocean carbon outgassing." Global Biogeochemical Cycles 36.7 (2022): e2021GB007226.

Primeau, François W., and Mark Holzer. "The ocean's memory of the atmosphere: Residence-time and ventilation-rate distributions of water masses." Journal of physical oceanography 36.7 (2006): 1439-1456.

Primeau, François. "Characterizing transport between the surface mixed layer and the ocean interior with a forward and adjoint global ocean transport model." Journal of Physical Oceanography 35.4 (2005): 545-564.

Randerson, James T., et al. "Multicentury changes in ocean and land contributions to the climate-carbon feedback." Global Biogeochemical Cycles 29.6 (2015): 744-759.

Ridge, Sean M., and Galen A. McKinley. "Ocean carbon uptake under aggressive emission mitigation." Biogeosciences 18.8 (2021): 2711-2725.

Rousselet, Louise, Paola Cessi, and Gael Forget. "Coupling of the mid-depth and abyssal components of the global overturning circulation according to a state estimate." Science Advances 7.21 (2021): eabf5478.

Russell, Joellen L., et al. "The Southern Hemisphere westerlies in a warming world: Propping open the door to the deep ocean." Journal of Climate 19.24 (2006): 6382-6390.

Sabine, Christopher L., et al. "The oceanic sink for anthropogenic CO2." science 305.5682 (2004): 367-371.

Schmittner, Andreas, et al. "Future changes in climate, ocean circulation, ecosystems, and biogeochemical cycling simulated for a business-as-usual CO2 emission scenario until year 4000 AD." Global biogeochemical cycles 22.1 (2008).

Schmittner, Andreas. "Decline of the marine ecosystem caused by a reduction in the Atlantic overturning circulation." Nature 434.7033 (2005): 628-633.

Schurer, Andrew P., et al. "Interpretations of the Paris climate target." Nature Geoscience 11.4 (2018): 220-221.

Shah, Syed Hyder Ali Muttaqi, et al. "Tracing the ventilation pathways of the deep North Pacific Ocean using Lagrangian particles and Eulerian tracers." Journal of Physical Oceanography 47.6 (2017): 1261-1280.

Sherman, Elliot, et al. "Temperature influence on phytoplankton community growth rates." Global Biogeochemical Cycles 30.4 (2016): 550-559.

Siegel, David A., et al. "Assessing the sequestration time scales of some ocean-based carbon dioxide reduction strategies." Environmental Research Letters (2021).

Smith, R., et al. "The parallel ocean program (POP) reference manual: ocean component of the community climate system model (CCSM) and community earth system model (CESM)." LAUR-01853 141 (2010): 1-140.

Steffen, Will, et al. "Trajectories of the Earth System in the Anthropocene." Proceedings of the National Academy of Sciences 115.33 (2018): 8252-8259.

Swingedouw, Didier, et al. "On the risk of abrupt changes in the North Atlantic subpolar gyre in CMIP6 models." Annals of the New York Academy of Sciences 1504.1 (2021): 187-201.

Talley, Lynne D. "Closure of the global overturning circulation through the Indian, Pacific, and Southern Oceans: Schematics and transports." Oceanography 26.1 (2013): 80-97.

Terhaar, J., Frölicher, T. L., & Joos, F. (2022). Observation-constrained estimates of the global ocean carbon sink from Earth system models. Biogeosciences, 19(18), 4431-4457.

Terada, Mio, Shoshiro Minobe, and Curtis Deutsch. "Mechanisms of future changes in equatorial upwelling: CMIP5 intermodel analysis." Journal of Climate 33.2 (2020): 497-510.

Thornalley, David JR, et al. "Anomalously weak Labrador Sea convection and Atlantic overturning during the past 150 years." Nature 556.7700 (2018): 227-230.

Volk, Tyler, and Martin I. Hoffert. "Ocean carbon pumps: Analysis of relative strengths and efficiencies in ocean-driven atmospheric CO2 changes." The carbon cycle and atmospheric CO2: Natural variations Archean to present 32 (1985): 99-110.

W. Weijer, W. Cheng, O.A. Garuba, A. Hu, B.T. Nadiga, CMIP6 Models Predict Significant 21st Century Decline of the Atlantic Meridional Overturning Circulation. Geophys. Res. Lett., 47, e2019GL086075 (2020).

Waugh, Darryn W. "Changes in the ventilation of the southern oceans." Philosophical Transactions of the Royal Society A: Mathematical, Physical and Engineering Sciences 372.2019 (2014): 20130269.

Waugh, Darryn W., et al. "Recent changes in the ventilation of the southern oceans." science 339.6119 (2013): 568-570.

Weijer, Wilbert, et al. "CMIP6 models predict significant 21st century decline of the Atlantic Meridional Overturning Circulation." Geophysical Research Letters 47.12 (2020): e2019GL086075.

Whitt, D. B. & Jansen, M. F., Slower nutrient stream suppresses Subarctic Atlantic Ocean biological productivity in global warming. PNAS, 117, 15504–15510 (2020).

Wiseman, N. A., et al. "Acclimation of phytoplankton Fe: C ratios dampens the biogeochemical response to varying atmospheric deposition of soluble iron." Global Biogeochemical Cycles (2023): e2022GB007491.

Yamamoto, A., et al. "Global deep ocean oxygenation by enhanced ventilation in the Southern Ocean under long-term global warming." Global Biogeochemical Cycles 29.10 (2015): 1801-1815.

Yamamoto, Akitomo, Ayako Abe-Ouchi, and Yasuhiro Yamanaka. "Long-term response of oceanic carbon uptake to global warming via physical and biological pumps." Biogeosciences 15.13 (2018): 4163-4180.

Yeager, Stephen, and Gokhan Danabasoglu. "The origins of late-twentieth-century variations in the large-scale North Atlantic circulation." Journal of Climate 27.9 (2014): 3222-3247.

Zickfeld, Kirsten, et al. "Long-term climate change commitment and reversibility: an EMIC intercomparison." Journal of Climate 26.16 (2013): 5782-5809.

Zickfeld, Kirsten, Michael Eby, and Andrew J. Weaver. "Carbon-cycle feedbacks of changes in the Atlantic meridional overturning circulation under future atmospheric CO2." Global Biogeochemical Cycles 22.3 (2008).